UiO : **Department of Mathematics**
University of Oslo

In depth PIV analysis of turbulent single phase pipe flow

Special attention on particles; size and emission properties

Sebastian Gyllengahm
Master's Thesis, Autumn 2019

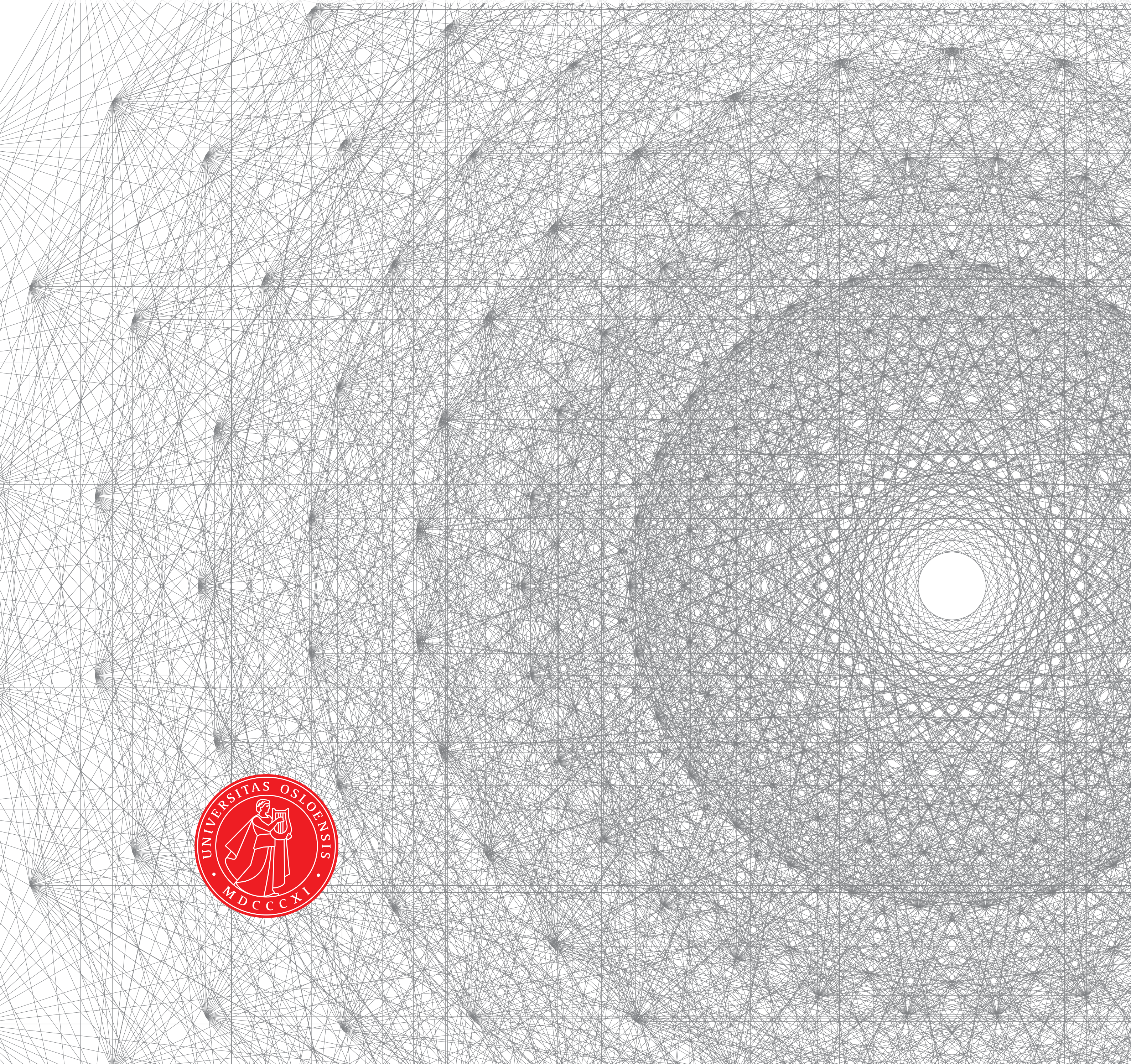

This master's thesis is submitted under the master's programme *Computational Science and Engineering*, with programme option *Mechanics*, at the Department of Mathematics, University of Oslo. The scope of the thesis is 60 credits.

The front page depicts a section of the root system of the exceptional Lie group E_8, projected into the plane. Lie groups were invented by the Norwegian mathematician Sophus Lie (1842–1899) to express symmetries in differential equations and today they play a central role in various parts of mathematics.

Acknowledgements

I would like to thank my supervisor Professor Atle Jensen for his guidance, support and for providing me with an interesting topic. Thank you to my supervisor Dr.Anis Awal Ayati for giving me the opportunity to travel to Rio de Janeiro, for providing me with an interesting topic, for the guidance and also for inviting me to the workshops in Oslo and Rio de Janeiro. Thank you to my supervisor Petter Vollestad for all the help in the lab, the guidance and much needed help in the experimental set-up. Thank you also to Olav Gundersen for all the help in the lab. I also would like to say thank you to Professor Igor de Paula and Paula Bormann at PUC-Rio for helping me in the lab and for being so hospitable during my stay at PUC-Rio. All of you have played a significant part in the completion of this thesis.

Contents

List of Figures

List of Tables

Chapter 1

Introduction

1.1 Preface

This thesis were supposed to cover a different topic than what it currently does. The original work plan were to investigate the stability of stratified gas-liquid flow by means of using experimental two phase fluid mean axial profiles in an Orr-Sommerfeld solver and then compare these results with theory. An experimental campaign was launched at PUC-Rio, Brazil in order to gather the experimental data and the whole fall semester were spent in Rio de Janeiro at PUC. Several profiles were gained with base flow and with waves. The data together with results and other relevant material were stored in a portable hard drive that unfortunately were stolen in the middle of the spring semester in Oslo and no back up were available. The former work plan thus had to be abandoned and another work plan was set where new experimental data had to be produced to finish up the thesis. The stay in Brazil did however give me plenty of experimental experience, some theoretical knowledge about parallel flow instabilities and a greatly improved my Matlab skills. A remaining result from one of the experimental profiles that were put in the Orr-Sommerfeld solver and compared with a kaffel table which shows the can be seen in the Appendix 6.3

1.2 Motivation and related research

Fluid dynamics is a discipline concerned about fluids in motion. The fundamental equations of fluid motion were derived for over 100 years ago and have to this day no known solution, making the discipline of fluid dynamics dependent on numerical simulations and experiments in order to conduct relevant research. Hence, both direct numerical simulations(DNS) and experiments are of fundamental importance within the field and will create synergy effects and serve as validation when used wisely in combination to investigate practical problems in fluid dynamics.

Particle image velocimetry(PIV) is one of the most important measuring techniques in fluid dynamics and is used in both fundamental and industrial research. New areas of application outside fluid mechanics are continuously reported such as in biology and turbulent machinery[38]. As DNS becomes more feasible as the computer power increases, PIV experiments will almost certainly continue to be an essential tool in the future for understanding the behaviour of fluids. One of the main issues in PIV is to seed the flow field with suitable particles. It is important that the particles does not change the fluid dynamics by their presence and at the same time, they should match the fluid density in order to avoid gravitational effects[38]. This thesis will focus on two different seeding particles with respect to their ability to reflect turbulent structures in single phase pipe flow trough the method of PIV in water. One commercial polyamide particle and a fluorescent particle extracted from a commercial acrylic paint have been compared in terms of mean- and turbulent-profiles as well as power density spectras. The experiments have been conducted in a 31 meter long PVC pipe with an internal diameter of $D = 10cm$ and three ranges of different Reynolds numbers(15-17k, 23-25k and 35k) have been investigated in pairs. Wu and Moin (2008)[7] simulated a fully developed incompressible turbulent pipe flow at bulk velocity based Reynolds number $Re_{U_b} = 44k$. The results from Wu and Moin together with a single gas phase flow seeded with water particles have served as a validation of the experimental set-up and the mean- and turbulent-profiles in this thesis. Previous successful attempts in using the same fluorescent particle as in this study have been conducted by Nogueira et al. (2003)[3] and by Birvalski (2015)[2]. Nogueira et al.(2003) performed PIV experiments in a pipe to study slug flows and seeded the water phase with fluorescent particles. They successfully presented a new technique to simultaneously determine both shape and the surrounding flow around a Taylor bubble. A thin liquid film around the Taylor bubble were resolved and this region, as it is close to the pipe wall, will in general be very polluted with reflections. These reflections were mitigated due to the fact that fluorescent particles have another wave length than the laser light and gives the opportunity to filter out the laser light and thus reflections but still allow the passage of the light emitted from the fluorescent particles. Birvalski(2015) conducted PIV experiments to achieve stratified multi-phase flow in a horizontal and slightly titled pipe where he among other things successfully exploited the emitting properties of the fluorescent particles to reduce the contamination of the PIV frames. Polyamide particles do have a refractive index and thus reflects the light from the light source whereas the fluorescent particles emits light; hence the two particles come with different properties and they can therefore be useful in different kinds of experimental applications and endeavours within PIV. This thesis attempts to show that both particles despite these different properties equally well will follow and accurate reflect the mean flow and turbulent fluctuations in the performed single phase flow experiments.

1.3 Outline

Chapter 2 describes the mathematical and physical background theory that are relevant in this study as well as an detailed discussion of PIV were a large part is devoted to errors in PIV. Chapter 3 presents and describes the experimental set-up. The second section in chapter 3 discusses challenges related to the experimental campaign that are of importance regarding the results and accuracy of this study. Cases that have been performed are presented in detail as well as the post processing techniques of the experimental data. Chapter 4 and 5 is devoted to discussion and presentation of the validation, results and conclusion of the this study. Validation and results are presented in terms of mean- and turbulence -profiles compared with the DNS results from Wu and Moin as well as power density spectras compared with the Kolmogorov spectra. A section in the Appendix present some remains from the study in Brazil.

Chapter 2

Background theory

2.1 Background theory

In this work an experimental investigation of the behavior of a fluid in motion have been conducted. The motion of an incompressible and Newtonian fluid is governed by the Navier-Stokes equations which are a set of nonlinear partial differential equations defined as in 2.1 and 2.2. These are an expression of Newtons Second Law for fluids, stating that mass times the acceleration of fluid particles is proportional to the forces acting on them. They read as follows

$$\nabla \cdot \boldsymbol{u} = 0 \tag{2.1}$$

$$\frac{\partial \boldsymbol{u}}{\partial t} + (\boldsymbol{u} \cdot \nabla)\boldsymbol{u} = -\frac{1}{\rho}\nabla P + \boldsymbol{f} + \mu \nabla^2 \boldsymbol{u} \tag{2.2}$$

and we have that $\boldsymbol{u} = \boldsymbol{u}(\boldsymbol{x}, t)$ is the velocity vector and the solution of 2.1 and 2.2, ρ is the fluid density, $P = P(\boldsymbol{x}, t)$ is the pressure, $\boldsymbol{f}$ are body forces, μ is the viscosity, $x = (x, y, z, t)$ is the position vector and t is the time. The solution $\boldsymbol{u} = \boldsymbol{u}(\boldsymbol{x}, t)$ describes the velocity field whereas $P = P(\boldsymbol{x}, t)$ describes the scalar pressure field. These equations are infamously known to be very hard to study and analyze in general. Thus it is common to turn to other methods in order to investigate fluid flow which are governed by these set of equations, such as experiments as in this work or numerical simulations[22].

One way of analytically analyze fluid flow is to use dimensionless numbers. These are physical parameters that doesn't have no units of measurement. They remain the same whether metric or other units are used in the equation and can be used to compare flows with different scale. One particularly useful dimensionless quantity is the Reynolds number 2.3.

$$Re = \frac{\rho U L}{\mu} \tag{2.3}$$

where U is the velocity scale, L is a characteristic geometric size, and ρ and μ are the fluid density and viscosity respectively. The Reynolds number give us an estimate of the relation between the inertia and viscosity in a fluid flow. Flow with different Reynolds number will in general have very different characteristics and flow with similar Reynolds number will in general have similarities in regards to turbulent intensity etc. Flows with a low (below 2000) Reynolds number tend to be laminar whereas flows with a high Reynolds number (over 2000) tend to be turbulent. These numbers however are not exact and depends on various parameters.

2.1.1 Turbulence

Turbulence is a flow phenomenon that is very commonplace in the nature around us. It is a flow regime distinct from laminar flow as it is seemingly totally random and are characterized by chaotic three dimensional vorticity. The road between laminar and fully turbulent flow is very complex and goes through many stages of sometimes intermittent flow regimes before the fully developed turbulent flow is established [19]. When turbulence is present it usually dominates all other flow phenomena and results in increased energy dissipation, mixing, heat transfer, and drag. An example of when increased mixing is very well used is for example when we mix milk with tea in a cup, without a stir of the liquid with the spoon, the milk will take a long time to mix in to the liquid; whereas it can be seen to mix very rapidly after a little stir that create turbulence. Other examples of turbulence occurring in our every day life are many. Smoke from a cigarette, the flow out of a water tap, the wake after a walking person or a moving locomotive. Turbulence are wanted in some circumstances and in some others not. It is however not yet fully understood and more research needs to be done[20].

Physical description of turbulence

Even though turbulence seem to be completely random it has a clear spatial structure and can be described by the following characteristics (Frank M White 2006)[22]:

Fluctuations in pressure, velocity and temperature. Fluctuations are superimposed upon the mean value of each property.

Eddies of different size that mix and fill the shear layer. Eddy size varies from a shear layer thickness δ (this thickness depends on the situation) down to the so-called Kolmogorov lenght scale $\eta = (\nu^3\delta/U^3)^{\frac{1}{4}}$, where ν is the kinematic viscosity and U is the velocity.

Random and specific variation in fluid properties. Each property has a specific continuous energy spectrum. This spectrum drops off to zero as a function of the eddy size.

Self sustaining motion. Turbulent flow can maintain itself by producing new eddies to replace those lost by viscous dissipation.

Mixing in turbulence,as mentioned before, is much stronger than that due to pure laminar (molecular) action. The nature of the three dimensional turbulent eddy motion will cause rapid diffusion of mass, momentum and energy.

A mathematical description of turbulence, mean flow and fluctuations

Since actual computation of the velocity component $\boldsymbol{u}(\boldsymbol{x}, t)$ is not possible in turbulent flow the standard analysis of turbulence separates the fluctuating property from it's time-mean value.

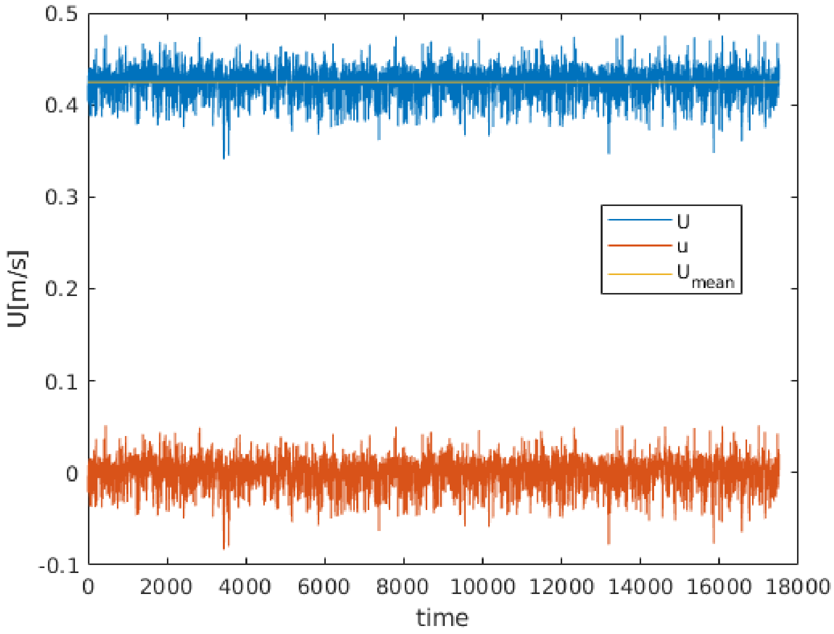

Figure 2.1: *An illustration of the mean and fluctuation velocities produced from the collected data in this thesis. U is the true velocity, u is the velocity fluctuation and* U_{mean} *is the mean velocity.*

By Lautrup (2011) [20] the mainstream field is defined by

$$\overline{\boldsymbol{u}(\boldsymbol{x}, t)} = \lim_{T \to \infty} \frac{1}{T} \int_0^T \boldsymbol{u}(\boldsymbol{x}, t + s) ds \tag{2.4}$$

where T is the time interval starting at any time t. This average is assumed to exist and to be time independent in the limit. This definition can be exploited in order to evaluate the mean value experimentally. This can be done to any desired precision from the average of a sufficiently large number fo measurements of the instantaneous velocity field near the point $\boldsymbol{x}$ over a long enough time period T. Now, the fluctuating part is defined as the difference between the instant/true velocity field and it's mean value. We have

$$\boldsymbol{u'}(\boldsymbol{x}, t) = \boldsymbol{u}(\boldsymbol{x}, t) - \overline{\boldsymbol{u}(\boldsymbol{x}, t)} \tag{2.5}$$

This fluctuation part 2.6 have a vanishing average, i.e.

$$\lim_{T \to \infty} \frac{1}{T} \int_0^T \boldsymbol{u'}(\boldsymbol{x}, t+s) ds = \lim_{T \to \infty} \frac{1}{T} \int_0^T (\boldsymbol{u}(\boldsymbol{x}, t+s) - \overline{\boldsymbol{u}(\boldsymbol{x}, t+s)}) ds = 0. \tag{2.6}$$

where we have used that,

$$\lim_{T\to\infty}\frac{1}{T}\int_0^T \overline{\boldsymbol{u}(\boldsymbol{x},t+s)}ds = \overline{\boldsymbol{u}(\boldsymbol{x},t)} \tag{2.7}$$

which comes from the assumption that the average is time independent in the limit.
All the present fields in a turbulent flow can be averaged in a similar way as $\boldsymbol{u}$. The system is said to be in statistically equilibrium when all mean values are time independent.

Reynolds stress

From the above observations we may now establish the so-called Reynold's decomposition by (Osborne Reynolds, 1895)[25] as defined in equation 2.8.

$$\boldsymbol{u}(\boldsymbol{x},t) = \overline{\boldsymbol{u}(\boldsymbol{x},t)} + \boldsymbol{u'}(\boldsymbol{x},t). \tag{2.8}$$

The idea on wards is now to put 2.8 into the Navier-Stokes equations 2.1 and 2.2 to obtain the Reynolds stress tensor. Now, let us start out by put 2.8 into 2.1. We have that

$$\nabla\cdot\boldsymbol{u}(\boldsymbol{x},t) = \nabla\cdot(\overline{\boldsymbol{u}(\boldsymbol{x},t)} + \boldsymbol{u'}(\boldsymbol{x}),t) = 0. \tag{2.9}$$

By taking the time average we get

$$\overline{\nabla\cdot\boldsymbol{u}(\boldsymbol{x},t)} = \nabla\cdot(\overline{\boldsymbol{u}(\boldsymbol{x},t)} + \boldsymbol{u'},\boldsymbol{x},t) = \nabla\cdot\overline{\boldsymbol{u}(\boldsymbol{x},t)} = 0, \tag{2.10}$$

which directly implies that,

$$\nabla\cdot\boldsymbol{u'} = 0. \tag{2.11}$$

Next we want to take the mean of the momentum equation 2.2. We start by looking at the particle derivative that contains a non-linearity, i.e the convective term seen as the last part in 2.12. Notice that we also introduce tensor notation where $u_i = (u(x,y,z,t), v(x,y,z,t), w(x,y,z,t))$, $i = 1,2,3$ and $j = 1,2,3$.

$$\frac{Du_i}{Dt} = \frac{\partial u_j}{\partial t} + \frac{\partial}{\partial x_i}(u_i u_j) \tag{2.12}$$

By taking the mean we obtain

$$\frac{D\overline{u_i}}{Dt} = \frac{\partial\overline{u_j}}{\partial t} + \frac{\partial}{\partial x_i}(\overline{u_i u_j}). \tag{2.13}$$

We can simplify 2.13 by first look at the convective term and substitute with 2.8,by using 2.6, we get

$$\overline{u_i u_j} = \overline{(\overline{u_i} + u'_i)(\overline{u_j} + u'_j)} = \tag{2.14}$$

$$\overline{\overline{u_i u_j} + \overline{u_i}u'_j + u'_i\overline{u_j} + u'_i u'_j} = \tag{2.15}$$

$$\overline{\overline{u_i u_j} + u_i u'_j} = \overline{u_i u_j} + \overline{u'_i u'_j}. \tag{2.16}$$

Combining this result with the previous equation we obtain

$$\overline{\frac{Du_j}{Dt}} = \frac{\partial \overline{u_j}}{\partial t} + \frac{\partial}{\partial x_i}(\overline{u_i u_j} + \overline{u'_i u'_j}) = \tag{2.17}$$

$$\frac{\partial \overline{u_j}}{\partial t} + \frac{\partial}{\partial x_i}(\overline{u_i u_j}) + \frac{\partial}{\partial x_i}(\overline{u'_i u'_j}) = \tag{2.18}$$

$$\frac{\partial \overline{u_j}}{\partial t} + \overline{u_i}\frac{\partial}{\partial x_i}\overline{u_j} + \frac{\partial}{\partial x_i}(\overline{u'_i u'_j}). \tag{2.19}$$

Then we can take the mean of the rest of the momentum equation. But first we want to define the mean particle derivative,

$$\frac{\bar{D}}{Dt} = \frac{\partial}{\partial t} + \overline{u_j} \cdot \nabla \tag{2.20}$$

to finally arrive at

$$\frac{\bar{D}\overline{u_j}}{\bar{D}t} = -\frac{1}{\rho}\frac{\partial \overline{P}}{\partial x_j} + \nu \nabla^2 \overline{u_j} - \frac{\partial \overline{u'_i u'_j}}{\partial x_i}. \tag{2.21}$$

We notice that the only thing that differ 2.21 from 2.2 is the last term on r.h.s in 2.21, which is called the Reynolds stress tensor, i.e. $\overline{u'_i u'_j}$. This term is never negligible in a turbulent flow. If this term is zero, which is indicating a laminar flow regime, 2.21 will be reduced to 2.2.

The Reynolds stress tensor is symmetric and in particular we have $u'v'$ which is a turbulent shear stress, $u'u'$ and $v'v'$ which is the turbulent kinetic energy.

Kolmogorov spectrum

Richardson's energy cascade theory(see, Richardson,1920)[10] argues that the largest eddies within a flow are unstable and break down and by doing so creates smaller eddies which in their turn break up and creates even smaller eddies, and so on, until viscosity. This "cascade" transfers the kinetic energy of the flow from the largest eddie scales down to the smallest. The turbulent energy cascade can be characterized by the energy spectrum $E(\kappa)$ which describe the distribution of the energy as a function of the wave number κ.

$$\frac{1}{2}\overline{(u'_i u'_i)} = \int_0^\infty E(\kappa) d\kappa \tag{2.22}$$

The wave number κ is $\kappa \sim 1/L$ related to the characteristic eddie size L and $\overline{(u'_i u'_i)}$ is the averaged turbulent kinetic energy. As mentioned before, the eddie sizes will vary between the largest eddies of size L_0, defined by the boundaries of the flow, down to the smallest eddie, defined by the Kolmogorov length η. In between those two wave numbers where $1/L_0 << \kappa << 1/\eta$ is a region called the integral length scale. This is a region where inertial effects are still dominating over viscous and according to a hypothesis of Kolmogorov, the energy spectrum $E(\kappa)$ solely depend on the wavenumber κ and the viscous dissipation ϵ within this region. Consider the dimensional analysis:

$$[\frac{1}{2}\overline{(u'_i u'_i)}] \sim m^2 s^{-2}; \quad [\epsilon] \sim m^2 s^{-3}; \quad [\kappa] \sim m^-; \tag{2.23}$$

where

$$[E(\kappa)] \sim \frac{[\frac{1}{2}\overline{(u_i'u_i')}]}{\kappa} \sim m^3 s^{-2}. \tag{2.24}$$

Given the hypothesis from Kolmogorov there is only one possible form for the energy spectrum, namely

$$E(\kappa) \sim \epsilon^{\frac{2}{3}} \kappa^{\frac{-5}{3}}, \tag{2.25}$$

and

$$E(\kappa) = C\epsilon^{\frac{2}{3}} \kappa^{\frac{-5}{3}}. \tag{2.26}$$

Equation 2.26 is the famous Kolmogorov spectrum where C is an universal constant, experimentally determined to be 1.5. So, the $-5/3$s law states that in some inertial range $[\kappa_1, \kappa_2]$, the energy density of the flow $E(\kappa)$ behaves like $1.5\kappa^{-5/3}$. The Kolmogorov spectrum have been confirmed by numerical simulations (see, for example, Ishiara (2003)[8] and Chen and Xu (2013)[9]). it is important to note that the theory of Kolmogorov does come with some limitations. Some objections mentioned in the book by Pope, (2003)[21], are for example: That the theory is only valid for sufficiently high Reynolds numbers and there is no criterion for what a high enough Reynolds number would be. That the energy cascade only consist of a one way transfer of energy is considered to be an oversimplification, something that is very difficult to measure experimentally. According to the Kolmogorov hypothesis the skewness and kurtosis of the turbulence fluctuations are supposed to be universal constants, but are proven to vary as a function of the Reynolds number. Most importantly though, according to Pope, these issues mentioned can be assumed to have only a minor significance in the context of mean velocity fields and Reynolds stresses.

2.1.2 Tracer particles

The novelty of this study is to compare two different tracer particles in a PIV experiment to investigate their exactness of representing mean and turbulent motions in a fluid. These particles are: a commercially manufactured polyamide particle from Dantec Dynamics [1] and a fluorescent particle extracted from a commercially acrylic paint (Lefranc & Bourgeois, Fluorescent Light Orange colour), see appendix 6.1, previously used in PIV experiments by Birvalski (2005)[2] and Nogueira et al. (2003)[3]. Some technical information about the particle differences are presented in table 2.1. Worth to note is that the density of water is $\rho_{water} = 1[gr/cm^3]$, and hence, both particles are close to neutrally buoyant.

$Particle$	$\overline{d_p}[\mu m]$	$d_p[\mu m]$	$Shape$	$\rho[gr/cm^3]$	$Material$
$Polyamide$	50	$30-70$	$Round$	1.03	$Polyamid12$
$Flashe$	6	$2-10$	$Unknown$	1.02	$Acrylic$

Table 2.1: *A technical comparison of the particles where $\overline{d_p}$ is the mean diameter and d_p is the size distribution. The information about the Polyamid particle are drawn from the Dantec website [1] for the Flashe see 6.1.*

The light emitted by the fluorescent particles are around 590 nm according to Nogueira et al. (2003)[3] while the polyamid particle will reflect the light from the source which in this case is a Nd:YAG laser with a wave length of 532 nm. The shape of the Polyamide particles is round but not spherical and the shape of the Flashe particles is assumed to be round particles and not flakes.

2.2 Particle Image Velocimetry

As previously mentioned this study is based on a experimental investigation of fluid flow, and in specific of fluid pipe flow. There are several ways to investigate the motion of a fluid such as Particle tracking velocimetry, X-ray etc. but in this study however a technique that is called PIV have been employed throughout.

2.2.1 What is PIV[27][28]

Particle Image Velocimetry (PIV) is a measuring technique which allows for capturing the velocity information of whole flow fields in both gaseous and liquid media. Moreover, it is a non-intrusive optical method, which means that it does not interfere with the flow in any way, in contrast we have, for instance, probe techniques where the flow is disturbed by the presence of the probe itself. It is a indirect velocity measurement technique where tracers are added to the flow with the assumption that these tracers are following the motion of the fluid elements. The light scattered from the tracer particles are recorded by a camera on a sequence of frames. The displacement of the particles is then evaluated between subsequent image pairs and thus resolves the instant velocity field in both time and a space, given that you know the time difference between images.

Development of PIV started in the 1980's and are widely used in both industrial and fundamental research in fluid mechanics and others Raffel et al. (2018) [38].

2.2.2 Principle for PIV

PIV measurements in general can be conducted in various ways but are in general based on a three basic principles. These are, by (Koolas 2017)[28]

A visual representation of the fluid flow.

An imaging system for capturing the visual representation

A method of for processing the images for quantify the fluid motion.

In general the tracer particles need to be added and then illuminated in a 2D-plane. The tracer particles should be naturally buoyant and have a light scattering property good enough such that the movement of the particles can easily be captured by the camera. It is also important to carefully select particles that are faithfully following the actual flow without any velocity lag. In general smaller particles follow the flow better. Illumination should take place two times in a short enough, pulse like, time interval so that each particle "freeze" in its motion to avoid streaks or blurred images. The time delay between subsequent illumination pulses also need to be carefully chosen for particles to travel far enough to accurately determine the distance they have advanced, but on the other hand, a short enough interval so that no particle slips out of the light sheet due to an out of the plane motion. In addition we need enough particles

with a homogeneously distribution. How many particles that are "enough" depends on several factors and will be touched upon later. The frame size is restricted by the camera and lens in use and should be adjusted to capture the most relevant part of the flow.
By employing the technique of PIV we typically end up with quite large amounts of data. To handle and analyze big amounts of data we need sophisticated post-processing techniques based on statistical methods such as the cross-correlation function.

2.2.3 Theory of Cross-Correlation in PIV

Idea

Given two subsequent images, the idea is to find an Eulerian description of the velocity field. This can be done by first divide the raw image into a grid of smaller windows called subwindows, denoted I_W. Suppose now that red dots in figure 2.2 represents particles in the first image and that blue dots represents the same particles in the subsequent image. Then we want to find the same pattern of dots in the second frame as in the first, i.e the displacement of the particles during a time interval Δt. The idea is now to find out the distance and in what direction these particles have moved during the time interval Δt. This can be done under the assumption that, in each subwindow, all the particles travel at an uniform velocity. We then get after finding the correct pattern matching, a resulting ensemble velocity vector that can be seen as a pink vector, in figure 2.2.

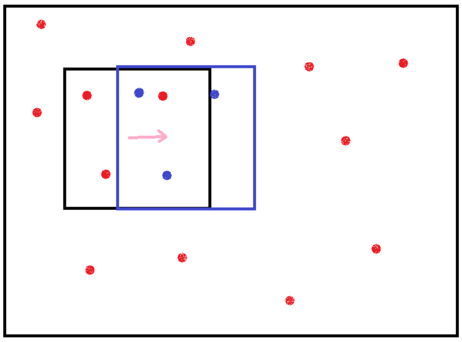

Figure 2.2: *An illustration of two subsequent subwindows with pattern match resulting in a pink velocity vector.*

This kind of pattern matching requires a metric to tell how different the pattern is. There are several ways of finding such a pattern but a common choice is the cross-correlation function, presented in an article from 1991 by Willert and Gharib (1991)[29].

Theory

A digitized camera image can, analogously to a one dimensional time series, be considered to be a two-dimensional signal field. Let us assume we are considering a discrete signal field that represents a sequence of images that are showing moving particles from a PIV experiment. As described above, these images or signal fields rather are divided into subwindows, conceptualized in figure 2.2.

So, in between two subsequent images there may be seen a spatial displacement of particles given that we have a fluid flow present in the illuminated plane. This displacement may be described as in the linear digital signal processing model shown in figure 2.3.

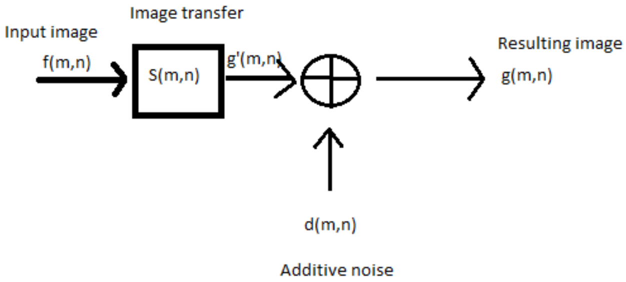

Figure 2.3: *A model describing the functional relationship between two successive frames.*

The sampled region $f(m,n)$ may be considered the input and the output function $g(m,n)$ as the corresponding sampled region of a subsequent image at a time Δt later. The spatial displacement function $s'(m,n)$ and the additive noice process $d(m,n)$ constitutes the system of which this displacement process is described. The noise function $d(m,n)$ is a result of several factors, among others, we have for example Willert (1991)[29]:

Particles moving out or in of the edges of the image frame during the time interval Δt.

Particles disappearing due to out of plane motion.

The number of particles present in the each sub window.

In summary one can say that a PIV experiment, is about finding the displacement function $s(m,n)$. This is the function that estimates the magnitude and direction of the pink velocity vector as shown in figure 2.2.

A way to mathematically describe how the output sample $g(m,n)$ relates to the input sample $f(m,n)$ as the discrete convolution of $s(m,n)$ and $f(m,n)$ is ,

$$g(m,n) = \left[\sum_{k=-\infty}^{\infty} \sum_{l=-\infty}^{\infty} s(k-m, l-n) f(k,l) \right] + d(m,n). \tag{2.27}$$

The displacement function $s(m,n)$ is in this case a Dirac delta function $\delta(m - i, n-j)$ displaced from the origin by i, j units and this displacement corresponds directly to the average displacement of the particles in the sampled region. If $d(m,n)$ are negligible and dividing this displacement with the time scale Δt we will obtain the velocity vector, $\boldsymbol{U} = \frac{\Delta \boldsymbol{x}}{\Delta t}$, in the sampled region, where $\Delta \boldsymbol{x} = (\Delta x, \Delta y)$ is the displacement vector and Δt is the time difference. Due to the discrete Dirac delta function, equation 2.27 does not allow for sub-pixel measurements. A statistical technique of spatial cross correlation to find the displacement function $s(m,n)$ were proposed by Willert and Garib(1991) [29]. The discrete 2-dimensional cross-correlation function $\phi_{fg}(k,l)$ of the sampled regions $f(m,n))$ and $g(m,n)$. It is a statistical technique and is here given as the expected value E,

$$\phi_{fg}(k,l) = E[f(m,n), g(k+m, l+n)]. \tag{2.28}$$

We can expand equation 2.28 to obtain,

$$\phi_{fg}(k,l) = \frac{\sum_{m,n} f(m,n) g(k+m, l+n)}{\sum_{m,n} f(m,n) \sum_{m,n} g(m,n)}. \tag{2.29}$$

Cross correlation is a match metric of the degree of similarity between pixel intensity of $f(m,n)$ and $g(k+m, l+n)$,see Brown (1992)[54].For an identical match between $f(m,n)$ and $g(k+m, l+n)$, a cross correlation peak will have a peak at the point k, l. Equation 2.29 will in general (if the particles we are looking at are bigger than one pixel) return a broader peak than equation 2.27 and can be interpolated to sub-pixel accuracy. The highest correlation peak is considered to represent the best match of particle images between the function $f(m,n)$ and $g(m,n)$.

Implementation

In this thesis the program HydroLabPIV, developed by Dr.Kolaas[28], have been used HydrolabPIV is an in house software of Oslo University that implements the cross correlation function as proposed in proposedby Willert and Garib(1991)[29]. In addition, HydrolabPIV uses a normalized cross correlation $ncc(r,s)$ function order to improve accuracy. Compare with a non-normalized cross correlation that will yield different maximum correlation values for the same degree on matching, depending on intensity values and pixel densities Raffel et al.(2018)[38]. The $ncc(r,s)$ function is given by

$$ncc(r,s) = \frac{num(r,s)}{\sqrt{den_1(r,s) den_2(r,s)}} \tag{2.30}$$

where

$$IJ = \sum_{i,j}\sum_{i,j} f(i,j) \sum_{i,j}\sum_{i,j} g(i,j) \quad (2.31)$$

$$num(r,s) = \sum_{i,j} f(i+r, j+s) \cdot g(i,j) - \frac{\sum_{i,j} f(i+r,j+s) \sum_{i,j} g(i,j)}{IJ} \quad (2.32)$$

$$den_1(r,s) = \sum_{i,j} f(i+r, j+s)^2 - \frac{\left(\sum_{i,j} f(i+r,j+s)\right)^2}{IJ} \quad (2.33)$$

$$den_2 = \sum_{i,j} g(i,j)^2 - \frac{\left(\sum_{i,j} g(i,j)\right)^2}{IJ} \quad (2.34)$$

The normalized cross correlation 2.30 return values in the range $[-1, \quad 1]$, and in the case of PIV images where all the intensity values are positive, in the range $[0, \quad 1]$. Note that $den_1(r,s)$ is the co-variance of $f(i,j)$ i.e, $E[(f - \mu_f)(f - \mu_f)] = E[f^2(i+r, j+s)] - \mu_f^2$, $den_2(r,s)$ is the co-variance of $g(i,j)$ which have been re-written in similar fashion as $f(r,s)$ and $num(r,s)$ is the co-variance of $f(i,j)$ and $g(i,j)$ which by the linear properties have been rewritten to $E[(f-\mu_f)(g-\mu_g)] = E[(f(i+r,j+s)g(i,j))] - \mu_f \mu_g$, where $E(f(i,j)) = \mu_f$ and $E(g(i,j)) = \mu_g$. Padfield (2012)[30], showed that it is possible to compute the normalized cross correlation with a Fast Fourier Transform (FFT) which significantly speeds up process of the pattern matching.

2.2.4 Error and challenges in PIV

It is important to identify the sources of error while conducting a PIV experiment since they will directly affect the overall accuracy of the measurements. Errors are introduced in a variety of ways and by identifying them we can possibly reduce them to a minimum and thus get a more accurate and reliable result. The quality of the experimental set-up will be an contributing factor here as well as the evaluation technique, i.e the cross correlation but also physical variations in the flow itself such as the variations of the Reynolds number (Raffel, 2018)[38].

The total error source may be decomposed up into to types, a biased part $< (\epsilon_{int}) >$ and a random part $\sigma(\epsilon_{int})$,Coleman (2009)[31]. A biased error will typically not vary during an experiment and can be thought of as systematic in it's difference from the true value whereas a random error will change throughout in both magnitude and direction.

To this authors knowledge, recent papers that have been published on the topic of uncertanities in PIV have with a few exceptions been mainly focused on $a - posteriori$ techniques which is beyond the scope of this study. Masullo and Theunissen(2016)[14] developed a vector validation technique in the presence of clusters of outliers and proposed an advancement of earlier detection schemes presented by Westerweel and Scarano(2005)[12]. Kislaya and Sciacchitano(2018)[15] made use of optical diffusers to increase the image particle diamater in an attempt to reduce peak looking effects. Xue et al.(2014)[16] posit that correlation signal to noise ratio(SNR) calculated from the correlation plane can be used to quantify the quality of the correlation and to determine the uncertainty of an individual measurement. Charonko and Vlachos(2013)[17] demonstrated a method, based on the cross correlation peak, for estimating the uncertainty bounds to within a given confidence interval for a specific individual measurement. Wieneke(2015)[11] derived a relationship between the standard deviation of the intensity differences in each interrogation window and the expected asymmetry of the correlation peak, which they converted to the uncertainty of the displacement vector.

Ayati et al. (2012)[32] used the work from (Herpin, 2008)[37] whom in his turn combined methods and results from earlier studies (Focault (2003)[33], Lecordier and Trinit (2003)[34], Westerweel (1997)[35] and Soria (2006)[36]) in order to establish pre-determined or $a-priori$ estimates of the uncertainties in the measurements. These $a-priori$ estimates will certainly not cover all sources of error that exist but they may perhaps give a sense of the precision and some weaknesses of the experiments in this study.

Non-optimal concentration and non-uniform distribution of particles over the I_W

The tracer particles works as information carriers and are utilized to detect the magnitude and direction of the flow. Therefore it is important that enough particles is present in each I_W, that they are of the correct apparent size and also that the particles are evenly distributed throughout the flow.
The particle size is by Cameron (2011)[39] and Raffel et al. (2018)[38] recommended to lie in the range of 2-4 pixels and unfortunately, all the apparent particle sizes d_p in the current experiments does not land within this range but around 1.5 in the gas phase and 2-2.5 in the water phase. The recommended particle density per interrogation window I_W is 5-15 particles by Thielicke et al. (2014)[40]. [40]. This is easier to adjust in the post processing by just alter the size of the interrogation window and in this study all cases lies between 7-30 particles per interrogation window. The average number of particles N_p were approximated by converting PIV images into a binary image using an appropriate threshold to differentiate between particles and the background. Then by using the function *regionProps()* in $Matlab$ an estimation of the average diameters of the connected areas were computed. To ensure a homogeneously distribution of particles it is, in the water phase, important to mix the particles well into the water tank as well as run the loop for some time before every data collection. For the air phase, it is necessary to place the PIV section long enough down stream of the atomizing nozzle seeder, such that the heavier non-naturally buoyant particles will disappear from the entraining flow. However, even though the true distribution of particles is homogeneously distributed we may have non-homogeneously light scattering over the field of view, or other reasons, that makes the acquired image distribution to be non-homogeneous. Therefore the apparent particle distribution of the images were visualized through a 2-D histogram of the data density made in Matlab. The script make use of the particle coordinate positions from the binarized image, these positions are then interpolated to their nearest evenly spaced integer grid, which is defined before hand, see Appendix for more information about the scripts.

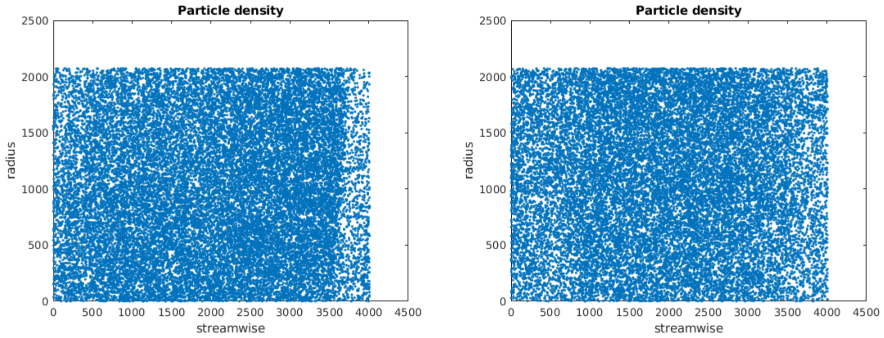

Figure 2.4: *The estimated particle density from which the histograms in figure 2.5 where calculated with the Flashe case on the left and the Polyamid case on the right. The lack of particles on the right is due to a black tape that were glued on the backside of the pipe to mitigate reflections finished just where the lower density starts.*

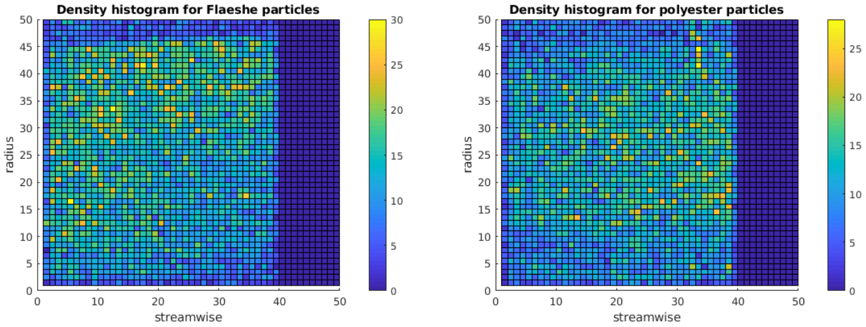

Figure 2.5: *Histograms from the density script. On the left hand side is the density of the Flaeshe particles visualized from a single image. On the right hand side we have the particle density of the Polyamide particles, also from a single image. The color bar goes from yellow(relatively high) to blue(relatively low) density.*

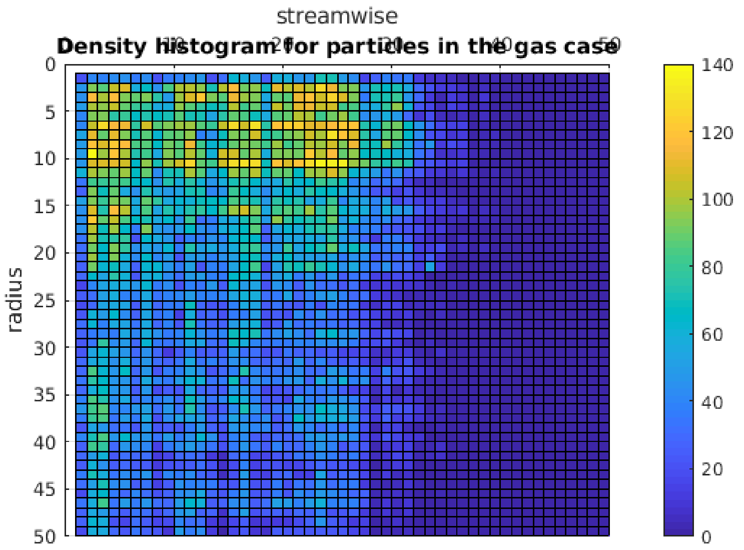

Figure 2.6: *A single image instant particle density visualized for the gas phase. It seems like the density of the top of the pipe is a higher than the lower part as well as the density on the left hand side compared to the outer right. This may be a cause for concern regarding the accuracy of the gas phase.*

Foucault et al. (2003)[33] showed that the random error $\sigma(\epsilon_{int})$ could be approximated to $0.006px$ and that it was one magnitude larger than the bias error $< \epsilon_{int} >$, provided that the image particle size and concentration over the I_W is optimized around $2.2px$ and 10. The particle size and window concentration in this work can be seen in table 2.2and the scripts to calculate the number of particles N_p and the image particle density ρ_p can be seen in Appendix6.2.

Phase	**Tracer type**	N_p	N_p/I_W	$\overline{d_p}$
Water	Polyamide	22000	10-11	2.5px
Water	Flashe	24000	10-11	2px
Gas	Water	75000	10-20	1.5px

Table 2.2: *A table with average values for some key parameters for each experiment. Phase indicates the working fluid, $Tracertype$ what kind of tracer, N_p the number of apparent particles, N_p/I_W particles per interrogation window and d_p the mean image particle size.*

Interrogation algorithm and peak locking

Peak locking is a term that describes a common displacement bias in PIV experiments where the measured displacement of the particle image location tend to bias towards integer values. Christensen (2004)[41] showed that PIV measurements in turbulent flows are especially sensitive to peak-locking. Occasions where displacements are small, under 0.5 pixels in magnitude, can be especially problematic since they tend to be locked towards 0 pixels displacement and thus being underestimated in magnitude. Great care must therefore be taken in the experimental set up proceedings to get large enough displacement in the fluctuating velocities to avoid this phenomenon, which can be especially prevalent in the wall normal velocity component. Particle sizes should be between 2-4 pixels in order to minimize the peak lock effects, Westerweel (2010)[43], which, as mentioned in the previous section, is not the case for all experiments in this study. Therefore, the gas phase in particular, but also the water case with Flashe particles might be prone to peak looking due to their smaller than recommended mean image particle size. Moreover, according to Michaelis et al. (2016)[42] it is also favorable to use a CCD camera (as used in this experiment) with small pixels (5-10μ m) to reduce the peak-locking problem. Michaelis et al. (2016)[42] investigated *a priori* and *a postpriori* methods for PIV. The *a priori* methods are all set to optimize the particle image size with camera filters etc. to be within the recommended values, which in this study haven't been done. As for the *a postpriori* methods it is proposed to use a spline or bilinear interpolation method to estimate the highest correlation peak. In *HydrolabPIV* several different interpolation methods can be employed but here have the Lanczos resampling method which is based on a *sinc* kernel been used as it is recommended by Koolas (2017)[28] for particles in the 2-4 pixel diameter range which seem to be the case for the particle distributions in this work, see figure 2.7a and 2.7b. In addition, evidence has been presented that a *sinc* interpolation kernel yields minimal peak locking influences for adequately resolved particle images, see Roesgen (2003)[44]. Beneath in figure 2.8, 2.9 and 2.10 are histograms for the displacement in U,u' and v' for one case of both particles. The two shows strong signs of peak locking in the streamwise component U. The turbulent fluctuations are Gaussian distributed for the Polyamid case which indicates no peak locking effects, whereas the Flaeshe case shows sign to have peak lock effects in the fluctuating parts as well and especially in the v' component.

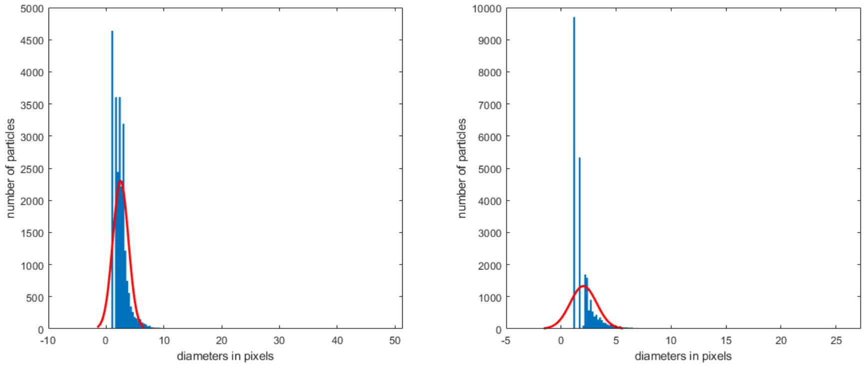

(a) *Polyamid*

(b) *Flaeshe*

Figure 2.7: *A histogram of the estimated particle distribution in pixels for Polyamide and Flashe particles, see Appendix 6.2 for calculations of the distributions.*

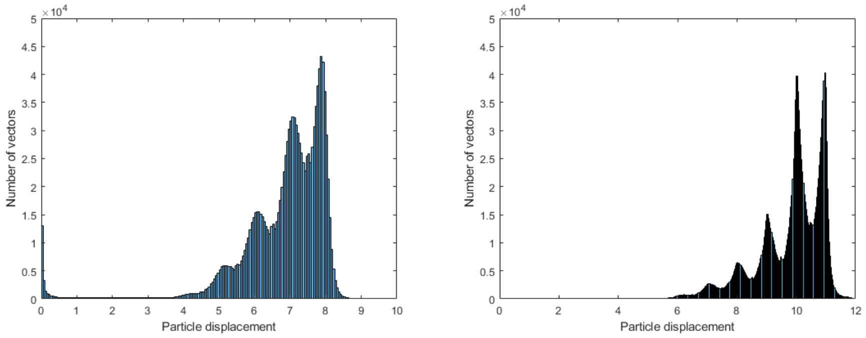

(a) *Polyamid*

(b) *Flaeshe*

Figure 2.8: *A histogram of the particle displacement for both the* $Re_{U_b} = 35k$ *cases for the stream wise velocity* U*. An indication of peak locking is observed for both tracer particles due to the bias towards integers in the displacement value.*

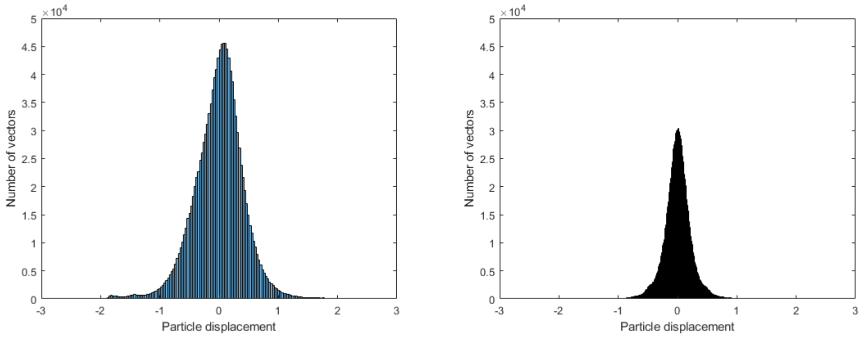

(a) *Polyamid u component*

(b) *Polyamid v component*

Figure 2.9: *Histogram from the polyamid* $Re_{U_b} = 35k$ *case. Gaussian distribution on the left for the fluctuating u-component and on the right as well for the fluctuating v-component.*

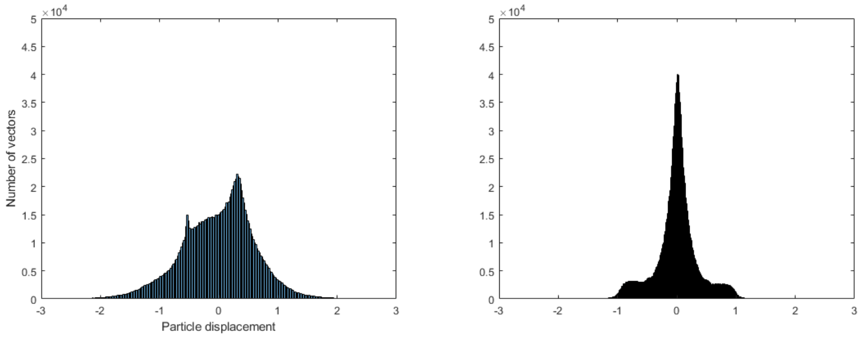

(a) *Flaeshe u component*
(b) *Flaeshe v component*

Figure 2.10: *Histogram from the Flaeshe* $Re_{U_b} = 35k$ *case. Gaussian distribution on the left for the fluctuating u-component and on the right a bias towards integers for the fluctuating v-component.*

Effects of background noise and reflections

The measurement signal is contained in the recorded intensity of the PIV image in addition to a variety of noise sources. By dividing the strength of the signal with the noise, we get the signal to noise ratio (SNR). The signal to noise ratio governs the accuracy of the cross correlation, where a low SNR value will give a poor measurement and vice versa. The noise effects can be reduced in severity by optimizing the size of the interrogation window I_W, the particle diameter d_p and particle density N_p/I_W to align with the values recommended in the literature. There are however certain noises that can not be dealt with in any convenient matter such as reflections from the pipe wall or condensation of the pipe wall(relevant for the gas phase). Some reflections will completely overpower the measurement signal, making it very difficult to recover any information. An easy way to deal with reflections is to mask them away, unfortunately resulting in a complete loss of information in the masked area.

In this work a background subtraction have been done in an attempt to reduce the noise. Prior to the PIV interrogation a background image are created by scanning through all images for each experiment, finding the average low corresponding pixel value in all selected images. Next a subtraction of the background image on every single image is performed creating a set of new images with an assumed lower noise level, see appendix6.2. In figure 2.11 are two resulting histograms of the SNR field showing excellent SNR values of around 20 as Scharnowski and Kähler(2016)[4] showed that a SNR value above 3 is a sufficient signal to noise ratio.

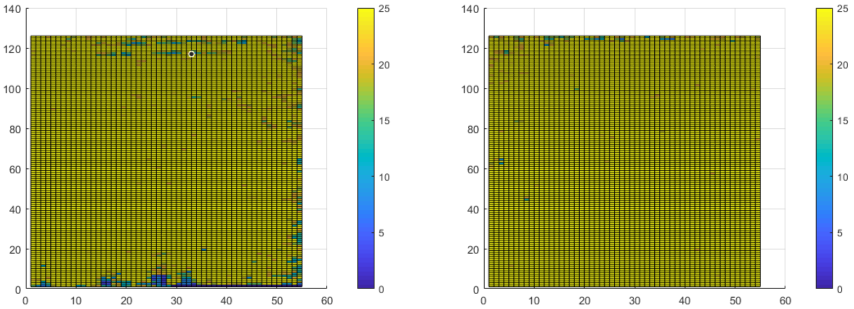

(a) *Polyamid* $I_W[128 \quad 40]$ (b) *Flaeshe* $I_W[128 \quad 40]$

Figure 2.11: *A histogram of the SNR fields computed from the Hydrolab PIV code showing both the* $Re_{U_b} = 35k$ *cases.*

Unpaired particles due to out-of-plane motion

The experimental set-up in this study captures a 2-D representation of the flow which means that motion in the opposing direction of the laser sheet can neither be measured or observed in the final data. Due to the 3-D characteristics of the present turbulent flow regime we will have a component w_{rms} and need to consider tracer particles that are moving out of the laser sheet in between subsequent images, which in turn may result in a weaker signal and that thus will affect the accuracy of the experiment. The out of plane component w_{rms} can in magnitude be related to the friction velocity u^*. From Harpin et al. (2008) [37] we may assume a Gaussian distribution of the total width giving $K = 3w_{rms} = 3u^*$. In the gas case of $Re = 44k$(which can be considered to be the "worst" case in this study) with a friction velocity of $u^* = 0.365m/s$ and a time delay of $\Delta t = 50\mu s$ we will thus get a maximum out of plane displacement of $dw_{\Delta t} = 0.036$mm. Next by scaling the maximum displacement with the laser sheet thickness $I_z = 1mm$ we get $dw_{\Delta t} = 0.054 I_z$ and can thus conclude that most of the articles will remain within the laser sheet during interrogation.

Non-uniform displacement over the I_W due to mean velocity gradients and turbulent fluctuations

The assumption that we have a uniform flow within each interrogation window I_W can be a significant source of error closer to the edges of the pipe where there are high velocity gradients. The gradient can lead to a broaden correlation peak and might even split up into multiple peaks, Scarano (2002)[47]. This error can somewhat be reduced by using smaller I_W but in cases when the gradient is large it might not be enough. In addition to this we also have the turbulent components that will result in local discrepancies of the particles between corresponding image pair.

It is possible to evaluate the gradient in the heart of the logarithmic region (which is where the peak of the streamvise rms-profile u^* lies) by using the formula proposed by Herpin et al.(2008)[37]:

$$(\frac{du}{dy})_{I_W,\Delta t} = \Delta t \frac{u^*}{px_{obj}} \int_{y^+ - \frac{I^+_{IW}}{2}}^{y^+ + \frac{I^+_{IW}}{2}} \frac{dU^+}{dy^+} dy^+ \tag{2.35}$$

where

$$\frac{dU^+}{dy^+} = \frac{1}{Ky^+} \quad \text{for} \quad y^+ > 100^+ \tag{2.36}$$

They scaled the displacement difference with the particle image diameter px_{obj},and K is the Von karmán constant $K = 0.41$, Δt is the time difference between subsequent images, u^* is the friction velocity, U^+ is the non dimensional velocity scaled with the friction velocity and y^+ is the non dimensional wall coordinate made dimensionless with the viscosity and the friction velocity.

The gas phase case with a Reynolds number of 44000 and with an interrogation window I_W of $40x40$ where estimated to have a maximum particle displacement gradient $\frac{du}{dy})_{I_W,\Delta t}$ of about 0.3 pixel. This may be especially problematic when we have a relatively small particle image size, where peak looking might be in effect, and it might contribute quite significant to the error in the peak of the rms profiles. The rest of the results are presented in the Result section.

Passivity of tracer particles

Another important aspect in PIV is the tracers particles ability to reflect the dynamics of the flow. To "slow" particles will lead to systematic errors in the measurements and we therefore need to investigate this to make sure that it will not affect our results. A number of important quantities that should be considered are presented by Ayati et al. (2014)[32]:

- The ratio of particle density to the fluid density, $r_p = \frac{\rho_p}{\rho f}$ which in the gas phase is of the order of 1000 and in the liquid phase of the order of 1.

- The Reynolds number that characterize the particle motion, which is defined as $Re_p = \frac{d_p U_{rel}}{\nu}$, where d_p is the particle diameter, ν is the fluid kinematic viscosity and U_{rel} is the relative velocity between the particle and the fluid.

- The drag coefficient.

- The Stokes number $St = \frac{\tau_p}{\tau_f}$ (the ratio of particle response time to the time scale of the turbulence).

Stokes(1851) showed that for small particles with negligible Reynolds numbers the particle time constant is

$$\tau_{p,Stokes} = \frac{(2\rho_p + \rho_f)d_p^2}{36\nu}. \tag{2.37}$$

ρ_p is the density of the particle, ρ_f is the density of the fluid, d_p^2 is the particle diameter and ν the kinematic viscosity. The particle time scale where derived by, Fessler and Eaton (1999)[45] to be

$$\tau_p = \frac{\tau_{p,Stokes}}{[1 + 0.15Re_p^{0.687}]} \tag{2.38}$$

which can be reduced to

$$\tau_p = \tau_{p,Stokes} \tag{2.39}$$

at the limit $Re_p - > 0$.

Turbulence is, as mentioned earlier, a multi-scale phenomenon in both time and space. The time scale thus vary, depending of what scale of turbulence we are considering. It is bounded by the Kolmogorov time scale at the lower limit and at the upper limit by the so called integral time scale which is sometimes referred to as the *largest eddy turnover time* in the literature. Looking at the Stokes number $St = \frac{\tau_p}{\tau_f}$ it makes sense to use the upper time scale $\tau_f = \frac{L}{U}$ in this study to include the largest Stokes numbers that are present in the flow. Fessler and Eaton(1999)[45] concludes that particles with a $St \leq 10$ are suitable to capture the turbulent dynamics in the flow and as can be seen in figure 2.12 even for a large water particle of $50\mu m$ the Stokes number are very moderate. This is confirmed in the work by Lau and Nathan(2016)[46] where it is shown that the turbulence profiles diminishes considerably in strength as the Stokes number gets higher than 5.

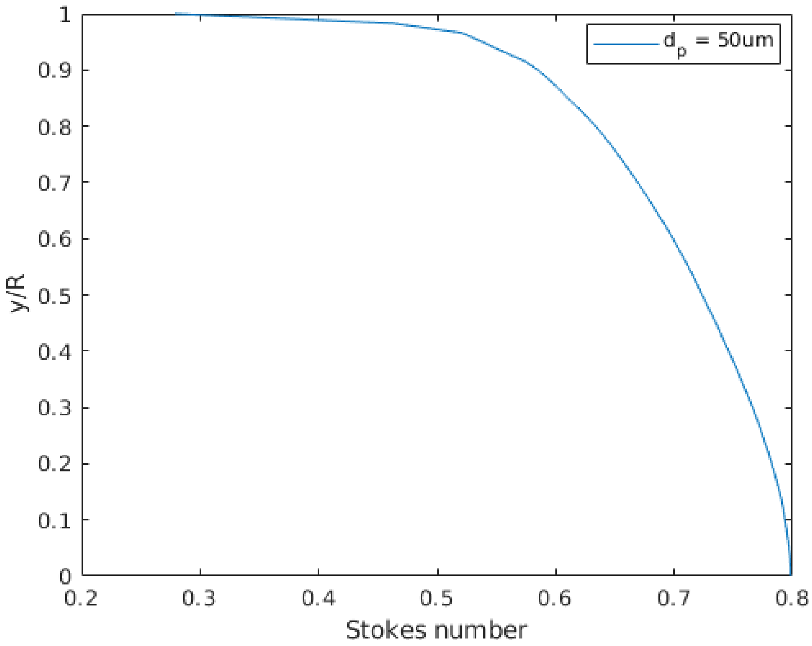

Figure 2.12: *Stokes number distribution along the radius for a large water particle in the gas experiment* $Re_{U_b} = 44k$.

For neutrally buoyant particles where the particle density approaches the fluid in which it is immersed, as is the case for the water experiments, the time scale of the particle can by Raffel et al.(2018)[38] be defined as

$$\tau_p = \frac{d_p^2 \Delta\rho}{18\mu} \tag{2.40}$$

where $\Delta\rho$ is the difference in density between the liquid and the particle. As $\Delta\rho$ approaches zero, so is the Stokes number $St = \frac{\tau_p}{\tau_l}$. Both the Polyamide and the Flashe particles can thus be considered passive and maintain a good tracking fidelity.

Spatial dynamic range

Two important questions are: what scales that are present in the turbulent fluid flow and what scales can the PIV system detect and resolve?
The spatial dynamic range(SDR) of a PIV system determines what scales of the fluid flow that can actually be measured and thus what turbulent scales that can be resolved. The SDR are bounded by a upper and lower limit. The upper limit SV_{max} is determined by the extent of the field of view. Whereas the lower bound is determined by $SV_{min} = 2I_W$, see Herpin et al. (2008)[37]. The theoretically achievable SDR where defined by Adrian(1997)[48] as the ratio

$$SDR = \frac{SV_{max}}{SV_{min}} \tag{2.41}$$

which in the image space will be

$$SDR_x = \frac{\Delta x_{max}}{2I_W}, \quad SDR_y = \frac{\Delta y_{max}}{2I_W} \tag{2.42}$$

where Δx_{max} is the sensor size in pixel ($4008px \times 2672px$ in our case) and I_W the size of the interrogation window. It is however worth to note that by decreasing the size of the I_W we are not necessarily able to detect smaller scales, since the signal to noise ratio will go up as it decreases.

The scales that are present in the fluid flow are bounded on the lower side by the Kolmogorov length scale $\eta = (\frac{\nu^3}{\epsilon})^{\frac{1}{4}}$ where ν is the kinematic viscosity and ϵ is the dissipation rate per unit mass whereas the upper limit is determined by the physical boundaries of the fluid. The smallest structures were shown by Stanislav et al.(2008)[51] to dissipate to fast to be considered coherent[1]. They also showed that the smallest coherent structures where about 10 Kolmogorov length scales η in diameter which corresponds to $y^+ = \frac{yu^*}{\nu} = 20^+$ which is a dimensionless wall unit where the characteristic length y is scaled with the kinematic viscosity and the friction velocity.

Herpin et al.(2008)[37] suggest that the SDR of a PIV system should be compared to the range of the coherent structures W_{str} in the fluid,

$$W_{str} = \frac{3\delta^+}{20^+}, \tag{2.43}$$

where δ^+ is the diameter of the pipe expressed in dimensionless wall units. δ^+ is the size of the *large scale motions* defined by Adrian(2007)[49]. Thus, W_{str} is the ratio of the maximum size large scales motions δ^+ over the minimum size of the small scale coherent structures. Herpin et al.(2008) concludes that a full resolution of the flow structures requires $SDR = W_{str}$.

---

[1] A *coherent* structure where defined by Robinson (1991)[50] as: *"3d regions of the flow over which at least one fundamental flow variable (velocity component, density, temperature etc.) exhibits significant correlation over a range of space and/or time that are significantly larger than the smallest local scales of the flow"*

Chapter 3

Experimental set-up and method

3.1 Experimental Set-Up

The experimental campaign in this study where conducted in the HydroLab at the University of Oslo using a 2D-PIV system.
All experiments were conducted in a horizontal 31 meter long PVC pipe with an internal diameter D = 10 centimeters. The pipe consisted of adjacent sections of 3.5 meters each and were connected with annular joints which are stabilized by collars to vertical beams, that support the whole structure. The vertical position of the test section are adjusted with a digital spirit level. Working fluids were air and water with an average temperature of $21°C$, both at atmospheric pressure.

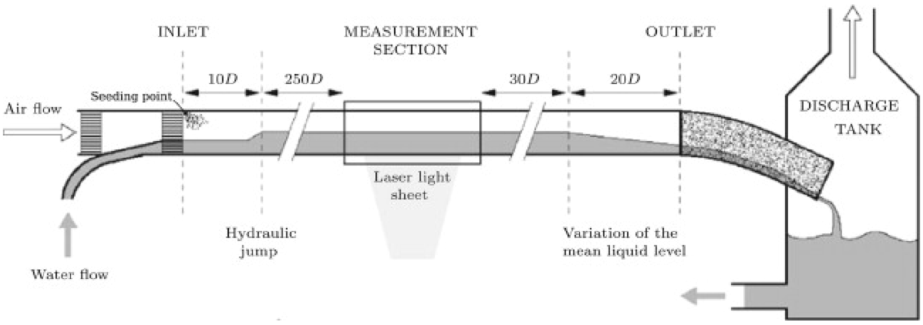

Figure 3.1: *Schematic overview of the flow rig. The grey area in the end of th pipe section are a flexible duct that connects the outlet with the discharge tank and the striped areas in the inlet represent honey comb flow straighteners.*

A 5 cm I.D tee branch at the pipe inlet leads in the water phase. The water phase then pass through honey comb flow straighteners to minimize unwanted disturbances introduced in the transition process from tee to pipe. At the outlet, about 50D downstream after the PIV section, the pipe discharged into a separating tank at atmospheric pressure through a flexible plastic duct. This flexible duct were lifted and raised above the level of the non-flexible pipe section in order to establish a single water phase flow in cases where this were a necessity.

Water was circulated with a 1.4kW centrifugal pump with a maximal flow rate of $90m^3/h$ and the gas flow where produced by a frequency regulated fan. Water and air were recirculated from the bottom and top exits of the tank, respectively. Mass flow rates were measured by two flow meters. The water phase were measured by a Endress Hauser Promass with an accuracy of $\pm 0.2\%$ and the gas phase were measured by a Emerson Micro Motion Coriolis flow meter with an accuracy of $\pm 0.5\%$. A SMAR LD 301 differential pressure gauge placed above the centerline measured the static pressure drop between two taps, separated by a distance of 12.4 meters and located at the top of the pipe, one up and the other down stream of the PIV section. Bulk and friction velocities were calculated using a density of 997 kg/m^3 for water and 1.2 kg/m^3 for air. In order to calculate the friction velocities, the pressure drop measurements were also used. Reynolds numbers, based on the bulk velocity, in the water phase ranged from $10 - 35 \times 10^3$ and in the gas from $5 - 70 \times 10^3$.

The PIV measurements in a vertical plane were performed in a channel section located 260D downstream from the inlet and 50D upstream from the outlet. According to Wang Zhi-Qing (1982)[52] the hydrodynamic entry length $L_{turbulent}$ for a turbulent flow can be approximated by the formula

$$L_{turbulent} = 1.395 \times D \times Re^{1/4} \tag{3.1}$$

where D is the pipe diameter and Re is the Reynolds number based on the bulk velocity.By 3.1 we get values around $L_{turbulent} \leq 25D$ for all test cases. We can thus consider the flow to be fully hydro-dynamically developed at the PIV section and the flow characteristics will no longer change with increased distance along the pipe. This is an important assumption and is exploited in the post processing and will be touched upon later. The test section consisted of a rectangular PVC box that where filled with water or air depending on the phase that were measured. A design that reduces the distortion of the signal caused by the pipe wall. Furthermore, the inside of the pipe wall, in the PVC box section and adjacent to the camera, is prepared with a black tape to reduce undesirable reflections, see figure 3.3.

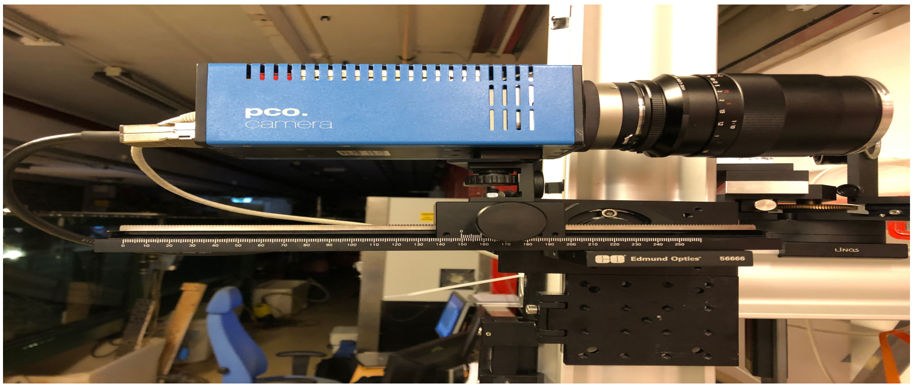

Figure 3.2: *A close up of the PCO4000 camera.*

A Nd:YAG double pulsed laser of 135mJ produced the illumination of the 2D light sheet, and the images were recorded with a 16 bit PCO.4000 camera at a frequency of 0.3 hertz. The camera was placed about 30 cm from the outer pipe wall at a 0° angle from the center-line, giving a field of view of about $15 \times 10 cm^2$. The horizontal camera position did however vary somewhat between experiments and thus giving a slightly different field of view.

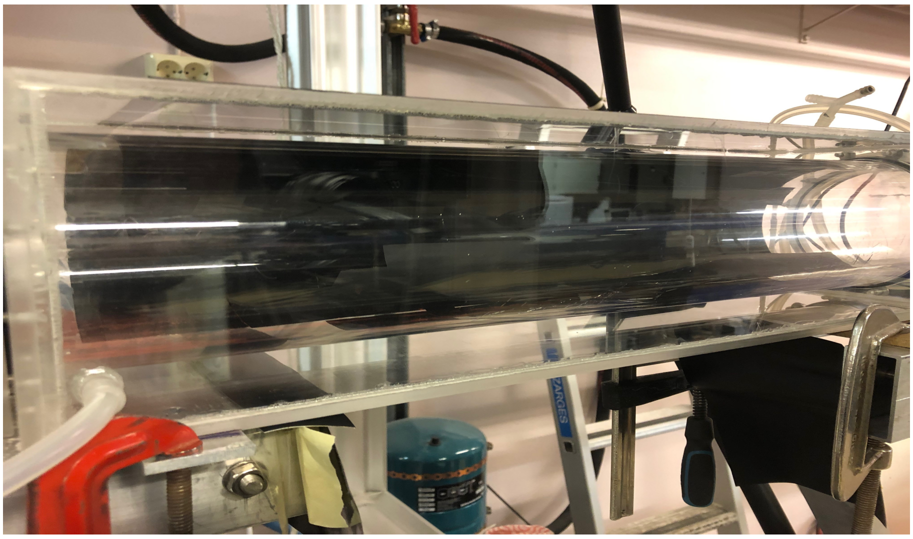

Figure 3.3: *A close up of the rectangular PVC-box.*

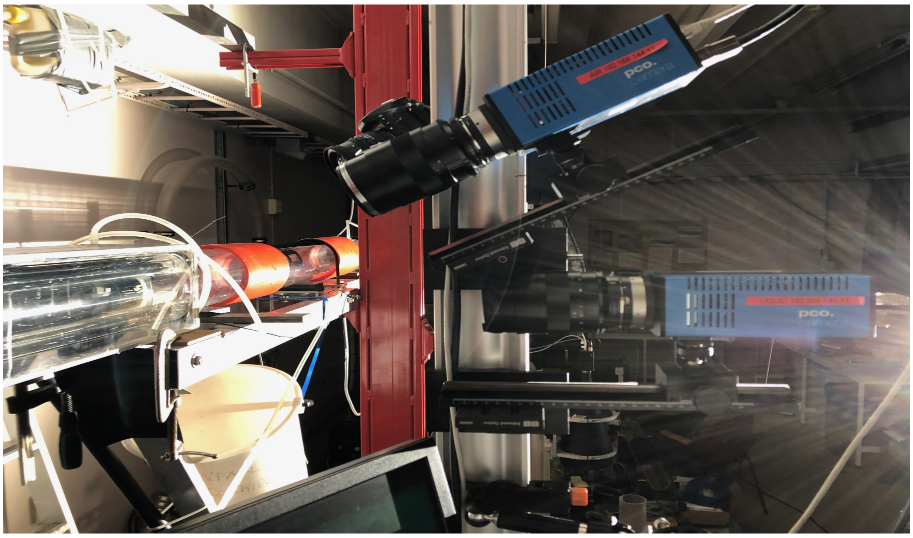

Figure 3.4: *A picture showing the PIV section enclosed by the PVC box on the left hand side and on the rightwe see the PCO.4000 camera (lower cam) that where used.*

The water phase was seeded with two different kinds of particles. The first particle was commercial ***Polyamide*** particles with a diameter $d = 50 \mu m$ from Dantec Dynamics. These particles are naturally buoyant, round and suitable for water flow applications. The other particles where made of dry orange fluorescent ***Flashe*** color and where prepared in the lab, see Appendix 6.1. These particles had an mean average diameter distribution of $d = 2 - 10\mu m$ are not spherical and where close to naturally buoyant

The particles where added in to the discharge tank and thereafter circulated in the loop in order to get a homogeneously distribution of particles before every run. The tank where emptied and cleaned out between experiments to not mix particles. During the expeirment with the Flashe particle an orange filter from B&W where used to block the intense green laser reflections from the laser and to allow the passage of the light emitted by the fluorescent Flashe particles.

The gas phase where seeded with water droplets provided by a high pressure atomizing nozzle supplied with filtered tap water and introduced at the seeding point as shown in figure 3.1 or about 260D downstream of the PIV section. The nozzle produces around 10^{10} particles per second where 72% of the droplets have a diameter below $6\mu m$ according to specifications from the manufacturer. Heavy particles quickly dropped to the floor of the pipe due to the gravitational pull. This combined with particles that smashes into the walls, creates a thin film that flows at the bottom of the pipe, and actually creating a multi phase flow regime of air and water. Enough particles were however carried with the flow to get a sufficient amount of particles 260D downstream at the PIV section.

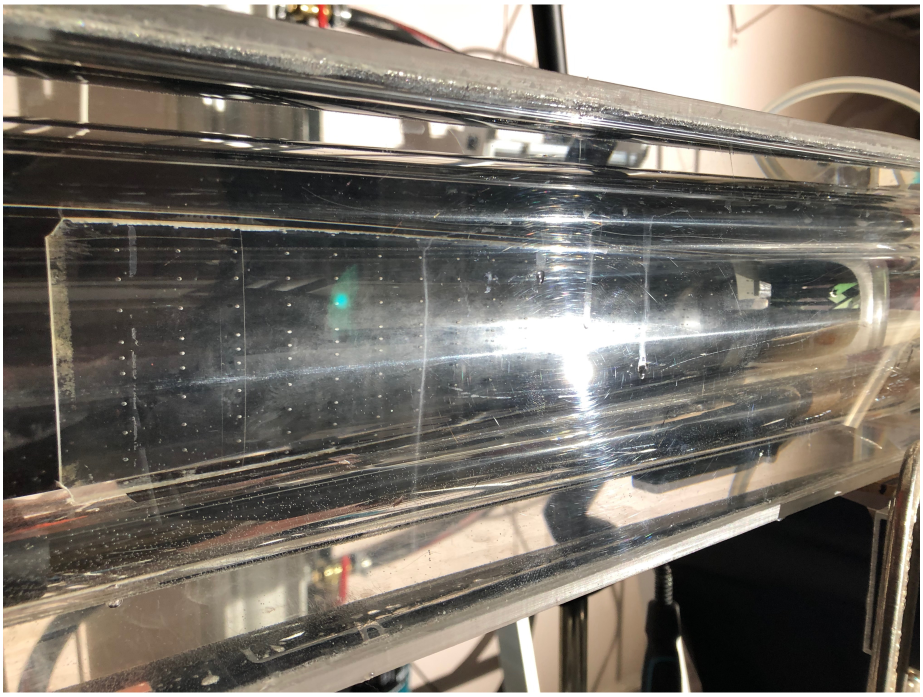

Figure 3.5: *A picture showing the plastic coordinate map as it is placed inside the pipe.*

A calibration image of a plastic map with an uniform grid, as shown in figure **??**, where used to map the pixel space to the physical space. A least squares bi-cubic fit is used to interpolate between the two spaces. A bi-cubic fit is used rather than a linear fit to account for the distortion created by the curved pipe wall. The same or a very similar set-up have been used in works by among other Ayati et al.(2014)[32]and Sanchis and Jensen(2011)[53]

3.2 Challenges

During the experimental campaign I've encountered many problems, made several mistakes and have had a number of unsuccessful attempts of gathering data. Some problems where mayor whereas others were minor. Beneath are a few of those that I think are particularly worthwhile to mention since they may affect the gathered data and thus manipulate the final results, if not handled with care.

3.2.1 A foggy pipe

During the gas phase acquisition there were a problem with a increasing fog layer inside of the pipe, as can be seen in figure 3.6a to the left in fig 3.6. This problem is greatly affecting the image quality in a negative way and can sometimes even destroy the whole signal by covering the particles with noise, making the acquired images useless. This phenomena usually started at the pipe bottom and climbed it's way upwards of the pipe wall vertically. By assuming a symmetric flow, it is possible to run experiments until the fog reached mid level and only using the upper half of the acquired images.

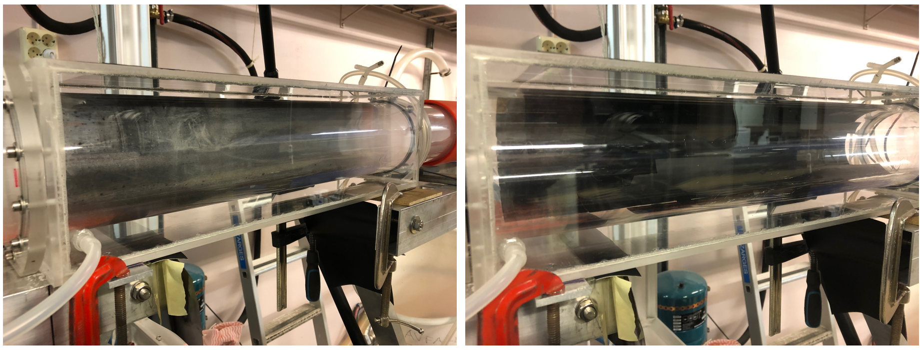

(a) *An image of the PIV section showing fogginess inside of the pipe wall.*

(b) *An image of the PIV section without fogginess.*

Figure 3.6: *A contrast between a foggy pipe to the left and a clear pipe to the right*

This phenomena does not seem to have any obvious solution other than some post processing techniques, such as subtraction of the background gradient, and are an event that are not always present, but seems to occur when the weather conditions are humid.

3.2.2 Set-up of Single Phase flow

It turned out to be a bit more tricky to run a single phase flow experiment than anticipated. An attempt was first made where a stopper/plug was placed a few diameters D distance downstream from the PIV section. This where very efficient in regards to obtain a single phase flow, but on the other hand, strongly affected the flow characteristics by skewing the velocity field. Another attempt was then performed where the flexible part in the end of the pipe were lifted, as explained earlier. This was almost successful, was it not for a Taylor bubble, as in figure 3.10, that where sitting right under the PIV section, creating a multi-phase flow regime rather than a single phase regime.

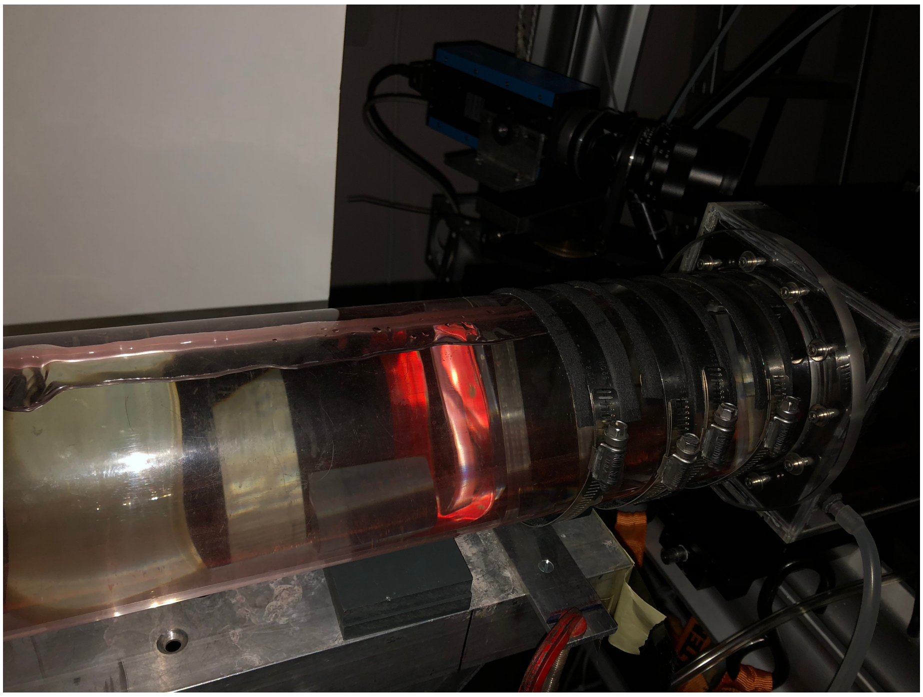

Figure 3.7: *An image showing a Taylor bubble, right before the PIV section, which reaches over a distance of 1.5-2 meters.*

This created a non-symmetrical flow pattern and needed to be addressed. The cause of this was probably due to a not perfectly horizontal pipe, but a pipe with a slight upwards bend, where the PIV-section where the highest point. By manipulating the highest point to occur downstream of the PIV-section, we were able to "push" the bubble further downstream such that it did not affect the measurement section. A way to $a-posteriori$ make sure that the mean velocity profiles were symmetric and that we thus have a single phase flow, is to compare the mass flow rate(measured by a Endress Hauser Promass with with an accuracy of ±0.2%) with a flow rate based on an experimental velocity profile. The mass flow rate is defined by the integral,

$$\dot{m} = \iint_A \rho \bar{U}(r) \cdot d\bar{A} = \rho \int_0^{2\pi} \int_0^R \bar{U}\bar{i} \cdot \bar{i} r dr d\theta = \rho \int_0^{2\pi} \int_0^R U r dr d\theta, \qquad (3.2)$$

defined over the intervals $0 < r < R$ and $0 < \theta < 2\pi$ where A is the area of the pipe, $\bar{U}$ the velocity vector and U is the streamwise velcoity component, r is the radial coordinate, θ is the angle and ρ is the density of the fluid. 3.2

were approximated by an algorithm that implemented the trapezoidal rule, see appendix.

3.2.3 Reflections

Reflections is an unfortunate thing that comes along with PIV experiments in general and especially in cases with such powerful lighting sources as the lasers used in this study in combination with a curved transparent pipe wall. They might turn out a great concern when they are stronger than the signal itself and actually drowns the specific area in noise resulting in a complete loss of information. In such cases the only remedy, known to this author, is to cut away the polluted part. Other times we are more fortunate; as when reflections are less profound, they can be handled appropriate by subtracting the background gradient.

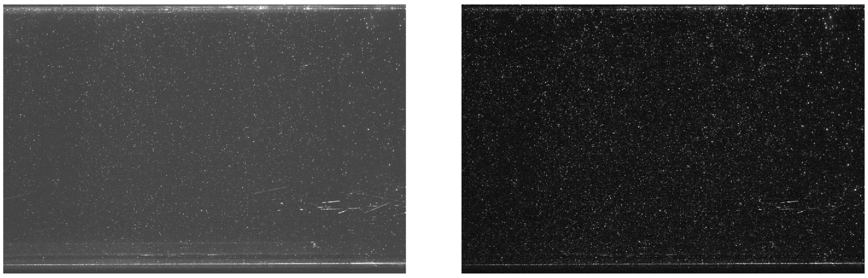

(a) (b)

Figure 3.8: *Example of a reflection (lower right corner) that could not be removed or mitigated with the post processing techniques that were used in this study. Left image is original whereas the right image is exposed to a background subtraction.*

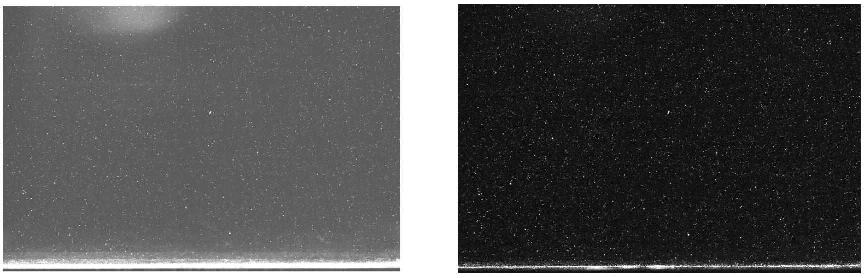

(a) (b)

Figure 3.9: *Example of a reflection (at the top left) that could be mitigated with the post processing techniques that were used in this study. Left image is original whereas the right image is exposed to a background subtraction.*

3.2.4 Pressure drop

The important pressure drop that are used to calculate the friction velocity were very unstable and unreliable for all the polyamid cases and was not working at all for any of the flashe cases. Events with a measured negative pressure drop, which is impossible, occurred and in general a highly fluctuating measurement was observed and no convergence around any certain number could be seen. However, since this thesis aims to compare two different tracer particles, the two will be subject to the about the same bias error regarding the normalization's of the turbulence profiles and thus the comparison should still be relevant and perhaps give some objective insight.

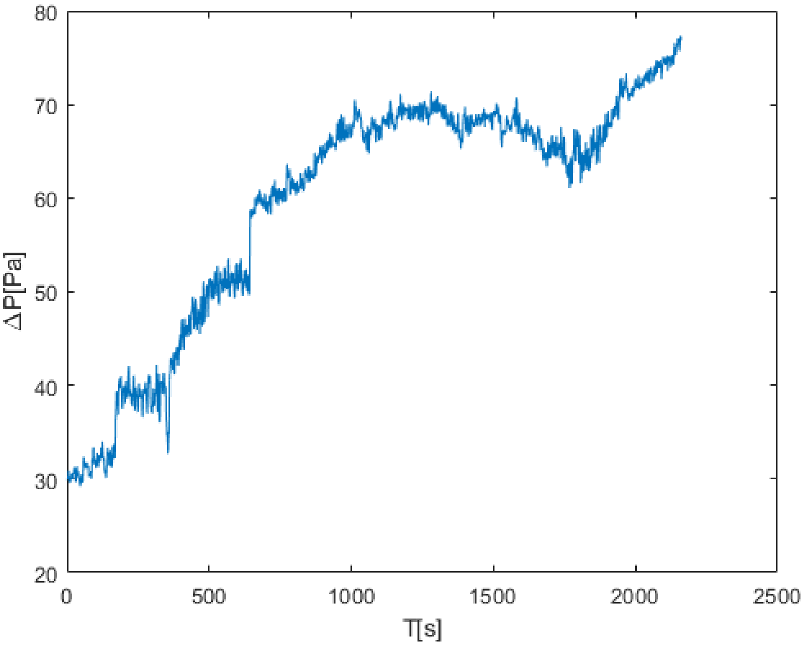

Figure 3.10: *A pressure drop graph from the polyamid* $Re_{U_b} = 25k$ *case.*

3.3 Experiments performed

Three different kinds of pipe flows experiments have been investigated; one single phase gas and two single phase water. The same test rig have been used for all experiments and what separates them are the fluid, the tracers and the Reynolds numbers. The parameters in the tables are: The Reynolds number Re_{U_b} which is calculated based on the bulk velocity U_b, the friction velocity u^*, Δt is the time separation between subsequent laser pulses, $d_{p,max}[px]$ is the maximum longitudinal particle displacement, d_p is the particle size measured in pixels and $\overline{d_{im}}$ is the average image particle size.

3.3.1 Single phase gas

The gas case had a bulk velocity of $U_b = 7m/s$, giving a Reynolds number of $Re_{U_b} = 44000$. The tracers where small water particles with an approximated diameter of $d_p = 1 - 6\mu m$ or $d_p = 0.03 - 0.2px$, provided by the high pressure atomizing nozzle as explained in the Set-up section3.1. The particle image diameter d_{im} were found to be $d_{im} = 1.3 - 1.5pixels$. The field of view were $[15cm \times 10.5cm]$

3.3.2 Single phase water: Polyester particles

Three cases with different bulk velocity U_b and thus different Reynolds number have been investigated and are shown in table 3.1. The tracers where commercial polyamide particles from Dantec Dynamics.

Polyester							
Re_{U_b}	$U_b[\frac{m}{s}]$	$u^*[\frac{m}{s}]$	$d_{p,max}[px]$	$d_p[\mu m]$	$\overline{d_p[px]}$	$d_{im}[px]$	$\Delta t[\mu s]$
17k	0.175	0.011	7	30-70	0.75-1.75	2.5	1200
25k	0.25	0.014	7	30-70	0.75-1.75	2.5	860
35k	0.35	0.019	8	30-70	0.75-1.75	2.5	650

Table 3.1: *Some key parameters of the polyamid case*

The field of view where $[16.5cm \times 11cm]$. The amount of tracer particles per image were around 25000 for all cases.

3.3.3 Single phase water: Flaeshe particles

Three cases with different bulk velocity U_b and thus different Reynolds number have been investigated and are shown in table 3.2 . The tracers where extracted from an commercial acrylic paint.

Flaeshe							
Re_{U_b}	$U_b[\frac{m}{s}]$	$u^*[\frac{m}{s}]$	$d_{p,max}[px]$	$d_p[\mu m]$	$d_p[px]$	$\overline{d_{im}[px]}$	$\Delta t[\mu s]$
15k	0.14	0.011	6	2-10	0.06-0.3	2	900
23k	0.23	0.014	10	2-10	0.06-0.3	2	900
35k	0.34	0.019	12	2-10	0.06-0.3	2	720

Table 3.2: *Some key parameters of the Flaeshe case*

The field of view was $[12.5cm \times 7.5cm]$ and the total amount of tracer particles were around 22000 per image for all cases.

Note that the field of view in this experiment does not cover the whole pipe. This is because Flaeshe particles did not emit strong enough light to be detected in the camera images therefore the camera were placed closer to the PIV section. Also note that the reported friction velocities u^* are used from the polyamid case. On the positive side, the PIV frames in the Flashe case were not as contaminated with reflections as the polyamide case. This can be seen in section 3.2.3 by comparing figure 3.8b and 3.9b which shows a image from the polyamide and flashe case respectively. The polyamide frame 3.8b have a strong reflection in the lower right corner. This reflection cannot be seen in the Flashe frame, see figure 3.8b.

3.4 Post processing

After the experiments are finished we are left with a sequence of 500 image pairs where a convergence of the longitudinal mean velocity $\overline{U}$ is established after around 200-250 image pairs, see figure 3.11. These images contains the information of the fluid that we want to investigate and we need to process them appropriately to make the interpretation as easy and reliable as possible. Beneath are an explanation of the different steps that were performed on every case. Each image sequence were treated and evaluated the same way and the processing techniques were performed in the order as they are explained.

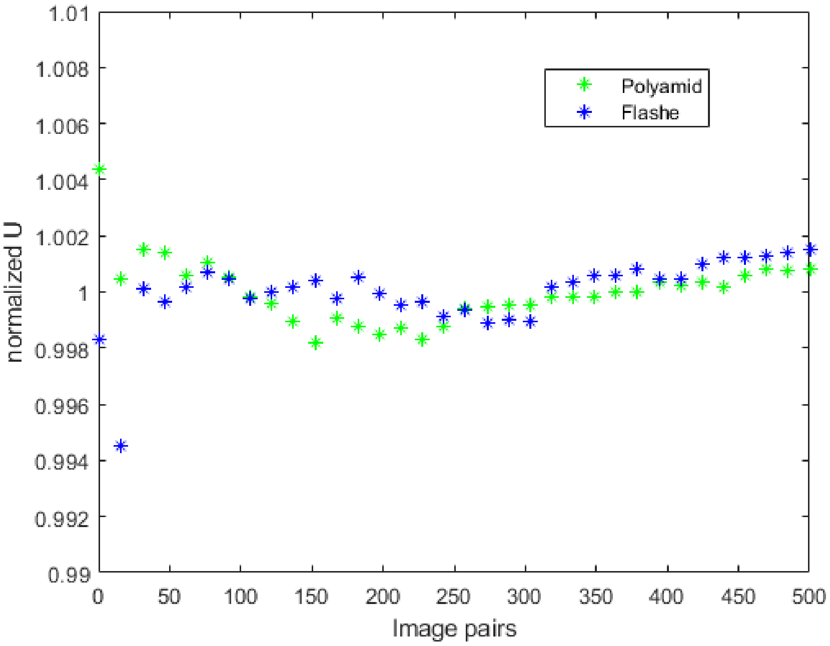

Figure 3.11: *A convergence plot of the normalized longitudinal mean velocity* $\overline{U}$ *from the polyamid* $Re_{U_b} = 35k$ *case with* $I_W : [128 \quad 40]$ *for both particles.*

3.4.1 Background subtraction

A background subtraction algorithm were build and used in an effort to reduce effects of the background gradient and to mitigate reflections on the images. The background image are created by first reading in the dimensions of the original images to make a dimensionally identical empty 2D array. The 2D array is then converted to an unsigned 16 bit integer matrix by using the $im2uint16()$ function and after adding the maximum value 2^{16} to each position a preliminary background image created. The values of each pixel in the original greyscale images are between 1 to 65655.

Next, a loop goes through the whole sequence of images and for every iteration each image from the original sequence is imported by using the function *imread*(), one by one. During every iteration all pixel positions in the original image is compared with the corresponding position in the background image. For corresponding positions where the original image have the lowest value, the value in the background position is substituted to the lowest value, but else, no change will be done. This proceeds until the whole sequence of original images have been looped trough and then by subtracting 1 from the result, we have the final background image. The subtraction from the background image is done to make sure that any original image is not masked i.e. ending up with a position value of zero, in case of a maximum value in the background image. Next a subtraction of the background from each and every original image is performed and the resulting images are saved and used for further processing.

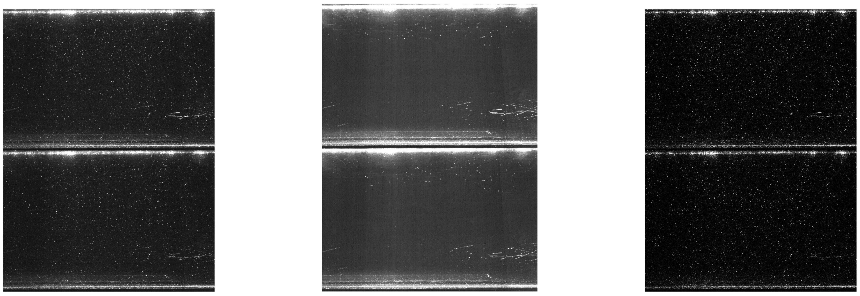

Figure 3.12: *Showcase of the subtraction process in the polyamide case. From the left to right: Original, background and filtered*

3.4.2 PIV algorithm

HydrolabPIV

The next step in the post processing is to perform the PIV on the images to quantify the fluid motion. All cases have been processed in the program HydrolabPIV, developed by Dr.Kolaas at the University of Oslo, see Kolaas (2017)[28]. As mentioned previously, HydrolabPIV uses a normalized cross correlation function to measure the displacement of the fluid motion and a fast Fourier transform is used for a faster calculation. To improve the accuracy of the cross correlation peak, a sub-pixel interpolation is employed in HydrolabPIV. The user can freely choose between several options of interpolation techniques but in this work the *Lanczos* kernel have been used, as it is recommended for particles within the particle image size $d = 2 - 4$ pixels.

Implementation of HydrolabPIV

The implementation of HydrolabPIV requires the user to build a $Matlab$ script. This script can be viewed in it's entirety in the Appendix 6.2.
At first a masking are done manually where the outer edges outside of the pipe, are masked away. The masking handle put the intensity value in the masked

area of the image to zero, which means that all the information in that area is deleted. A unique mask are used for all image pairs for each individual case, since the camera target is identical for all images during every experiment run.

By now, the images are ready to get examined by the cross correlation function. First we need to define the search range and subwindow size. This is done in the function $setpivot('range', [X \quad Y \quad X \quad Y],' subwindow'[X \quad Y], .50)$ where the arguments following *range* determines the search area, the argument following *subwindow* determine the size of the subwindow and the last argument is the overlap which is always set to 50% in this work. For an overlap of 50% we will get a velocity vector for every $\frac{X}{2} pixels$ in the X direction and $\frac{Y}{2} pixels$ in the Y direction. The argument for *subwindow* and *range* will vary but the subwindows lies in between the range 32×32 to 128×128 and the range is always put to be half the subwindow size in respective direction. This information is then used in the $normalpass()$ function in which the cross correlation function are used to evaluate the fluid motion. The *normalpass* function takes in the arguments $normalpass(mask, im1, mask, im2, opt)$ where the *mask* is the masking information, $im1$ and $im2$ are a subsequent image pair and *opt* is the information from the *setpivopt* function. The normal pass returns a *struct* called *piv* with information of the velocity field among others. After the $normalpass()$ a vector validation to detect and replace outliers of the velocity field is performed to improve the quality of the PIV result. HydrolabPIV implements the same method as Westerweel and Scarano(2005)[12], namely a 3×3 normalized local median filter. For cases where part of the3×3 filter is masked, a masked 5×5 local median filter is used instead. Residuals from the filter are replaced by using a function called $replaceoutliers()$ where the missing vectors are evaluated using a fitted B-spline.
This process is performed for each image pair, i.e 500 times, giving a *struct* with velocity field information for each subsequent image pair. The *struct* that are returned from the normalpass contains among others the following: 2D Velocity field of the longitudinal component U and the radial component V with corresponding coordinates in x- and y- direction, details about the PIV pass and the kind of interpolation function for the cross correlation peak and other details that have been used in the pass, peak strength and signal to noise ratio strength, position of outlier vectors and more.

3.4.3 Calculation of the turbulence profiles

Another script is build to handle the sequence of structures that where produced in the HydrolabPIV program by the normalpass function in the previous step. Through an iteration loop each velocity field component, U and V, are read in one by one and are then put together, side by side and streamwise, into two matrices U_{matrix} and V_{matrix}. Defining the streamwise coordinate to be X and the radial Y the matrix dimensions will be $Y \times 500X$ when 500 image pairs is completed. By using the fact that the flow is considered to be stationary,as mentioned in the Set-up section, we can treat every row X in the matrix as a time signal. How many points each longitudinal row contains depend of the subwindow size I_W but will in this work range between 10000 - 80000 points.

Coordinate transform

To convert from the camera pixel coordinate system to a world coordinate system a coordinate transformation needs to be implemented. In this work a cubic transformation have been used instead of a linear transformation as it is optional in HydrolabPIV. This is to take into account the pipe curvature which distort the PIV images. A reference pixel point system X is created by using the coordinate map see figure 3.5 where the physical world units are known. The user need to manually click in the reference points as can be seen in figure3.13.

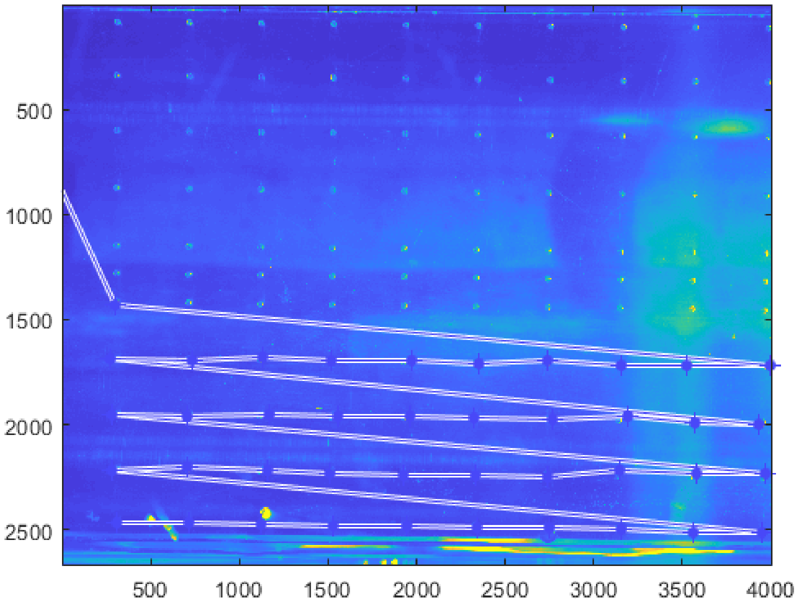

Figure 3.13: *Selecting pixel reference points.*

Then a reference world unit grid $\tilde{X}$ is defined in the $ndgrid()$ function where dimensions and grid steps in the streamwise and radial direction are established by input from the user. These should match the coordinate map.
Using both the above reference systems the coordinate transformation equation

$$\tilde{X} = TX \tag{3.3}$$

can be solved for T, which is the transformation matrix. Using the transformation T the whole field can be mapped from the pixel to real world coordinates.

Mean velocity

The mean velocity profiles of U and V as a function of the diameter of the pipe can now be calculated by using the $mean(var, dim)$ function in Matlab. It calculates the mean value of a variable var along the dimension dim. For a random variable vector U_j made up of N scalar observations, the $mean(var)$ is defined as $avg = \frac{1}{N}\sum_{j=1}^{N} U_j$. By taking $mean(U_{matrix}, 2)$ we will get a mean velocity profile U_{mean} as a function of the diameter of the pipe for the streamwise U component.

Fluctuating velocities

By using the mean velocity U_{mean} the fluctuating velocity matrix $U_{fluctuating}$ can be defined. This is simply done by a matrix subtraction, $U_{fluctuating} = U_{matrix} - U_{mean}$ where the U_{mean} is subtracted from every column. Clearly the $U_{fluctuating}$ matrix comes in the same dimensions as the U_matrix and it contains time signals of the observed fluctuations from the mean velocity U_{mean}, which we can think of as the observed turbulence fluctuations.

Turbulence profiles

A streamwise turbulence intensity profile u' are approximated by giving the $U_{fluctuating}$ matrix as the argument to the root mean square function $rms(var, dim)$ in Matlab. It calculates the rms level of a variable var along the dimension dim. For a random variable vector u_j made up of N scalar observations $rms(var)$ is defined as $u'_j = \sqrt{\frac{1}{N}\sum_{j=1}^{N} |U_{fluctuating,j}|^2}$. The return from $rms(U_{fluctuating}, 2)$ is the turbulence intensity in the streamwise direction as a function of the diameter of the pipe.

Corresponding calculations is performed in order to calculate the turbulence profile v'.

And the Reynoldstress component $u'v'$ can at last be calculated by using the Matlab function $mean()$ to gain, $u'v' = mean(U_{fluctuating}. * V_{fluctuating}, 2)$. The product $U_{fluctuating}. * V_{fluctuating}$ is a component wise multiplication.

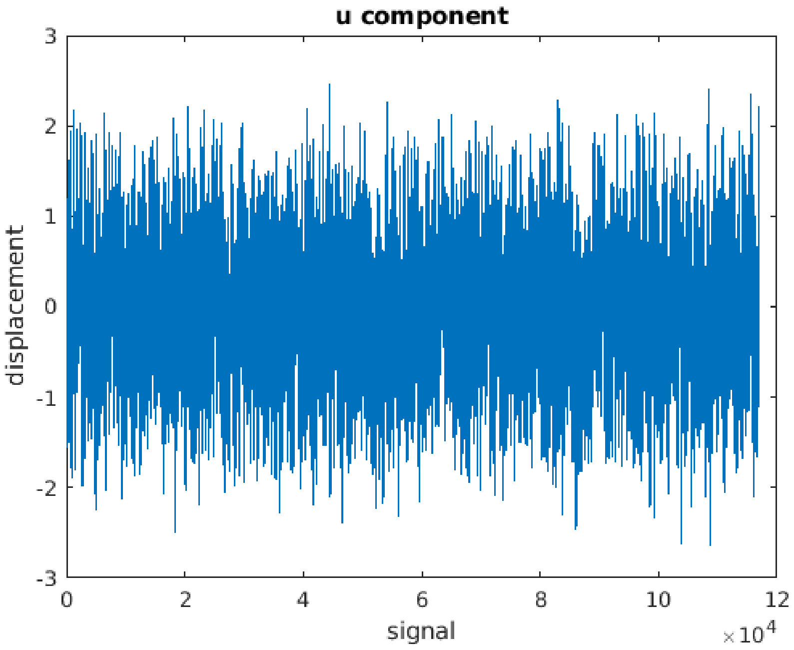

Figure 3.14: *A row vector from the* $U_{fluctuating}$ *matrix in the gas phase, representing the fluctuations in the streamvise direction in the fluid.*

Spectral analysis

The PIV experiments in general suffer from a low temporal resolution and in this experiment the acquisition rate were only $0.3Hz$. On the other hand, a quite small field of view and the relatively large camera sensor result in a high spatial resolution. A spectral analysis in time can be done by applying Taylor's hypothesis(1938)[1] of frozen turbulence through multiplying the spatial frequencies with the mean velocity, see Scharnowski et al.(2018)[5]. The power density spectra was computed by using the resulting 500 vector fields of the fluctuating longitudinal and radial component u and v respectively extracted from the $U_{fluctuating}$ and $V_{fluctuating}$ matrices as in figure 3.14. The spectra is produced with the Welch method, from Welch (1967)[55], where each signal is divided into segments of 1000 with a 50% overlap using Hamming windows. See more information about the post processing in the Appendix 6.2.

---

[1] From Moin(2009)[56]"Taylor (1938) proposed his famous hypothesis relating the spatial and temporal characteristics of turbulence. Taylor reasoned that if the turbulence intensity u is small compared to the mean flow speed U, then the temporal response at a fixed point in space can be viewed as the result of an unchanging spatial pattern convecting uniformly past the point at velocity U."

Chapter 4

Results and discussion

4.1 Validation of gas phase

In order to establish some confidence in the set up and post processing process, a comparison of the gas phase PIV measurements have been made by a direct numerical simulation(DNS) conducted by Wu and Moin(2008)[7]. An explanation of the approach of the DNS and the experiment are presented below.

DNS

Wu and Moin made a simulation of a fully developed incompressible turbulent flow through a smooth pipe with unit radius R = 1, at bulk velocity- and pipe diameter-based Reynolds number at $Re_D = 44000$ on a second order finit-difference methods on 630 million grid points. The grid distribution where $300 \times 1024 \times 2024$ along the cylindrical dimensions r, θ and z respectively where r is the radial component measured from the pipe axis, θ is the azimuthal component and z is the flow axial component. The minimum and maximum wall normal grid spacings are 3.578×10^{-4} and 9.892×10^{-3}, respectively, which correspond to 0.41 and 11.3 in wall units. The grid spacing distribution can be seen in figure 4.1. The first layer of grid points is located at 0.205 wall units away from the pipe surface.

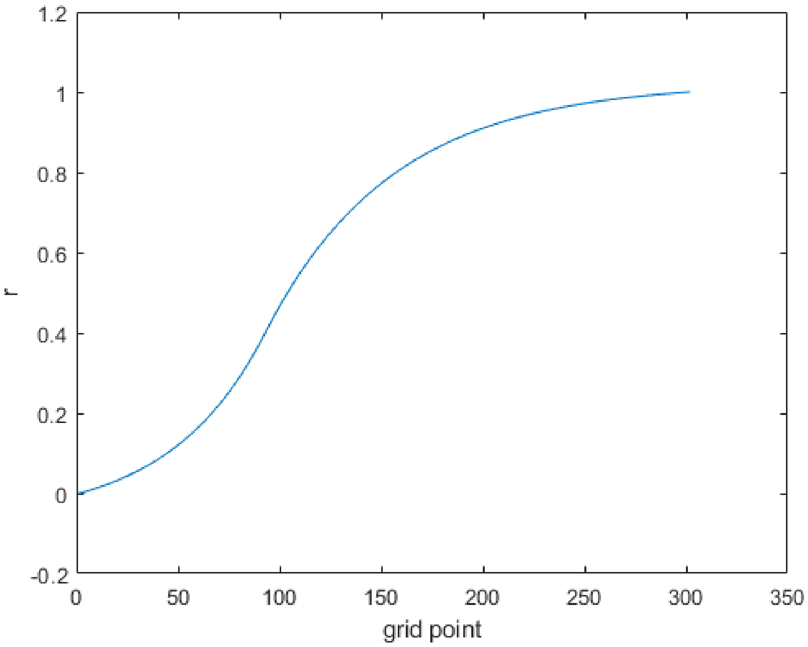

Figure 4.1: *The wall-normal grid point distribution of the simulation by Wu and Moin. At the vicinity of the wall, between* $0.9 < r < 1$ *the grid distribution is at it's finest with 108 points. Between* $0 < r < 0.1$*, at the centerline of the pipe, there are 44 grid points.*

The statistics where collected for $30000\Delta t$ with $\Delta t = 0.005$. To accommodate unrealistic initial conditions and start-up effects the collection where started after $20400\Delta t$ which is enough for one particle to travel 10 times the pipe axial dimension at the bulk velocity.

PIV

A fully developed gas single phase flow experiment were conducted at an average Reynolds number of $Re_D = 44000$, based on the bulk velocity. A total of 500 instant velocity fields were collected and processed to produce the data and velocity and turbulence profiles. Only the upper half of the pipe are displayed due to the quality of the raw images and resulting accuracy of the profiles. Three different I_W were used in the post processing to be compared where the common factors where an overlap of 50%, a particle imag size $d_p = 1.5px$, a time step of $\Delta t = 50\mu s$, a pipe diameter D = 0.1m or in wall units $\delta^+ = Re_\tau = 1200$, a CCD array of [4008px 2672px] with a field of view $[S_x \quad Sy] = [13cm \quad 10cm]$ and a ratio of the range of the large turbulent structures and the smallest coherent structures, $W_{str} = \frac{3\delta^+}{20^+} = 180$. In table 4.1 are some other relevant key parameters of the experiment as well.

I_W	$[32px \quad 32px]$	$[64px \quad 64px]$	$[128px \quad 128px]$
$Range_{I_W}$	$[16px \quad 16px]$	$[32px \quad 32px]$	$[64px \quad 64px]$
$[N_x, N_y]$	[250 167]	[125 83]	[68 41]
N_p/I_W	7	30	110
$d_{x,max}$	11.7px	11.7px	11.7px
SDR_{th}	[63 40]	[31 20]	[16 10]
y^+	128^+	255^+	300^+
$\frac{du}{dy}_{I_{W,\Delta t}}$	$0.19px$	$0.21px$	$0.3px$

Table 4.1: *Some key parameters from the Gas phase experiment. They are in order: the interrogation window size I_W, Search range $Range_{I_W}$, number of vectors in x- and y direction $[N_x, N_y]$ per velocity field, particles per interrogation window N_p/I_W, maximum particle displacement $d_{x,max}$, spatial dynamic range in the image space SDR_{th}, field of view ,an approximation of the first mesh points in wall units y^+, maximum difference in particle displacement over the I_W measured from the first mesh point y^+.*

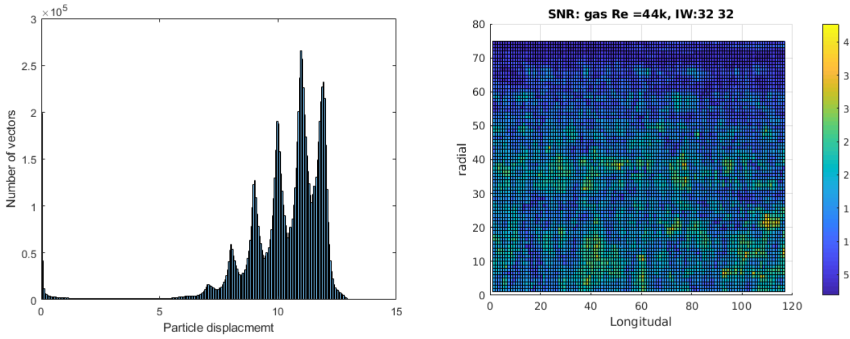

(a) (b)

Figure 4.2: *On the left: A histogram of the stream wise velocity component U. The horizontal axis shows the particle displacement and the vertical axis shows the number of velocity vectors. An accumulation of velocity vectors around whole integers indicates that there are peak locking effects. On the right: Signal to noise ratio for the case with interrogation window size [32px 32px]. Upper half of the pipe are shown. A relatively low signal to noise ratio is observed in the vicinity of the pipe wall compared to the center.*

4.1.1 Mean and rms-profiles

The measurements are presented in terms of normalized mean horizontal velocity profile $\bar{U}/U_b$, streamwise and radial rms-profiles, $u^{'}/U^*$ and $v^{'}/U^*$ and the Reynolds stress profile $u^{'}v^{'}/u^{*2}$. The bulk velocity is calculated from the measured mass flow rate $\dot{m}$, defined as

$$U_b = \frac{\dot{m}}{\rho A} \tag{4.1}$$

where ρ and A is the density and area respectively. The friction velocity u^* is calculated from the measured pressure drop and are defined as

$$u^* = \sqrt{\frac{\tau_w}{\rho}}, \quad \tau_w = \frac{\Delta P D}{4L} \tag{4.2}$$

where L is the distance between the measured pressure and D is the diameter of the pipe.

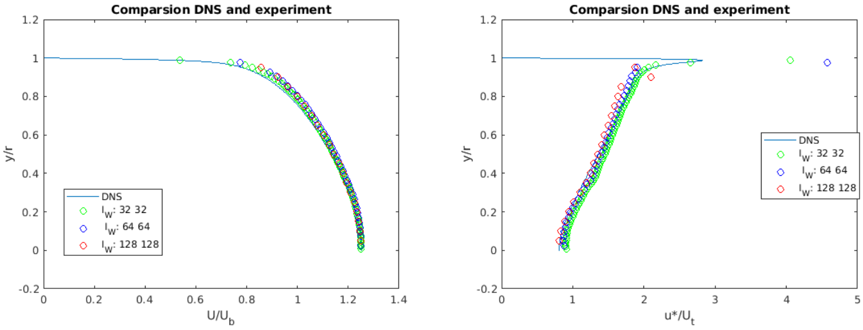

(a) (b)

Figure 4.3: *Normalized $\bar{U}$ and u' on the left and right respectively. Compared with DNS data from Wu and Moin(2008)[7]*

The average velocity $\bar{U}$ left in figure 4.33 fits very well with the DNS simulation for all the interrogation window sizes. The discrepancies are rather small in general and just differs a little bit from about 0.8 and upwards towards 1, at the pipe wall, which should be excepted considering a strong gradient and quite uneven illumination, see figure 2.6. Peak locking effects, see figure **??**, will also affect the accuracy more when the particle displacement is lower as is the case closer to the wall. The rms-profile for the u' component, figure 4.3b, is rather good for all of the interrogation windows, as well. A larger deviation at the spike in the vicinity of the wall can be observed for all cases except the [128 128], since it actually is to big to capture the kinematics that close to the wall. Here the experimental peaks exceed the DNS peaks by roughly 20%. There might be several explanations for this. For example, the maximum displacement of the u' profile is $2px$ and the approximated measurement error computed from the method to compute the non-uniform displacements, presented by [37], is 0.18px which may lead to a broaden cross correlation peak, see Adrian and Keane(1992)[6], and thus a lower accuracy. There is also the problem with an uneven light distribution as mentioned earlier and also reflections which may contribute to a larger signal to noise ratio here. By looking at figure 4.2b a relatively low Signal to noise ratio can be seen overall but especially close to the pipe wall. Another factor regarding the error of the u' peak value, might be the peak locking effect, as it's tendency to bias the cross correlation peak towards integers, can over- or underestimate the particle displacement which can result in large biases when the particle displacement is small.

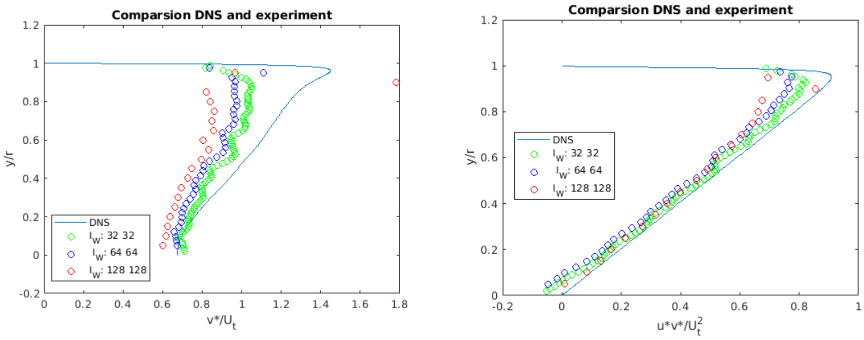

(a) (b)

Figure 4.4: *Normalized v' and $u'v'$ on the left and right respectively. Compared with DNS data from Wu and Moin(2008)[7]*

.

The rms-profiles for the v' component in figure 4.4a are all form wise somewhat accurate but underpredict the values compared with the DNS profile by Wu and Moin with around 30%. This can be due to a low spatial dynamic range(SDR) as it seems that the lower the SDR the lower the prediction of the profile. Looking at figure4.5b, a large peak can be seen around zero particle displacement and is most probably a bias effect, which certainly will contribute a large bit to the underestimation of the profile.

In conclusion it seems that regardless the peak lock effect, a quite low SDR and a low SNR there are satisfying accuracy in the PIV experiment which confirms that the current experimental set-up well serves it's purpose.

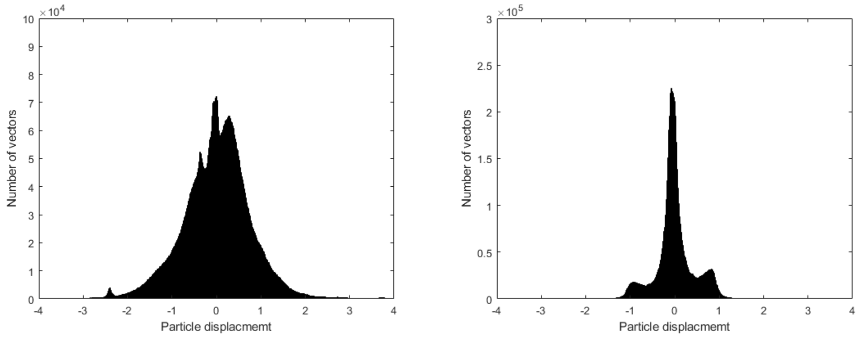

(a) (b)

Figure 4.5: *Histogram of the particle displacement for the radial u- and v -component. The v-component shows a heavy bias towards zero whereas the u-component have a more Gaussian distribution.*

.

4.1.2 Kolmogorov spectra

The power density spectres have been compared with the Kolmogorov spectre for both the longitudal u' and radial v' component, at three different pipe positions, the first mesh point $y^+ = 128$, $y^+ = 255$, $y^+ = 300$ respectively , $y/R = 0.5$ and $y/R = 0$ and for all three interrogation window sizes $[32px \quad 32px]$, $[64px \quad 64px]$ and $[128px \quad 128px]$. The frequency band spans up to the Kolmogorov length scale η multiplied with the mean velocity $\bar{U}$. It is important to notice that the power density spectre for frequencies higher than the mean velocity divided by $2I_W$ is within the noise floor and no frequency larger than $f = \frac{U}{I_W}$ can be resolved due to the size of the interrogation window, see Scharnowski(2018)[5].The resolved frequency and wave length are presented in table 4.2.

I_W	$[32px \quad 32px]$	$[64px \quad 64px]$	$[128px \quad 128px]$
$f[Hz] = \frac{U}{2I_W}$	3000	1500	750
$k[1/m]$	2.4mm	4.8mm	9.6mm

Table 4.2: *$f[Hz]$ corresponds to the highest theoretical resolved frequency outside the noise floor and k the corresponding wave number in mm.*

u' component

The common trait for the u' spectres in all positions is that the green specter of interrogation window size $[32px \quad 32px]$ seem to align with the $-5/3$ decay for the longest stretch followed by the blue spectre of the size $[64px \quad 64px]$ and that stretch coincides around $f = 10^3 Hz$ which corresponds to eddies of $175px$ size which according to [37] should be within the range of resolvable frequencies for both [32 32] and [64 64]. This interrogation window observation make sense considering that the turbulence profiles above showed the same pattern and one would assume that this would reflect the accuracy on the spectres, as well. The power of the spectres also aligns with the rms-profiles above in that it is highest in the vicinity of the wall and decreases as a function of the radius towards the center-line of the pipe. The spectre from the mid-pipe position $y/R = 0$ in figure 4.7b proved to have the longest alignment with the Kolmogorov decay $-5/3$ followed by the quarter pipe position $y/R = 0.75$ which again indicates that there are less noise in the region closest to the pipe center as it also aligns well with the previous results in the rms-profiles.

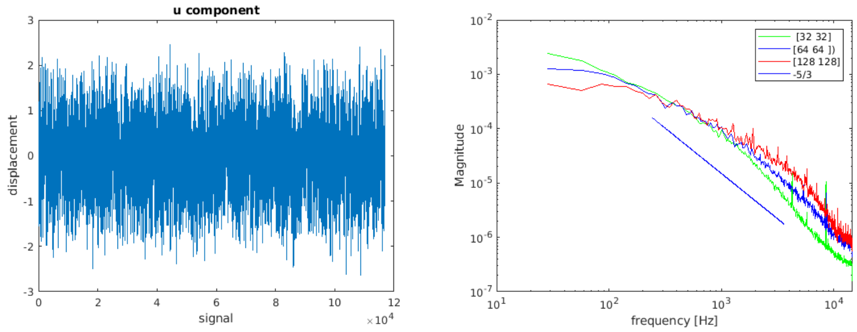

(a) (b)

Figure 4.6: *On the left: An example of a signal used to compute the power density spectrum of the u' component. This signal shows the u component signal from the vicinity of the pipe wall, here plotted as a function of the longitudinal axis of the 500 velocity fields. On the right: The Kolmogorov spectra in blue compared with the longitudinal PIV spectra of the different interrogation windows, calculated from the u' signal at the first mesh points.*

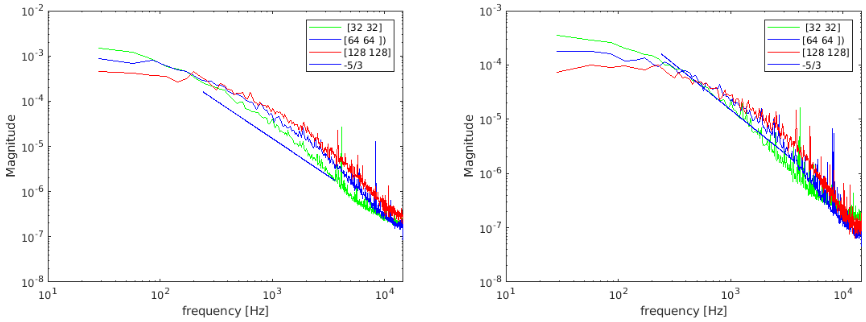

(a) (b)

Figure 4.7: *On the left: The Kolmogorov spectra in blue compared with longitudinal PIV spectra of the u' component calculated from the quarter pipe position. On the right: The Kolmogorov spectra in blue compared with the longitudinal PIV spectra of the u' component calculated from the mid pipe position.*

v' component

The spectres of the v' component from the first mesh point in figure 4.8b all seem to be characterized by a strong noise where only a very small section of the spectra on a very high frequency seem to align well with the $-5/3$ decay. The [32 32] spectres in both figure 4.9a and 4.9b seem to align for a longer stretch with the $-5/3$decay around the frequency $f = 10^3 Hz$

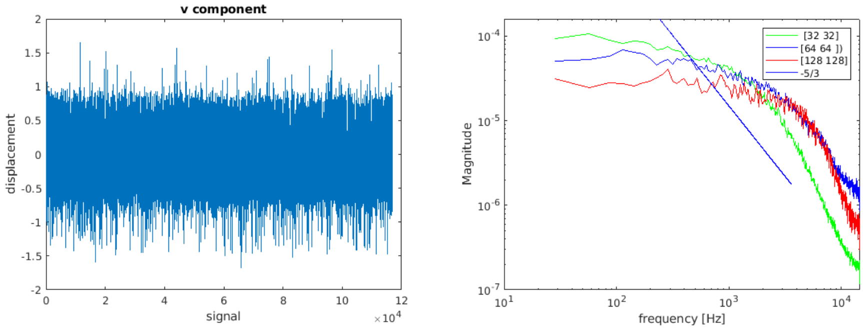

(a) (b)

Figure 4.8: *On the left: An example of a signal used to compute the power density spectrum of the v' component. This signal shows the u component signal from the vicinity of the pipe wall, here plotted as a function of the longitudinal axis of the 500 velocity fields. On the right: The Kolmogorov spectra in blue compared with the longitudinal PIV spectra of the different interrogation windows, calculated from the v' signal at the first mesh points.*

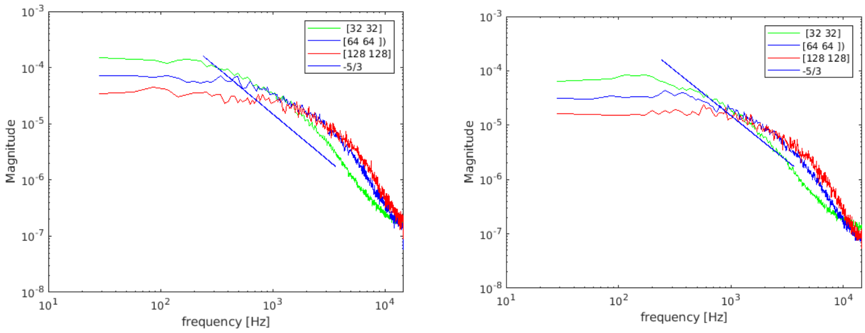

(a) (b)

Figure 4.9: *On the left: The Kolmogorov spectra in blue compared with longitudinal PIV spectra of the v' component calculated from the quarter pipe position. On the right: The Kolmogorov spectra in blue compared with the longitudinal PIV spectra of the v' component calculated from the mid pipe position.*

4.2 Results

The result of the comparison of the two different particles are here shown together with the DNS results from Wu and Moin(2008)[7] as well as with the Kolmogorov spectras for the three different Reynolds numbers. Each corresponding Reynolds number pair is presented separately. Two different interrogations windows have been used, [$72px$ $72px$] and [128 $40px$] both with the recommended particle value per window of around 10 particles [33] and also since the gas phase validation showed that the window with this amount of particles performed best results, see section 4.1. Better results can be seen in general for the [128   40] for all turbulence profiles, especially in the pipe vicinity as it mitigates the affects of the non uniform particle displacements, see sub-section 2.2.4. Important to keep in mind is as mentioned in section 3.2.4 that the pressure drop can't be relied upon and thus neither the important friction velocity u^* which is used for the normalization of the turbulence profiles. The precision of the turbulence profiles are thus not entirely reliable considering their proximity towards the DNS profiles. Regardless, since the main focus is to compare two tracer particles regarding their ability to reflect the turbulence within a fluid, there are hopefully still some objective insights that can be made between them two.

Even though the polyamid particles are within the range of the recommended image particle size of $2.2px$, see [33], these experiment still seem to be affected by peak lock effects, see figure 2.8a. Same goes for the Flashe particles where the peak lock effect seem to be even larger, see figure 2.8b, probably due to an even smaller particle image size of about $2px$, slightly under the recommended value. Neither the u- nor v-component in the polyamid cases seem to be affected by any peak lock effect, see figure figure 2.9. But the Flashe cases in figure 2.10 show some peak lock effect in the v- component. The fluctuating distributions are almost identical for the different cases for each particle so only the $Re_{U_b} = 35k$ case are shown here. This can be an important reason for the much larger deviations with the DNS results that can be seen in the rms-v profiles compared to the rms-u profiles for all experiments. The two particles both captures the kinematics excellent regarding the mean velocity and quite well for the rms-u profiles and do not differ in any surprising way in this regard, except for the rms-profiles in figure 4.11. The SNR fields in figure 2.11 shows values over 20 which gives us confidence that the vectors obtained by the cross correlation are valid for both particles, as Scharnowski and Kähler(2016)[4] showed that a SNR value of about 3 and over is sufficient to obtain valid velocity vectors. Something that do differentiate between the particles can be seen in the turbulence profiles for the rms-v profiles. The profiles from the polyamid particle have smoother profiles than the Flashe particle which have a lot of fluctuations from the pipe-vicintiy down to about $y/R = 0.4$ for all Reynolds numbers which is probably due to peak locking effects, see figures 4.12, 4.16 and 4.20.

One other thing is that even though the Flashe cases (without a measured pressure drop) comes with lower bulk velocities U_b across the board compared with the Polyamid cases, still shows larger turbulence intensities, especially for the rms-v profiles. Since the same normalization factor u^* have been used for the two, one would think that the case with a higher bulk velocity and thus a larger friction velocity u^*, would then show a relatively stronger intensity. Perhaps this is an effect of the different field of view between the two experiments, where the Flashe cases have a smaller field of view, or maybe even that the much smaller Flashe particles (an estimated $2 - 10\mu m$ vs the polyamid of $30 - 70\mu m$) follows the turbulence fluctuations in a more precise way. Another explanation might be the particle displacement, which is almost the double for the Flashe experiments compared to the Polyamid cases except for only the first case with $Re_{U_b} = 15k$, see table 3.2 and 3.1, allows for a larger displacement of the v-components. This displacement discrepancy seem to correspond well with the results in that when the particle displacement is larger, the rms- v profile is larger as well, see case $Re_{U_b} = 23 - 25$ and $Re_{U_b} = 35k$, but are closer when the particle displacement is more similar, see case $Re_{U_b} = 15 - 17k$. Thus, this problem is probably not a question about the quality of the particles but rather the quality of the pre-experimental preparations when deciding the time step between the laser pulses.

Coming to the power density spectres, all cases and all particles turned out to align well with the Kolmogorov spectra $-5/3$ and especially in comparison to the gas phase. This should be an indicator that both particles and the PIV set-up are able to pick up the turbulent fluctuations within the integral length scale adequately. The spectres calculated from the [72 72] windows were in general less noisy compared to the spectres from the [128 40] windows. No qualitative distinction can be seen between the different particles. The energy within the spectras can be seen growing in with the Reynolds number which is also a good indicator.

4.3 Mean and rms-profiles

The measurements for the mean- and rms-profiles are presented in terms of normalized horizontal velocity profiles $\overline{U}/U_b$, streamwise and radial rms- profiles, u'/u^* and v'/u^* and the Reynolds stress profile $u'v'/{u^*}^2$. Key parameters to the experimental results presented in tables in the beginning of each sub section. They are: Interrogation window I_W, the Reynolds number Re_τ based on the friction velocity, number of vectors for a single field in $[N_x \quad N_y]$, particles per sub window N_p/I_W, the range of the coherent structures W_{str}, the Spatial dynamic range SDR_{th} and the non-uniform displacement based on the window size $\frac{du}{dy}_{\Delta t}$.

4.3.1 Re = 15-17k

$Re_{U_b} = 15k$

I_W	Re_τ	$[N_x, N_y]$	N_p/I_W	W_{str}	SDR_{th}	$\frac{du}{dy}_{\Delta t}$
[72 72]	550	[111 74]	11	82	[55 37]	$0.27px$
[128 40]	550	[62 133]	11	82	[31 66]	$0.15px$

Table 4.3: *Some key parameters from the water experiment with Flashe particles with* $Re_{U_b} = 15000$.

$Re_{U_b} = 17k$

I_W	Re_τ	$[N_x, N_y]$	N_p/I_W	W_{str}	SDR_{th}	$\frac{du}{dy}_{\Delta t}$
[72 72]	550	[111 74]	11	82	[55 37]	0.48
[128 40]	550	[62 133]	11	82	[31 66]	0.27

Table 4.4: *Some key parameters from the water experiment with Polyamide particles with* $Re_b = 17000$.

Turbulence profiles

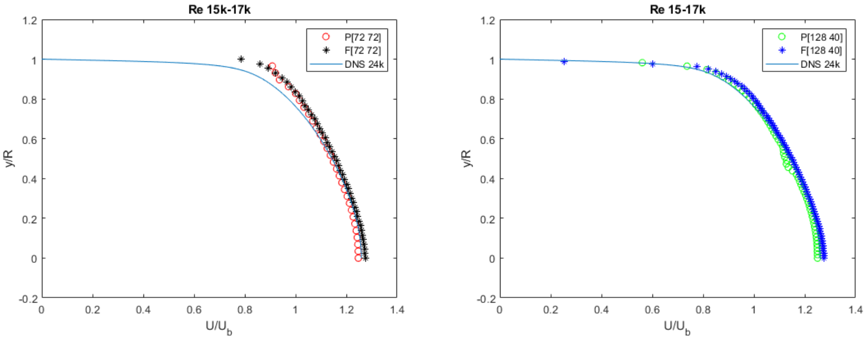

(a) $I_W[72 \quad 72]$ (b) $I_W[128 \quad 40]$

Figure 4.10: *Normalized* $\bar{U}$ *for Flashe (F) and Polyamid (P) particles on both the left and right compared with DNS data from Wu and Moin(2008)[7].*

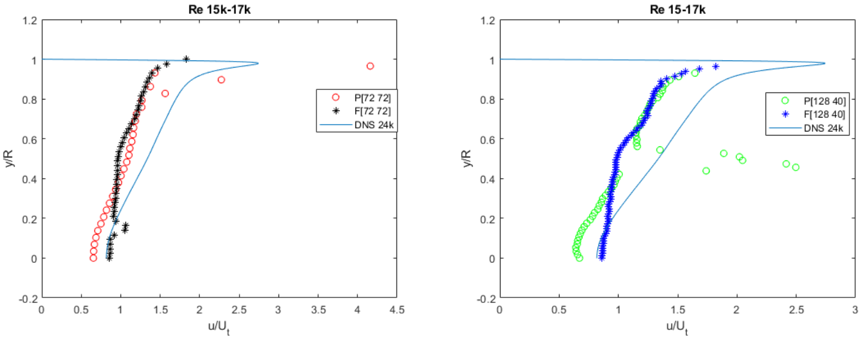

(a) $I_W[72 \quad 72]$ (b) $I_W[128 \quad 40]$

Figure 4.11: *Normalized* u' *for Flashe (F) and Polyamid (P) particles on both the left and right, compared with DNS data from Wu and Moin(2008)[7]*

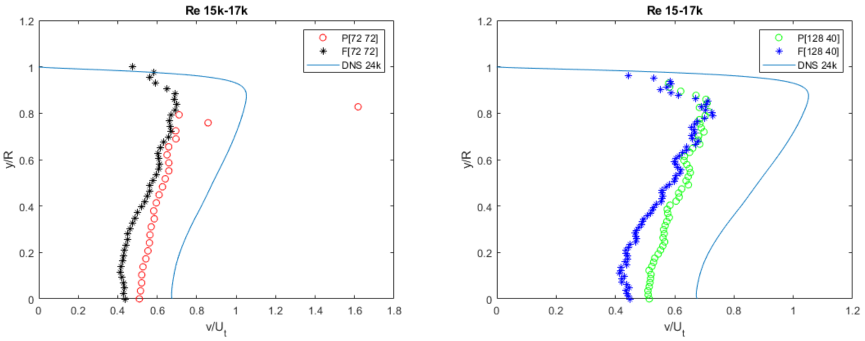

(a) $I_W[72 \quad 72]$ (b) $I_W[128 \quad 40]$

Figure 4.12: *Normalized v' for Flashe (F) and Polyamid (P) particles on both the left and right, compared with DNS data from Wu and Moin(2008)[7]*

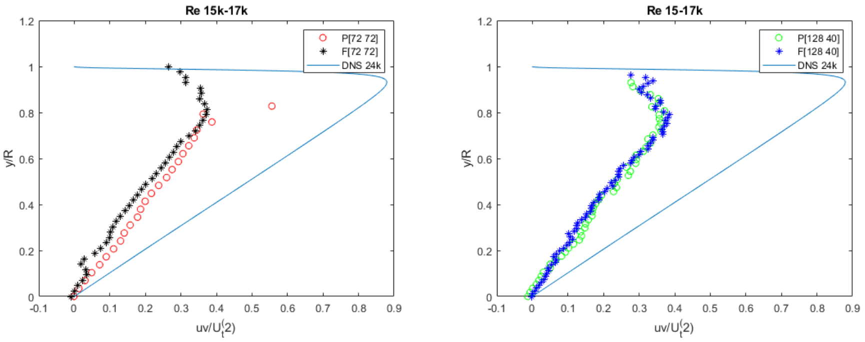

(a) $I_W[72 \quad 72]$ (b) $I_W[128 \quad 40]$

Figure 4.13: *Normalized Reynoldstress $u'v'$ for Flashe (F) and Polyamid (P) particles on both the left and right, compared with DNS data from Wu and Moin(2008)[7]*

4.3.2 Re= 23-25k

$Re_{U_b} = 23k$

I_W	Re_τ	$[N_x, N_y]$	N_p/I_W	W_{str}	SDR_{th}	$\frac{du}{dy}_{\Delta t}$
[72 72]	700	[111 74]	11	105	[55 37]	0.33
[128 40]	700	[62 133]	11	105	[31 66]	0.18

Table 4.5: *Some key parameters from the water experiment with Flashe particles with $Re_{U_b} = 23000$.*

$Re_{U_b} = 25k$

I_W	Re_τ	$[N_x, N_y]$	N_p/I_W	W_{str}	SDR_{th}	$\frac{du}{dy}_{\Delta t}$
[72 72]	700	[111 74]	11	105	[55 37]	0.44
[128 40]	700	[62 133]	11	105	[31 66]	0.24

Table 4.6: *Some key parameters from the water experiment with Polyamid particles with* $Re_{U_b} = 25000$.

Turbulence profiles

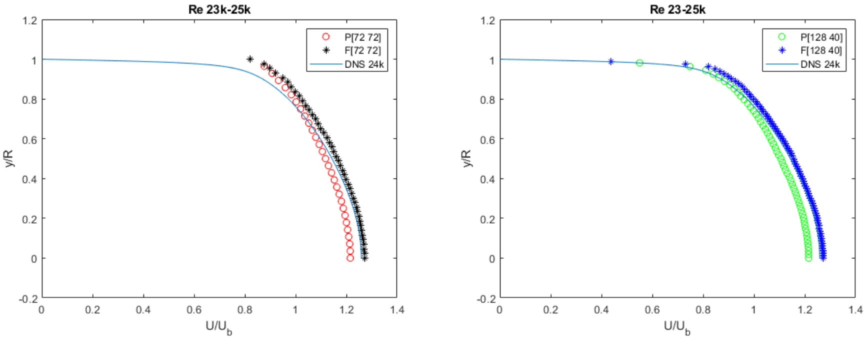

(a) I_W[72 72] (b) I_W[128 40]

Figure 4.14: *Normalized* $\bar{U}$ *for Flashe (F) and Polyamid (P) particles on both the left and right compared with DNS data from Wu and Moin(2008)[7].*

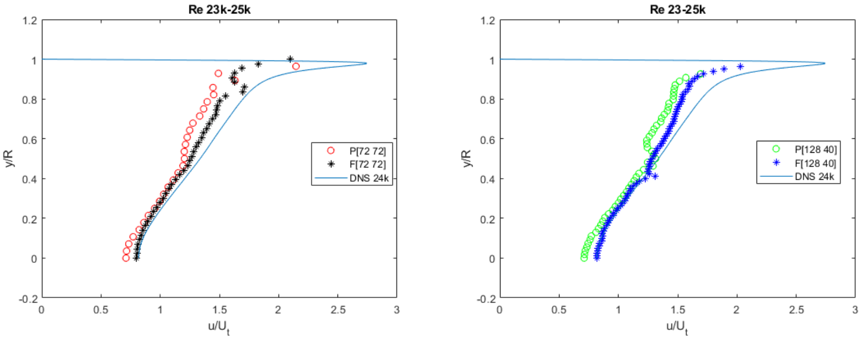

(a) I_W[72 72] (b) I_W[128 40]

Figure 4.15: *Normalized* u' *for Flashe (F) and Polyamid (P) particles on both the left and right, compared with DNS data from Wu and Moin(2008)[7]*

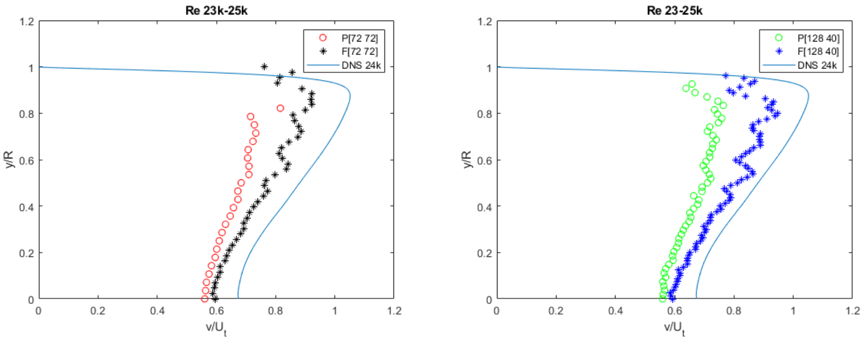

(a) $I_W[72 \quad 72]$ (b) $I_W[128 \quad 40]$

Figure 4.16: *Normalized v' for Flashe (F) and Polyamid (P) particles on both the left and right, compared with DNS data from Wu and Moin(2008)[7]*

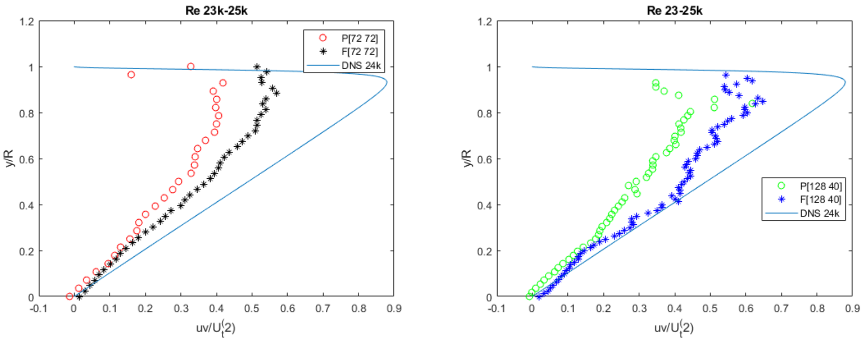

(a) (b) $I_W[128 \quad 40]$

Figure 4.17: *Normalized $u'v'$ for Flashe (F) and Polyamid (P) particles on both the left and right, compared with DNS data from Wu and Moin(2008)[7]*

4.3.3 Re = 35k

$Re_{U_b} = 35k$

I_W	Re_τ	$[N_x, N_y]$	N_p/I_W	W_{str}	SDR_{th}	$\frac{du}{dy}_{\Delta t}$
[72 72]	950	[111 74]	11	142.5	[55 37]	0.36
[128 40]	950	[62 133]	11	142.5	[31 66]	0.20

Table 4.7: *Some key parameters from the water experiment with Flashe particles with $Re_{U_b} = 35000$.*

$Re_{U_b} = 35k$

I_W	Re_τ	$[N_x, N_y]$	N_p/I_W	W_{str}	SDR_{th}	$\frac{du}{dy}_{\Delta t}$
[72 72]	950	[111 74]	11	142.5	[55 37]	0.50
[128 40]	950	[62 133]	11	142.5	[31 66]	0.26

Table 4.8: *Some key parameters from the water experiment with Polyamid particles with $Re_{U_b} = 35000$.*

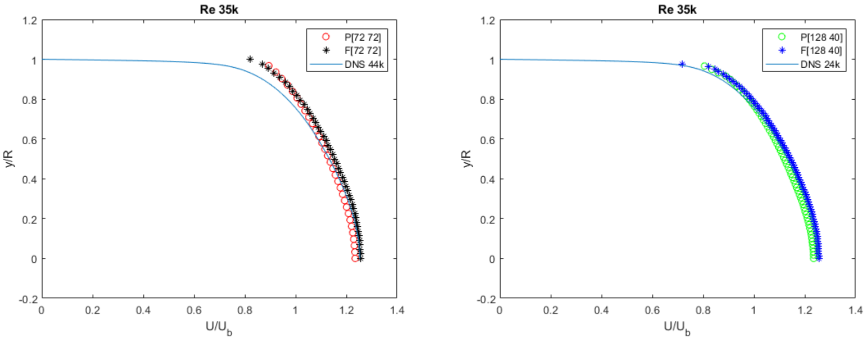

(a) $I_W[72 \quad 72]$ (b) $I_W[128 \quad 40]$

Figure 4.18: *Normalized $\bar{U}$ for Flashe (F) and Polyamid (P) particles on both the left and right compared with DNS data from Wu and Moin(2008)[7].*

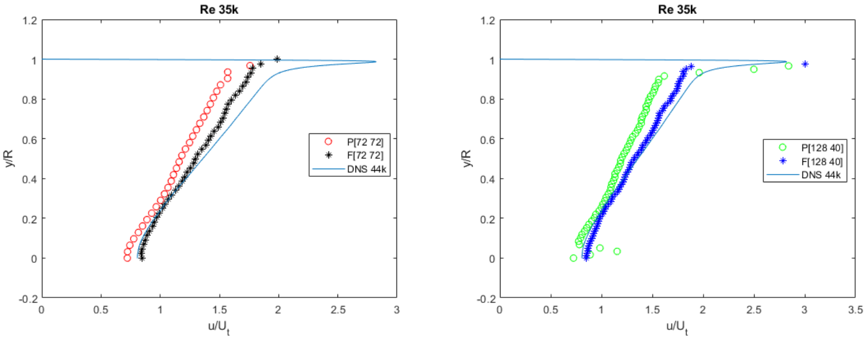

(a) $I_W[72 \quad 72]$ (b) $I_W[128 \quad 40]$

Figure 4.19: *Normalized u' for Flashe (F) and Polyamid (P) particles on both the left and right, compared with DNS data from Wu and Moin(2008)[7]*

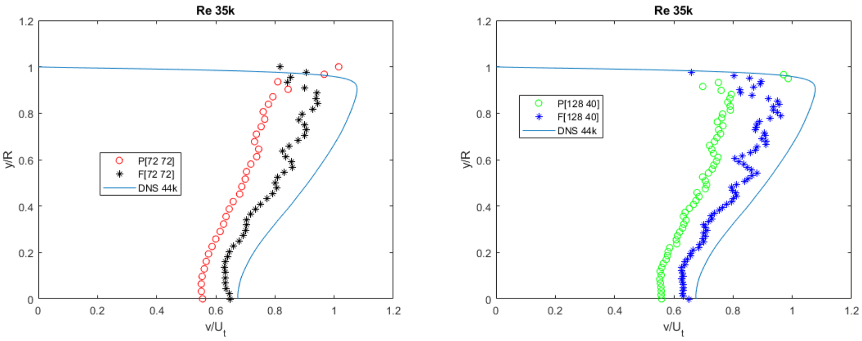

(a) $I_W[72 \quad 72]$ (b) $I_W[128 \quad 40]$

Figure 4.20: *Normalized v' for Flashe (F) and Polyamid (P) particles on both the left and right, compared with DNS data from Wu and Moin(2008)[7]*

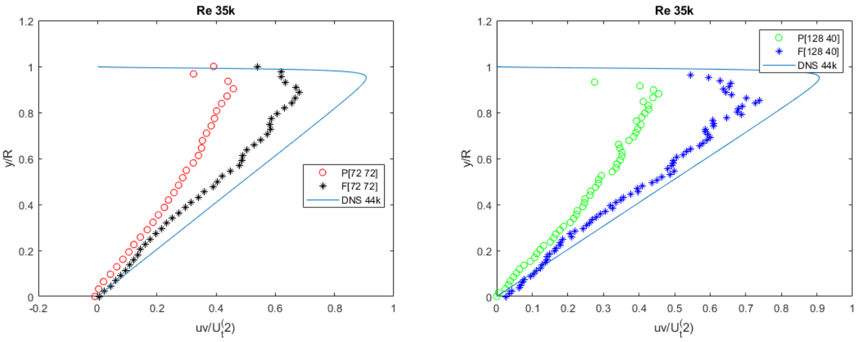

(a) $I_W[72 \quad 72]$ (b) $I_W[128 \quad 40]$

Figure 4.21: *Normalized $u'v'$ for Flashe (F) and Polyamid (P) particles on both the left and right, compared with DNS data from Wu and Moin(2008)[7]*

4.4 Kolmogorov spectras

The power density spectres have been compared with the Kolmogorov spectra for both the longitudal u and radial v fluctuating components, at three different pipe positions: at the vicinity of the pipe wall , at $y/R = 0.5$ and at $y/R = 0$ for the two particles and for both window sizes. The span of frequency band are presented in tables for every particle and subwindow size. The frequencies are calculated as mentioned in section3.4.3 by multiplying the spatial frequencies with the mean velocity.

. It is important to notice that the power density spectre for frequencies higher than the mean velocity divided by 2IW is within the noise floor and no frequency larger than f = UIW can be re-solved due to the size of the interrogation window, see Scharnowski(2018)[2].The resolved frequency and wave length are presented in table 3.2.

4.4.1 15-17k

$\boldsymbol{Re_{U_b}} = 15k$ *Flashe*

I_W	$f[Hz] = \frac{U}{I_{W_x}}$	$f[Hz] = \frac{U}{I_{W_y}}$	$k[1/m]$
[72 72]	3000	3000	[$4mm$ $4mm$]
[128 40]	2500	5000	[$8mm$ $4mm$]

Table 4.9: $f[Hz]$ *corresponds to the highest theoretical resolved frequency outside the noise floor and* k *the corresponding wave number in mm.*

$\boldsymbol{Re_{U_b}} = 17k$ *Polyamid*

I_W	$f[Hz] = \frac{U}{I_{W_x}}$	$f[Hz] = \frac{U}{I_{W_y}}$	$k[1/m]$
[72 72]	2500	2500	[$6mm$ $5mm$]
[128 40]	1600	3300	[$10mm$ $2mm$]

Table 4.10: $f[Hz]$ *corresponds to the highest possible theoretical resolved frequency outside the noise floor and* k *the corresponding wave number in mm.*

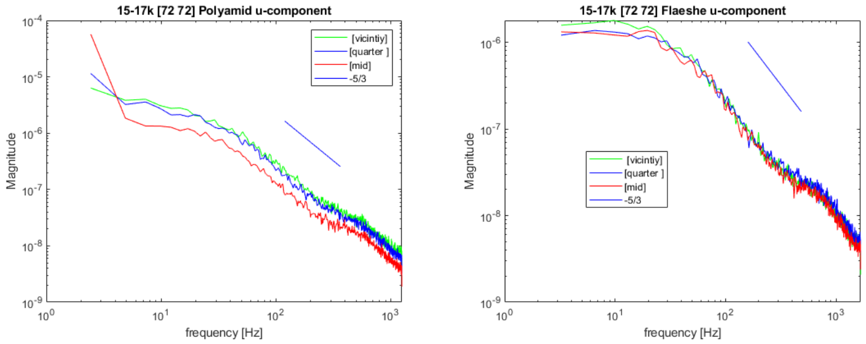

(a) *Polyamid*[I_W[72 72]

(b) *Flaeshe*[I_W[72 72]

Figure 4.22: *The Kolmogorov spectra* $-5/3$ *compared with the longitudinal* u *component PIV spectra of three different pipe positions: the pipe wall, quarter pipe and mid pipe. On the left the Polyamid particle and on the right the Flashe.*

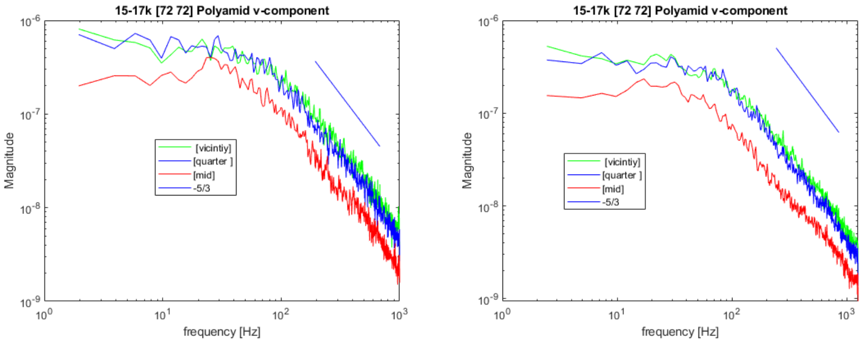

(a) *Polyamid* $I_W[72 \quad 72]$ (b) *Flashe* $I_W[72 \quad 72]$

Figure 4.23: *The Kolmogorov spectra* $-5/3$ *compared with the radial component* v *PIV spectra of three different pipe positions: the pipe wall, quarter pipe and mid pipe. On the left the Polyamid particle and on the right the Flashe.*

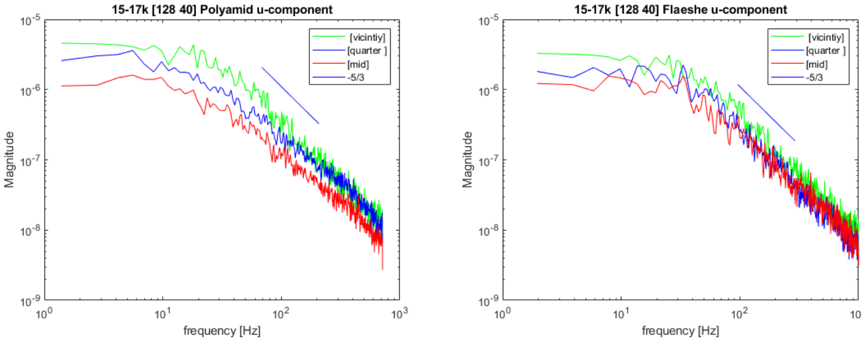

(a) *Polyamid* $I_W[128 \quad 40]$ (b) *Flashe* $I_W[128 \quad 40]$

Figure 4.24: *The Kolmogorov spectra* $-5/3$ *compared with the longitudinal* u *component PIV spectra of three different pipe positions: the pipe wall, quarter pipe and mid pipe. On the left the Polyamid particle and on the right the Flashe.*

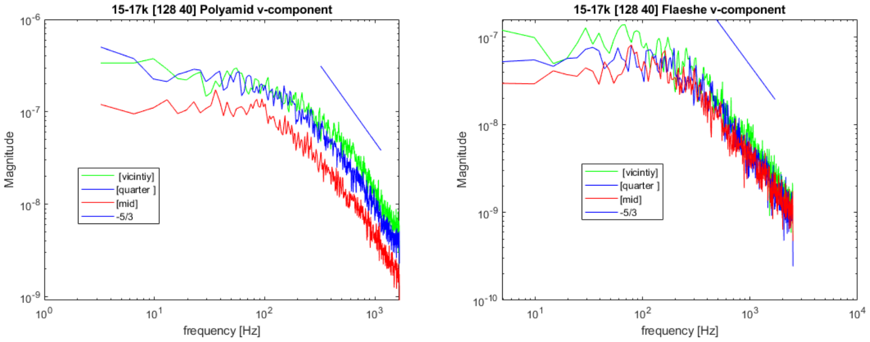

(a) *Polyamid* $I_W[128 \quad 40]$ (b) *Flashe* $I_W[128 \quad 40]$

Figure 4.25: *The Kolmogorov spectra* $-5/3$ *compared with the radial component* v *PIV spectra of three different pipe positions: the pipe wall, quarter pipe and mid pipe. On the left the Polyamid particle and on the right the Flashe.*

4.4.2 Re-23-25k

$\boldsymbol{Re_{U_b}} = 23k \quad Flashe$

I_W	$f[Hz] = \frac{\bar{U}}{I_{W_x}}$	$f[Hz] = \frac{\bar{U}}{I_{W_y}}$	$k[1/m]$
[72 72]	1000	1000	$[4mm \quad 4mm]$
[128 40]	1000	3300	$[8mm \quad 4mm]$

Table 4.11: $f[Hz]$ *corresponds to the highest theoretical resolved frequency outside the noise floor and* k *the corresponding wave number in mm.*

$\boldsymbol{Re_{U_b}} = 25k \quad Polyamid$

I_W	$f[Hz] = \frac{\bar{U}}{I_{W_x}}$	$f[Hz] = \frac{\bar{U}}{I_{W_y}}$	$k[1/m]$
[72 72]	1000	1000	$[6mm \quad 5mm]$
[128 40]	500	2000	$[10mm \quad 2mm]$

Table 4.12: $f[Hz]$ *corresponds to the highest theoretical resolved frequency outside the noise floor and* k *the corresponding wave number in mm.*

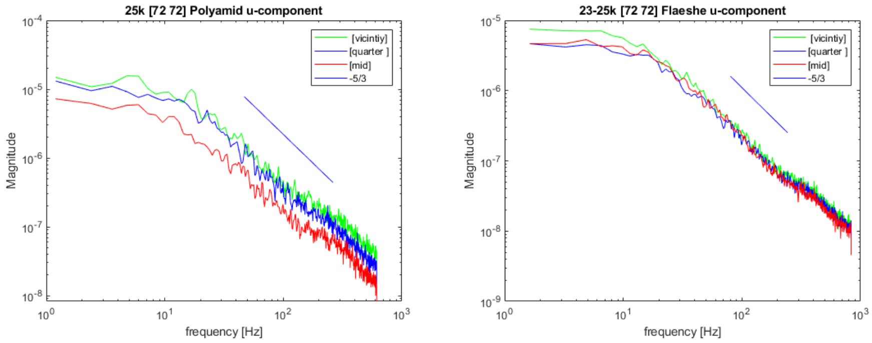

(a) Polyamid $I_W[72 \quad 72]$ (b) Flashe $I_W[72 \quad 72]$

Figure 4.26: *The Kolmogorov spectra* $-5/3$ *compared with the logitudinal component u PIV spectra of three different pipe positions: the pipe wall, quarter pipe and mid pipe. On the left the Polyamid particle and on the right the Flashe.*

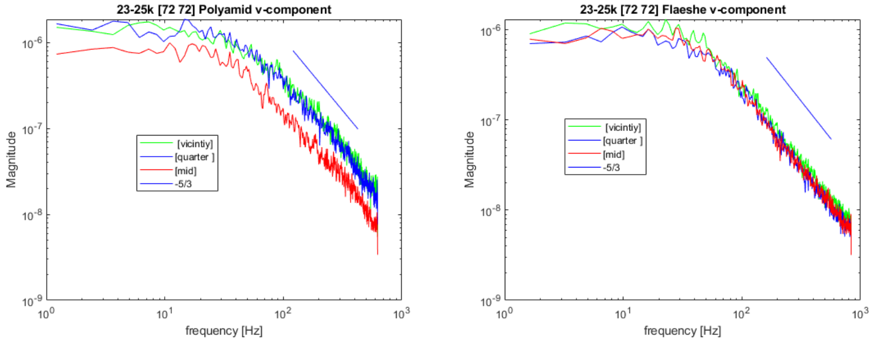

(a) Polyamid $I_W[72 \quad 72]$ (b) Flashe $I_W[72 \quad 72]$

Figure 4.27: *The Kolmogorov spectra* $-5/3$ *compared with the radial component v PIV spectra of three different pipe positions: the pipe wall, quarter pipe and mid pipe. On the left the Polyamid particle and on the right the Flashe.*

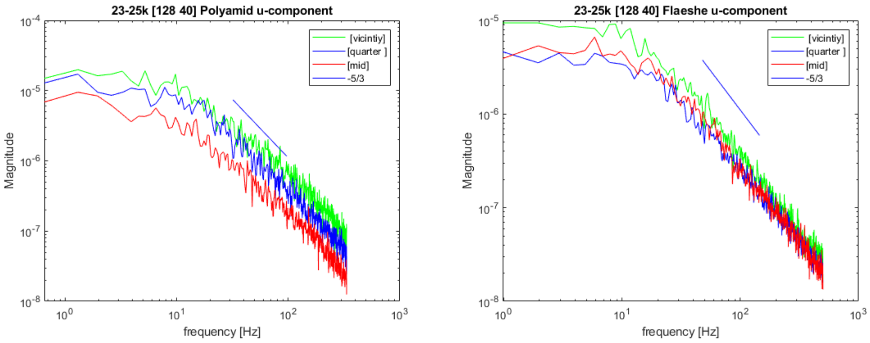

(a) Polyamid $I_W[128 \quad 40]$ (b) Flashe $I_W[128 \quad 40]$

Figure 4.28: *The Kolmogorov spectra* $-5/3$ *compared with the longitudinal component u PIV spectra of three different pipe positions: the pipe wall, quarter pipe and mid pipe. On the left the Polyamid particle and on the right the Flashe.*

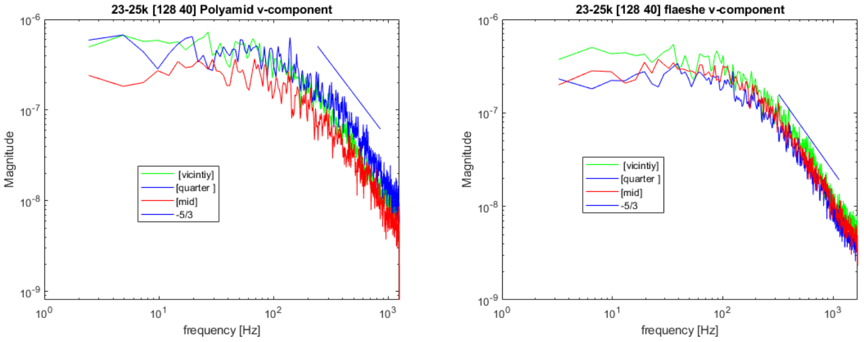

(a) Polyamid $I_W[128 \quad 40]$ (b) Flashe $I_W[128 \quad 40]$

Figure 4.29: *The Kolmogorov spectra* $-5/3$ *compared with the radial component v PIV spectra of three different pipe positions: the pipe wall, quarter pipe and mid pipe. On the left the Polyamid particle and on the right the Flashe.*

4.4.3 Re= 35k

$\boldsymbol{Re_{U_b}} = 35k \quad Flashe$

I_W	$f[Hz] = \frac{U}{I_{W_x}}$	$f[Hz] = \frac{U}{I_{W_y}}$	$k[1/m]$
$[72 \quad 72]$	1250	1250	$[4mm \quad 4mm]$
$[128 \quad 40]$	70	2500	$[8mm \quad 4mm]$

Table 4.13: $f[Hz]$ *corresponds to the highest theoretical resolved frequency outside the noise floor and k the corresponding wave number in mm.*

$\boldsymbol{Re_{U_b}} = 35k \quad Polyamid$

I_W	$f[Hz] = \frac{U}{I_{W_x}}$	$f[Hz] = \frac{U}{I_{W_y}}$	$k[1/m]$
$[72 \quad 72]$	1000	1000	$[6mm \quad 5mm]$
$[128 \quad 40]$	50	200	$[10mm \quad 2mm]$

Table 4.14: *$f[Hz]$ corresponds to the highest possible theoretical resolved frequency and k the corresponds to the wave number for that frequency in mm.*

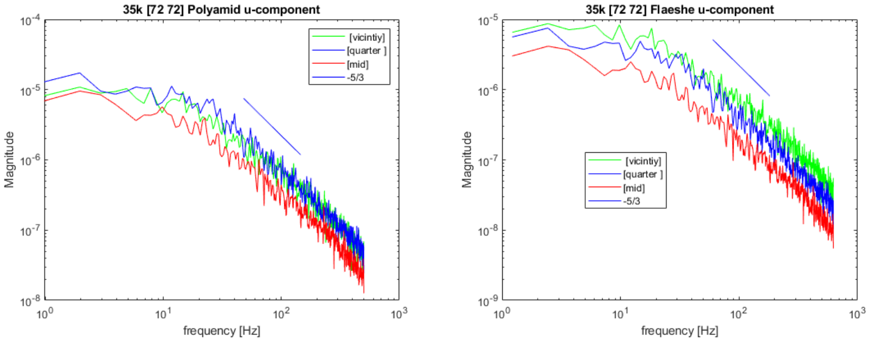
35k [72 72] Polyamid u-component

35k [72 72] Flaeshe u-component

(a) Polyamid $I_W[72 \quad 72]$ (b) Flashe $I_W[72 \quad 72]$

Figure 4.30: *The Kolmogorov spectra $-5/3$ compared with the longitudinal component u PIV spectra of three different pipe positions: the pipe wall, quarter pipe and mid pipe. On the left the Polyamid particle and on the right the Flashe.*

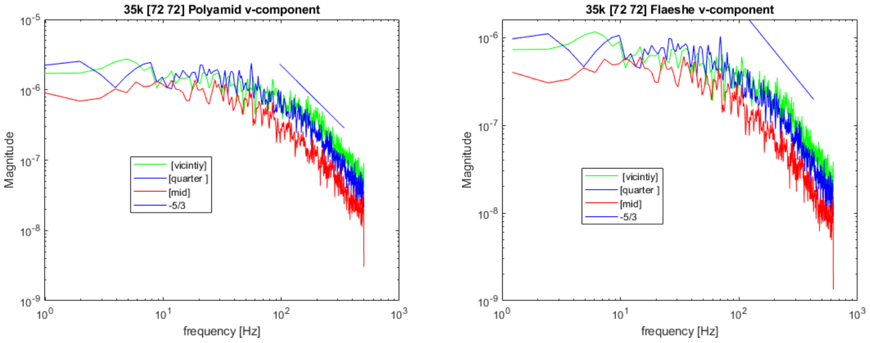
35k [72 72] Polyamid v-component

35k [72 72] Flaeshe v-component

(a) Polyamid $I_W[72 \quad 72]$ (b) Flashe $I_W[72 \quad 72]$

Figure 4.31: *The Kolmogorov spectra $-5/3$ compared with the radial component v PIV spectra of three different pipe positions: the pipe wall, quarter pipe and mid pipe. On the left the Polyamid particle and on the right the Flashe.*

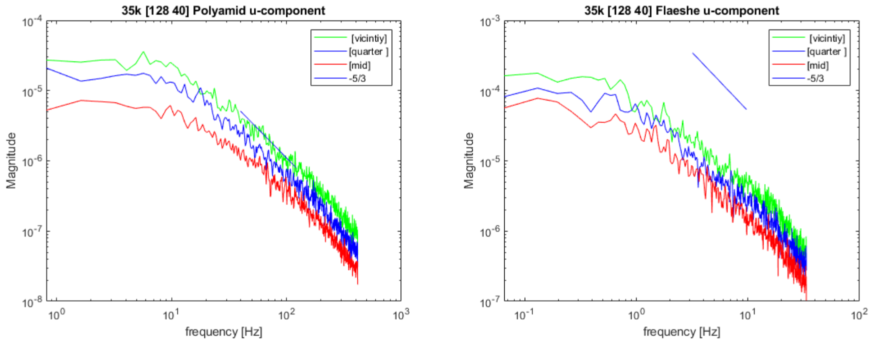

(a) Polyamid $I_W[128 \quad 40]$ (b) Flashe $I_W[128 \quad 40]$

Figure 4.32: *The Kolmogorov spectra* $-5/3$ *compared with the longitudinal component u PIV spectra of three different pipe positions: the pipe wall, quarter pipe and mid pipe. On the left the Polyamid particle and on the right the Flashe.*

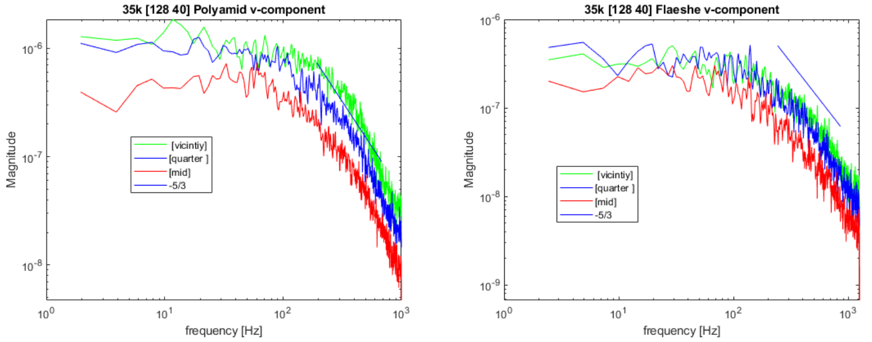

(a) Polyamid $I_W[128 \quad 40]$ (b) Flashe $I_W[128 \quad 40]$

Figure 4.33: *The Kolmogorov spectra* $-5/3$ *compared with the radial component v PIV spectra of three different pipe positions: the pipe wall, quarter pipe and mid pipe. On the left the Polyamid particle and on the right the Flashe.*

Chapter 5

Conclusion

A validation of a single phase gas experiment seeded with $1-6\mu m$ water particles have been conducted at $Re_{U_b}=44k$ and compared with DNS results from Wu and Moin(2008)[7]. Excellent results regarding the mean velocity profile and satisfying results regarding turbulence profiles were obtained. A spectral density analysis were made as well which showed varying results. Six single phase water cases have been conducted whereof three ($Re_{U_b}=15,23,35k$) where seeded with $2-10\mu m$ fluorescent particles extracted from commercial acrylic Flashe color and the other three($Re_{U_b}=17,25,35k$) with commercial $50\mu m$polyamide particles. Cases with corresponding Reynolds number have then been compared in pairs through mean flow characteristics, turbulence profiles and Kolmogorov spectras. Due to some unfortunate circumstances regarding the pre-experimental preparations and a broken pressure gauge, the comparison turned out a bit unfair. Regardless, both particles followed the mean flow characteristics very good and the rms u' profile turned out good as well. Some questions remain unanswered about the rms v' profiles. A spectral analysis were also performed for each case to compare the particles. Both particles proved to capture the decay of the turbulent energy in the fluid very well according to the theory of Kolmogorov. The Flashe particle proved to be a little bit it more sensitive to peak locking but had better quality in the PIV frames concerning reflections. In all, no big distinction in the particles abilities to reflect the fluid motions have been found.

Chapter 6

Appendix

6.1 Flashe Particles

6.1.1 Preparation

The Flashe particles was prepared by mixing approximately 15ml of paint with fresh water into a bucket equipped with a tap. The tap outlet are attached around 2 cm above the bottom of the bucket. By letting the mixture rest, the heavier particles of color will sink to the floor of the bucket and form a base. After approximately 24 hours the bucket is tapped for mixture through the outlet and thus leave the residue situated at the bottom under the outlet. The former procedure/step is then repeated one other time. The remaining residue, constituted the base from which the water phase where seeded.

Figure 6.1: *An image of the jar with the orange color that where used to produce the seeding base.*

6.1.2 Average diameter

To find the average diameter we start by pouring a thin layer of seeding base in a transparent crystallizing dish. The dish are placed upon a graph paper with a $1 \times 1mm$ grid, giving us a one to one conversion from pixels to meters. This constellation is installed under the lens of a microscope to magnify the area of interest. A photograph as in figure 6.2 were then taken and used for further processing.

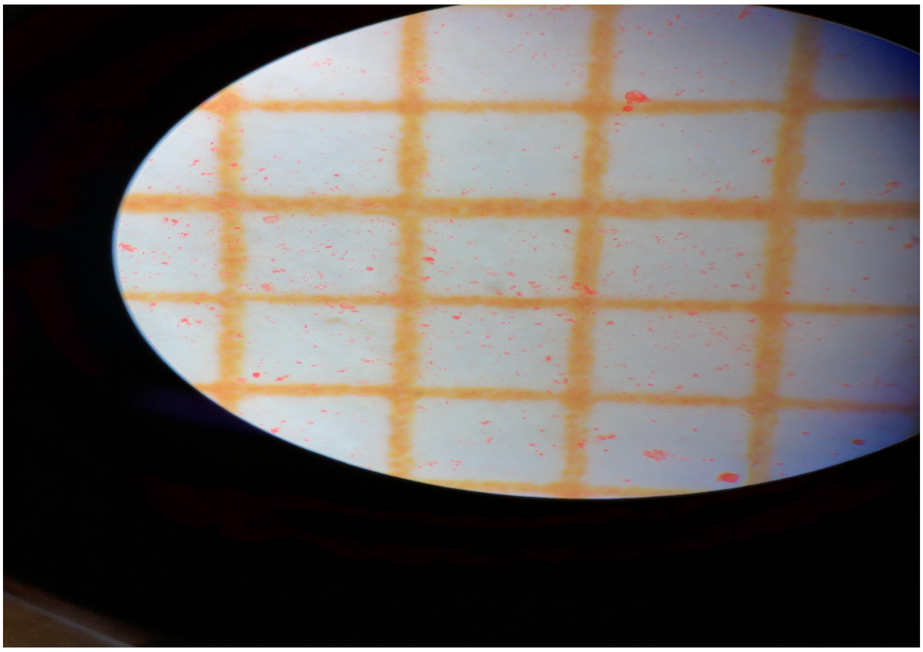

Figure 6.2: *Image of the particles on top of the* $1 \times 1mm$ *grid seen through the microscope.*

In the next step we crop out a square from figure 6.2 to get a close up of the particles, as seen in figure 6.3a. Then we binarize the cropped image 6.3a by using the Matlab function $im2bw([image], [px_{value}])$ to obtain figure 6.3b. Where the first argument is the particular image of interest and the second argument, $[px_{value}]$, is a level threshold for the binarization and it had to be adjusted for each single square.

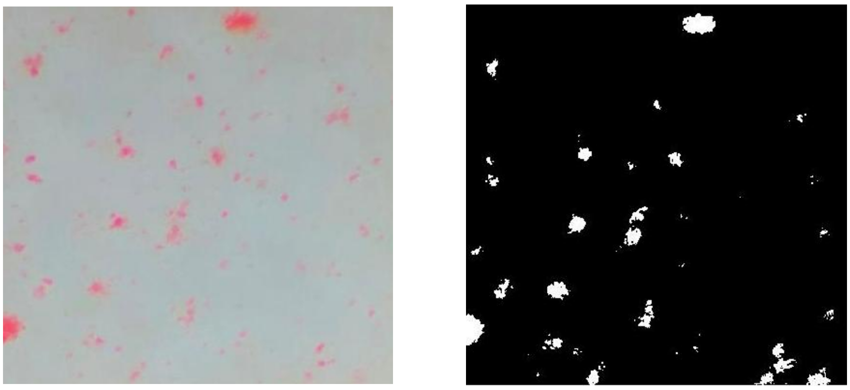
(a) *A cropped square from figure 6.2.* (b) *Binarized version of figure 6.3a.*

Figure 6.3

At last, by feeding the binarized images in to the Matlab function $regionprops()$, we obtain among others, the number of particles and the diameter for each particle. A distribution of the particle size is thereafter computed and the result can be seen in figure 6.4.

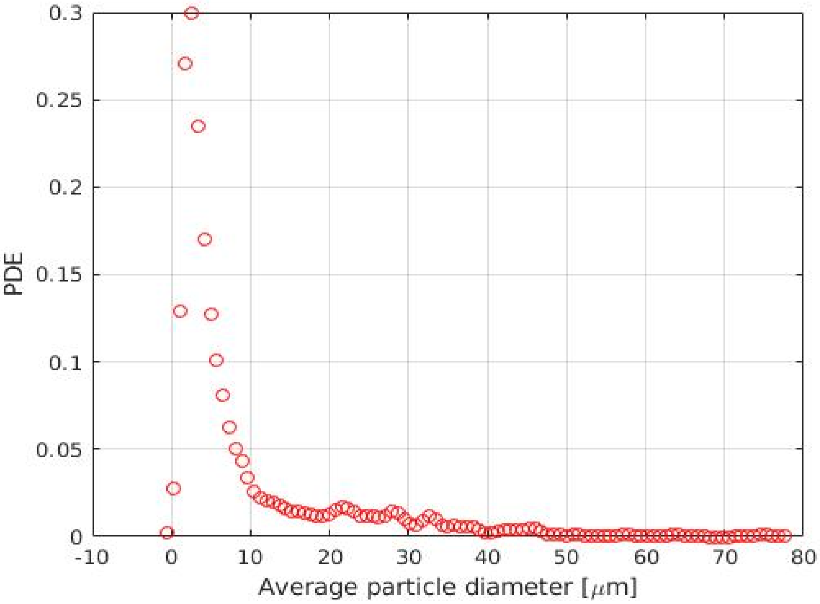

Figure 6.4: *Particle size distribution of the seeding sample.*

A total number of ten squares where processed and these squares contained around 400 particles. The mean diameter where found to be around $1-10\mu m$ and as can be seen in the PDF 6.4, the majority of particles are below $30\mu m$.

6.1.3 Density

The density of the Flashe paint were approximated by comparing the weight of 20ml amount of paint and compare it to the weight of 20ml of water on a digital ML-T precision scale from Mettler Toledo.

6.2 Matlab code

The most important matlab scripts are presented in this section.

Background subtraction

```
% program to remove background noise
addpath('/run/media/martingy/Seagate Backup Plus Drive/18_3/TempPCO5');

im = sprintf('im_00001.tif',1);



im = imread(im);
split = 5344;
im1 = (im(1:end,1:end));

%define preliminary background noise image
im_background = zeros(length(im1(:,1)), length(im1(1,:)));
%make an white image
im_background = im2uint16(im_background) + 65655;


% create an image background for the specific case in the path of all the
% 500 images
K = 500;

for k = 1:K
% read in each image to compare values with im_background
im = sprintf('im_00%03d.tif', k);
im = imread(im);
im1= (im(1:end, 1:end));

%loop over each pixel position, compare values with image_background and possibly switch
for i = 1:length(im_background(:, 1))

    for j = 1:length(im_background(1,:))
         A = im1(i,j);
       B = im_background(i,j);
```

```
        %replace the lowest value (lowest value is a black pixel)
        if A < B
        im_background(i,j) = im1(i,j);
         end
       end
    end
end

% subtract one from the im_background so that it does'nt mask in case
%of max values (initial value) in im_background when subtracting from original images.
im_background = im_background - 1;
%Create filtered images by using the created background and store
K2 = 500;
mkdir '/run/media/martingy/Seagate Backup Plus Drive/18_3/TempPCO5/filtered'
for k = 1:K2
k
im = sprintf('im_00%03d.tif', k);
im = imread(im);
im1 = (im(1:end, 1:end));
% subtract background from origninal image
im_filtered = im1 - im_background;
nr = sprintf('%03d', k);
imwrite(im_filtered, ['/run/media/martingy/Seagate Backup Plus Drive/18_3/TempPCO5/filtered/imf_00' nr '.tif'], 'Compression', 'none');
end
```

PIV algorithm

```
%Program to use the PIV algortihm from hydroLab PIV
path = 'D:\18_3\TempPCO3\filtered'
addpath(genpath('D:\Desktop\SEBASTIAN\master\HydrolabPIV\src'));
addpath('D:\18_3\TempPCO3\filtered');
javaaddpath('D:\Desktop\SEBASTIAN\master\HydrolabPIV\src\measures');
javaaddpath('D:\Desktop\SEBASTIAN\master\HydrolabPIV\src\interp');


%
str = sprintf('imf_00001.tif',1);
% since the image pairs are fit together on top of eachother we need to
% split them into two before creating the mask
```

```
im = imread(str);
split = 5344/2; % pixel height = 5344.  splity in to two images
im1 = (im(1:split,:));
im2 = (im((split +1):5344, :));

% in case of half window post processing
%im1 = im1(1:end/2, :);
%im2 = im2(1:end/2,:);


% create a polygonal mask to mask away sections outside the pipe
figure;
imagesc(im1, [0,2500]); % setting of the image intensity treshhold (arbitrary)
set(gca,'Ydir','normal')
h = impoly();
mask = h.createMask();



% number of images to process
K = 500;
numer = 1;
% make a directory to store the PIV structures
mkdir  'D:\18_3\TempPCO3\filtered\pivf12840'
for k = 1:K
    %reading in image number
    str = sprintf('imf_00%03d.tif',k);
    im = imread(str);
    % separate the image to get a distinct image pair
    im1 = (im(1:2672,:));
    im2 = (im(2673:5344,:));
    %im1 = im1(1:end/2, :);
    %im2 = im2(1:end/2,:);
    % set piv options. Use the same mask for both images to keep the same
    % form of the velocity field
    %                          X  X   Y  Y   X    Y  O_L
    opt = setpivopt('range',[-64 64 -20 20],'subwindow',128, 40,.50);
    piv = normalpass([],im1, mask,im2,mask,opt);
    % using the outlier function to discard outlier vectors
    [U,V,x,y]= replaceoutliers(piv);

    % save the information from each image pair in a separate struct
```

```
    nr = sprintf('%03d', k);
    save([ path '\pivf12840\piv00' num2str(nr) '.mat'],'piv','x','y','U','V', 'piv' );
    number = number + 1

end
```

Turbulent profiles

```
%This program reads in the PIV structs and calculates the mean and turbulence
%profiles
%

% establish the paths
addpath(genpath('/media/sebastian/Seagate Backup Plus Drive/Desktop/SEBASTIAN/master/HydrolabPIV/src'));
addpath('/media/sebastian/Seagate Backup Plus Drive/exp_water_25_2/TempPCO2/filtered/pivf12840');
javaaddpath('/media/sebastian/Seagate Backup Plus Drive/Desktop/SEBASTIAN/master/HydrolabPIV/src/measures');
javaaddpath('/media/sebastian/Seagate Backup Plus Drive/Desktop/SEBASTIAN/master/HydrolabPIV/src/interp');

% number of structs/image pairs
K = 500;


% coordinate transform
coord= imread('D:\exp_water_25_2\Coord2.tif');
imagesc(coord,[0, 4000])

%Select reference points in pixel coordinate
h=impoly;
pixel = h.getPosition;

% Define matching reference points in world coordinate
[wx,wy] = ndgrid((0:1:9)*0.015 + 0,( 0:1:9)*0.01 + 0.005);
world = [wx(:) wy(:)];

% Create coordinate transformation
[tform,err,errinv] = createcoordsystem(pixel,world,'cubic')

% define correct dt
dt = 700*10^(-6);

U_concatenate = [];
V_concatenate = [];
```

```


% slice the end parts of the piv field to avoid outliers and erroor
xtop = 15; %left side of the piv frame
xlow = 15; %right side of the piv frame
ytop = 5;  % top of the piv frame
ylow = 5; % bottom of the piv frame


% looping thorugh each struct and store each velocoity field in U- and V -concatenate
for i  = 1:K
   % read in struct
   nr = sprintf('%03d', i);
   load(['piv00' num2str(nr) '.mat']);

   % transforming from pixel to world coordinates
   [U,V,x,y] = pixel2world(tform,U,V, x,y,dt);

   %concatenate velocity fields. It is importante to cut in the image first AFTER the coordinate transform
   U_concatenate = [U_concatenate,{U(ytop:end-ylow, xtop:end-xlow)}];
   V_concatenate = [V_concatenate,{V(ytop:end-ylow,xtop:end-xlow)}];

end

%Create super matrix 500X * Y
U = cell2mat(U_concatenate);
V = cell2mat(V_concatenate);

% calculating the mean velocity profiles
U_mean = mean(U,2);
V_mean = mean(V,2);

% extract the velocity fluctuations
u = U - U_mean;
v = V - V_mean;
% calculating the turbulence profiles rms u and rms v and the reynold stress uv
rmsu = rms(u,2);
rmsv = rms(v,2);
uv = mean(u.*v,2);

% find the maximum mean velocity and the corresponding position on the Y axis
[max_num, max_idx]=max(U_mean(:));
[Y]=ind2sub(size(U_mean),max_idx);
```

```

% vectors to plot the profiles and the streamline signals
ylong = linspace(1,0,length(U_mean(Y:end)));
xlong = linspace(1,length(u(1,:)),length(u(1,:)));

%save all vectors and variables into a struct
data = struct('path',path,'U_temp', U ,'V_temp', V, 'U', U_mean, 'V', V_mean, 'u', u, 'v', v, 'rmsu', rmsu, 'rmsv', rmsv, 'uv', uv, 'x', piv.x, 'y', piv.y, 'xlong', xlong, 'ylong',ylong,'U_mean', U_mean,'dt', dt,'Y', Y,'ylong2', ylong2)
datac12840= struct( 'data', data, 'piv', piv )
```

Welch Spectra

```
% program to calculate the power denisty spectras


%Fs = (1/spatial frequency)*mean velocity
Fs  = 1/0.001

% define the signal to consider
pipe = length(data7272.data.u(:,1))
signal1 = datac7272.data.u(floor(10),:);

%compute the spectral density with welch method.
%default values: 8 segments, 50% overlap and hamming window
[psi, freq1] = pwelch(signal1, [1000],[],[], Fs);

% same for the other signals
signal2 = data7272.data.u(floor(pipe/4), :);
[psi2, freq2] = pwelch(signal2,[1000],[],[], Fs);

signal3 = data7272.data.u(floor(pipe/2),:);
[psi3, freq3] = pwelch(signal3,[1000],[],[], Fs);


% plot statements
figure(1);
loglog(freq1, psi, 'g');
hold on
loglog(freq2, psi2, 'b');
hold on
loglog(freq3, psi3, 'r');
hold on
% compare wiht Kolmogorov spectra
loglog(freq1(50:150), 1.5*freq1(50:150).^(-5/3), 'b')
xlabel('frequency [Hz]')
ylabel('Magnitude')
```

```
legend(' [vicintiy]','[quarter ]','[mid]', '-5/3')
title('35k [72 72] Polyamid u-component')
```

The mass flow rate

```
% calculation of the mass flow rate through a pipe
% int2(rho*U(r)*dA)
% where dA = deltaR*deltaTheta and we integrate over 0< r 0.1 and 0 <theta < 2pi


% define integrand area
%U_profile = flip(U_mean(1:end/2);
r = linspace(0, 0.05, length(U_profile));
theta = linspace(0,2*pi, 10000);
%r = flip(r);
% define mesh size (quadratic mesh)
deltaR = r(2) - r(1);
deltaTheta = theta(2)- theta(1);

% constants
%rho = 1.2; % gas at 20 degrees celsius
rho = 998; % water at 20 degrees celsius

% define mdot array
mdot = zeros(length(theta),1);

for j  = 1:length(theta(1:end-1))

mdot_column = 0;
mdot_temp = 0;

  for i = 2:length(r+1)

   % calculate flux through an area deltaR*deltaTheta with trapez
   U_avg = U_profile(i);

   %Uavg =  (U_profile(i)+U_profile(i-1))/2;

   mdot_temp = U_avg*(deltaR*(r(i-1) + r(i))*deltaTheta)/2;

   % add each value in mdot_temp and sum up
   mdot_column = mdot_column + mdot_temp;

  end
 % store each column in mdot array
  mdot(j) = mdot_column;

```

```
end
mdot_column = 0;
mdot_temp = 0;
% sum each column
mdot = rho*sum(mdot)
```

Seeding stats

```
% program to calculate number of particles, particle per IW and particle size.


addpath('D:\16_4\TempPCO3\filtered');

% read in an image from the given path. split in two to get
% the correct target
im = sprintf('imf_00001.tif',1);
im = imread(im);
split = 5344/2;
im1 = (im(1:end/2,1:end));
%im1 = (im((end/2 +1):end, :));

%visualize to check threshold and to compare with binarized
figure(1)
imshow(im(2672+300:end-300 , 1:end), [0 400])


% cut out piece of original image to compare with binarized of the same cut
figure(2)
imshow(im(300:400+300 ,1:400), [0 400])
h = gca;
h.Visible = 'on';
ylabel('pixels')
xlabel('pixels')
% slicing off the edges of the imported image to avoid pollution of the
% egdes where reflections are strong
pre_bw = (im(1+300:end/2-300 , 1:end));
%binarizing the image pre_bw with appropriate treshold
bw = imbinarize(pre_bw, 0.001);
%visualizing
figure(3)
imshow(bw)
figure(4)
imshow(bw(1:400 ,1 :400))

g = gca;
```

```
g.Visible = 'on';
ylabel('pixels')
xlabel('pixels')
stats = regionprops('table', bw, 'Centroid','MajorAxisLength' ,'MinorAxisLength','Area' );

% compting mean diameters and number of particles
meanDiameters = mean([stats.MajorAxisLength stats.MinorAxisLength], 2);
meanDiameter = mean(meanDiameters)
numberOfparticles = length(meanDiameters)
% define are of each subwindow in pixels
subWindow =72*72;
subWindow2 = 128*40;
% computing particles per interrogation window by assuming homogenous
% disributed particles
pixles = 2672*4008;
particlesPerIw = numberOfparticles/((pixles)/(subWindow))
particlesPerIw2 = numberOfparticles/((pixles)/(subWindow2))
% particle distribution in pixels
histfit(meanDiameters)
xlabel('pixels')
ylabel('number of particles')
xlabel('diameters in pixels')
```

Density of particles

```
% A program to estimate the density of the particles by using the
% a program to estimate the density of particles from a binarized image.

%reading in the positions in x and y of the image particles from stats
xi = (stats.Centroid(:,1));
yi = (stats.Centroid(:,2));
% visualisation of the particles for manual inspection
figure(5);
plot(xi, yi,'.');
title('Particle density')
xlabel('streamwise')
ylabel('radius')




% define an evenly spaced area of where the particles lies.
```

```
% dont make the space to large (n not to big), we want enough particles per square
n  = 50;
% defining the pixel size of the image
x = linspace(1, 4008,n);
y = linspace( 1,2672,n);
%defining grid
xn = linspace( min(x(:)),max(x(:)), n);
yn = linspace(min(y(:)), max(y(:)), n);


% interp1 returns interpolated values of at the specific query points (xn)
% using interpolation. xn contains the sample points and 1:numel(xn) the
% corresponding value and xi the coordinates of the query points.
% same for xr and yr.for this case we put all the data points to the
% closest integer(grid box)

xr = interp1(xn, 1:numel(xn), xi, 'nearest');
yr = interp1(yn, 1:numel(yn), yi, 'nearest');

% creating a Z field of xr and yr to visualize the density.
% first argument is the vectors to be accumulated, the second
%argument means that each data point is accounted for 1 in the accumarray Z
% and the last argude is the dimension of the output
Z = accumarray([xr (yr)], 1, [n n]);


figure(6);
surf(Z)
xlabel('streamwise')
ylabel('radius')
title('Density histogram for flaeshe particles ')
colorbar()
```

6.3 Brasil

In this section are the remains of the experimental campaign that were conducted at PUC-Rio, Rio de Janeiro in Brazil. The stay in Brazil primarily consisted of an experimental campaign where I together with the guidance of Dr.Igor de Paula and Paula Bormann conducted PIV measurements of stratified air-water flow, in which controlled perturbations were introduced at the pipe inlet. The outcome were a set of base flow profiles as well as profiles with interfacial wave interactions at different flow rate conditions. These profiles where then compared with theoretical profiles by means of an Orr-Sommerfeld solver built by Dr.Espen Aakervik. The resulting nodes of the theoretical and experimental profiles where plotted against a kaffel node spectrum.

6.3.1 Theory

Outline of the stability analysis

The two following disturbance analysis are following the same line of attack. The approach is rather general and it boils down to 7 steps. They go as follows

1. We begin to examine the stability of the basic solution of a physical problem, U_0. The solution will be on a vector form.
2. Add a perturbation variable , U', and substitute $(U_0 + U')$ into the governing equations.
3. From the resulting equations in step 2, subtract with the original base solution U_0 to obtain the perturbation equation.
4. Linearize the perturbation equation by assuming that the perturbations are small, $U' << U_0$, and neglect non-linear terms.
5. Assume a form of the perturbations, preferably a traveling wave.
6. The linearized disturbance equation should be homogeneous and have homogeneous boundary conditions. This is an eigenvalue problem.
7. The eigenvalues found from step 6 can be analyzed to determine whether the equations is stable, unstable or neutrally stable.

Kelvin-Helmholtz instability

The theory that is called up after Lord Kelvin and Hermann von Helmholtz predicts the onset of surface instabilities between two fluids with distinct densities that are flowing with different speed. A sketch of the problem is shown in figure 6.5.

Derivation

For a start a few assumptions are made about the flow conditions. These are that the flow in both regions are incompressible, irrotational and inviscid.Thus both base flows possess a velocity potential and a hydrostatic pressure distribution. They read as follows:

$$z < 0 : \qquad \phi_1 = U_1 x, \qquad p_1 = p_0 - \rho_1 g z \tag{6.1}$$

$$z > 0 : \qquad \phi_2 = U_2 x, \qquad p_2 = p_0 - \rho_2 g z \tag{6.2}$$

Furthermore we will allow for a tangential slip at the interface which implies that we have a discontinuity in velocity. Next we want to introduce a perturbation to both variables which we denote by a "hat":

$$\phi_1 = U_1 x + \hat{\phi_1}(x, z, t) \tag{6.3}$$

$$\phi_2 = U_2 x + \hat{\phi_2}(x, z, t) \tag{6.4}$$

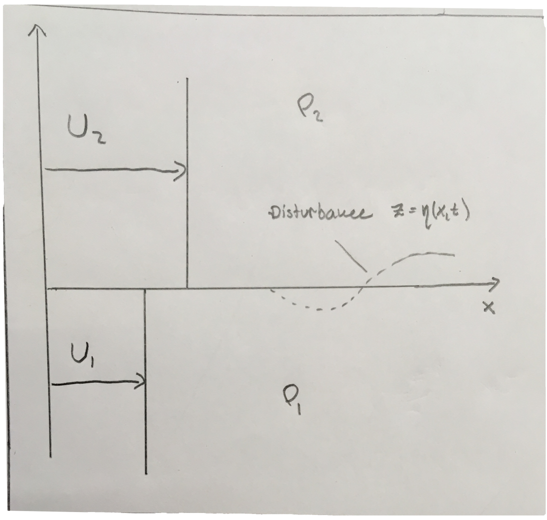

Figure 6.5: Sketch for the Kelvin-Helmholtz instability. The interface before perturbation lies at $z = 0$ and is coinciding with the x-axis.

Both $\hat{\phi}_1$ and $\hat{\phi}_2$ satisfy the Laplace equation. As shown in figure 6.5 we also perturb the interface, i.e. $z = \eta(x, t)$. When the flow is perturbed we'll get an unsteady pressure which satisfy the unsteady Bernoulli relation:

$$p_i = C_i - \rho_i \frac{\partial \phi_i}{\partial t} - \frac{\rho_i}{2} |\nabla \phi_i|^2 - \rho_i g z \qquad \text{for regions} \quad i = 1, 2 \tag{6.5}$$

At $z = 0$ when there is no disturbance we get that:

$$C_1 - \frac{\rho_1}{2} U_1^2 = C_2 - \frac{\rho_2}{2} U_2^2 \tag{6.6}$$

In order to close this problem we need to set up a few boundary conditions. These can be found through physical reasoning about the flow conditions at the interface and in the far field. One boundary condition is that we have a continuous pressure across the interface. By 6.5:

$$\text{At} \quad z = \eta : \qquad C_1 - \rho_1 \frac{\partial \phi_1}{\partial t} - \frac{\rho_1}{2} |\nabla \phi_1|^2 - \rho_1 g z = C_2 - \rho_2 \frac{\partial \phi_2}{\partial t} - \frac{\rho_2}{2} |\nabla \phi_2|^2 - \rho_2 g z + \nu \kappa \tag{6.7}$$

where $\nu\kappa$ is the surface tension. A second condition is that the velocities must match the interfacial motion, there will in other words be no cavities between the fluids.

$$\text{At} \quad z = \eta: \qquad w_i = \frac{\partial \phi_i}{\partial z} = \frac{d\eta}{dt} = \frac{\partial \eta}{\partial t} + \frac{\partial \eta}{\partial x}\frac{\partial x}{\partial t} = \frac{\partial \eta}{\partial t} + \frac{\partial \eta}{\partial x}\frac{\partial \phi_i}{\partial t} \tag{6.8}$$

where we have used the material derivative on $\eta(x, t)$. Other conditions are that the disturbance dies out when we go far from the interface. Mathematically stated as

$$\nabla \hat{\phi}_1 \to 0 \quad \text{as} \quad z \to -\infty \tag{6.9}$$

$$\nabla \hat{\phi}_2 \to 0 \quad \text{as} \quad z \to +\infty \tag{6.10}$$

Now we assume that the introduced disturbance are much weaker than the base flow.

$$g\eta << U_i^2 \quad , \quad \frac{\partial \eta}{\partial x} << 1, \quad |\nabla \hat{\phi}_i| << U_i \tag{6.11}$$

The left part in 6.11 can be thought of as small interfacial displacement, the second part that the slopes are small and the last that disturbance velocities are much smaller than the base flow. By Taylor expanding the perturbations around zero and linearize we may approximate the interfacial conditions at $z = \eta \simeq 0$ to obtain a new simplified pressure condition:

$$\text{At} \quad z \simeq 0 \quad \rho_1\Big(\frac{\partial \phi_1}{\partial t} + U_1\frac{\partial \phi_1}{\partial x} + g\eta\Big) = \rho_2\Big(\frac{\partial \phi_2}{\partial t} + U_2\frac{\partial \phi_2}{\partial x} + g\eta\Big) + \nu\kappa \tag{6.12}$$

where $\nu\kappa$ is the surface tension and furthermore we have used that

$$|\nabla \phi_i|^2 = |U_i + \frac{\partial \phi_i}{\partial x_j}|^2 = U_i^2 + 2U_i\frac{\partial \phi_i}{\partial x_j} + \Big(\frac{\partial \phi_i}{\partial x_j}\Big)^2 \simeq U_i^2 + 2U_i\frac{\partial \phi_i}{\partial x_j} \tag{6.13}$$

The first term in the rightmost part of 6.13 is eliminated by subtracting the base flow with the perturbed flow. By doing this we obtain the disturbance relations. These are the equations we want to analyze in order to deduce if the flow is unstable. We get the kinematic condition at $z \simeq 0$:

$$\frac{\partial \hat{\phi}_1}{\partial z} \sim \frac{\partial \eta}{\partial t} + U_1\frac{\partial \eta}{\partial x} \tag{6.14}$$

$$\frac{\partial \hat{\phi}_2}{\partial z} \sim \frac{\partial \eta}{\partial t} + U_2\frac{\partial \eta}{\partial x} \tag{6.15}$$

(Write something about how the different parts in 6.15 should be interpreted). Our boundary conditions are now reduced to a set of linear linear equations. Rather than solve these equations by assuming a general form of η we are imposing the ansatz that the disturbances are on a simple form; a two dimensional traveling wave or normal modes:

$$\eta = \eta_0 e^{i(\alpha x - \sigma t)} \tag{6.16}$$

$$\hat{\phi}_i = \phi_i^{'}(z) e^{i(\alpha x - \sigma t)} \tag{6.17}$$

where i is the complex unit, σ is the complex frequency and α is the wave number. We notice that $\hat{\phi}_i$ will be unstable if σ is positive. Using the Laplace equation we can now obtain the following ODE for the disturbance coefficient:

$$(\phi_i^{'})^{''} - \alpha^2 \phi_i^{'} = 0 \tag{6.18}$$

with solutions

$$\phi_1^{'}(z) = A_1 e^{\alpha z} \quad \text{and} \quad \phi_2^{'}(z) = A_2 e^{\alpha z} \tag{6.19}$$

that may be substituted back into our interfacial conditions 6.15 to yield expressions for the unknown constants A_1 and A_2. We get

$$A_1 = i\eta_0\Big(U_1 - \frac{\sigma}{\alpha}\Big) \quad \text{and} \quad A_2 = -i\eta_0\Big(U_2 - \frac{\sigma}{\alpha}\Big) \tag{6.20}$$

Hence, we end up with the following equations:

$$\hat{\phi_1} = i\eta_0\Big(U_1 - \frac{\sigma}{\alpha}\Big)e^{\alpha z}e^{i(\alpha x - \sigma t)}, \quad \hat{\phi_2} = -i\eta_0\Big(U_2 - \frac{\sigma}{\alpha}\Big)e^{-\alpha z}e^{i(\alpha x - \sigma t)} \tag{6.21}$$

$$\eta = \eta_0 e^{i(\alpha x - \sigma t)}, \quad \nu\kappa = -\nu\alpha^2 e^{i(\alpha x - \sigma t)} \tag{6.22}$$

At last we are gonna substitute the above equations into the pressure condition 6.12 which leads to the following relation

$$-\rho_1\alpha U_1^2 + \rho_1 U_1\sigma + \rho_1\sigma U_1 - \frac{\rho_1\sigma^2}{\alpha} + \rho_1 g = \rho_2\alpha U_2^2 - \rho_2 U_2\sigma - \rho_2\sigma U_2 - \frac{\rho_2\sigma^2}{\alpha} + \rho_2 g - \nu\alpha^2 \tag{6.23}$$

$$\sigma^2(\rho_1 + \rho_2) - 2\sigma\alpha(\rho_2 U_2 + \rho_1 U_1) + \alpha g(\rho_2 - \rho_1) - \nu\alpha^3 = 0 \tag{6.24}$$

6.24 is recognized as a second degree polynomial and can be solved wrt σ by using the abc-formula.

$$\sigma = \frac{\alpha(\rho_1 U_1 + \rho_2 U_2)}{\rho_1 + \rho_2} \pm \sqrt{\frac{\alpha\rho_1\rho_2(U_1 - U_2)^2}{(\rho_1 + \rho_2)^2} - \frac{\alpha g(\rho_2 - \rho_1) + \nu\alpha^3}{(\rho_1 + \rho_2)}} \tag{6.25}$$

As mentioned earlier; the perturbation is stable if $\sigma < 0$ and unstable if $\sigma > 0$ and the argument inside the square root is therefore crucial. The unstable condition is thus

$$\frac{\alpha\rho_1\rho_2(U_1 - U_2)^2}{(\rho_1 + \rho_2)^2} - \frac{\alpha g(\rho_2 - \rho_1) + \nu\alpha^3}{(\rho_1 + \rho_2)} > 0 \tag{6.26}$$

$$(U_1 - U_2)^2 > \frac{g(\rho_1^2 - \rho_2^2) + \nu\alpha^2(\rho_1 + \rho_2)}{\rho_1\rho_2} \tag{6.27}$$

Taking a close look at 6.27 we can observe that the wavenumber α might play a significant part in the evolution of a perturbation. We have that $\alpha = \frac{2\pi}{\lambda}$ where λ is the wavelength of the perturbation. Thus a long wavelength will give a relative small alpha whereas a short wavelength will give a relative large alpha.

Orr-Sommerfeld equation

For a parallel and viscous flow, the Orr-Sommerfeld equation predict under what conditions transition to turbulence occur. Flows of such characteristics are governed by the Navier-Stokes equation, which one indeed sets the outset of this derivation.

We start by consider an incompressible laminar flow with a constant density ρ, conductivity k and viscosity ν, and thus giving us the following set of equations, which we know as the Navier-Stokes relations.

$$\nabla \cdot \vec{V} = 0 \tag{6.28}$$

$$\frac{D\vec{V}}{Dt} = -\frac{1}{\rho}\nabla p + \nu \nabla^2 \vec{V} \tag{6.29}$$

Let us now assume that there exist a known laminar flow solution $\vec{V_0} = (U, V, W) = \vec{V_0}(\vec{x}, t)$ and $p_0 = p_0(\vec{x}, t)$. Our aim here is to investigate the stability of these solutions under the impact of a couple of infinitesimal perturbations defined as $\vec{v}(\vec{x}, t) = (\hat{u}, \hat{v}, \hat{w})$ and $\hat{p}(\vec{x}, t)$. Substitute for the superimposed solution $\vec{V_0} + \vec{v}$ and $p_0 + \hat{p}$ into 6.28 and 6.29. Next simply subtract the superimposed equation with the original one and linearize. The linearization is done by discard products of perturbations. The resulting equations are the disturbance equations.

$$\frac{\partial(U+\hat{u})}{\partial x} + \frac{\partial(V+\hat{v})}{\partial y} + \frac{\partial(W+\hat{w})}{\partial z} - \Big(\frac{\partial U}{\partial x} + \frac{\partial V}{\partial y} + \frac{\partial W}{\partial z}\Big) = 0 \tag{6.30}$$

$$\frac{\partial \hat{u}}{\partial x} + \frac{\partial \hat{v}}{\partial y} + \frac{\partial \hat{w}}{\partial z} = 0 \tag{6.31}$$

$$\frac{\partial \hat{u}}{\partial t} + U\frac{\partial \hat{u}}{\partial x} + \hat{u}\frac{\partial U}{\partial x} + V\frac{\partial \hat{u}}{\partial y} + \hat{v}\frac{\partial U}{\partial y} + W\frac{\partial \hat{u}}{\partial z} + \hat{w}\frac{\partial U}{\partial z} = -\frac{1}{\rho}\frac{\partial \hat{p}}{\partial x} + \nu \nabla^2 \hat{u} \tag{6.32}$$

$$\frac{\partial \hat{v}}{\partial t} + U\frac{\partial \hat{v}}{\partial x} + \hat{u}\frac{\partial V}{\partial x} + V\frac{\partial \hat{v}}{\partial y} + \hat{v}\frac{\partial V}{\partial y} + W\frac{\partial \hat{v}}{\partial z} + \hat{w}\frac{\partial V}{\partial z} = -\frac{1}{\rho}\frac{\partial \hat{p}}{\partial y} + \nu \nabla^2 \hat{v} \tag{6.33}$$

$$\frac{\partial \hat{w}}{\partial t} + U\frac{\partial \hat{w}}{\partial x} + \hat{u}\frac{\partial W}{\partial x} + V\frac{\partial \hat{w}}{\partial y} + \hat{v}\frac{\partial W}{\partial y} + W\frac{\partial \hat{w}}{\partial z} + \hat{w}\frac{\partial W}{\partial z} = -\frac{1}{\rho}\frac{\partial \hat{p}}{\partial z} + \nu \nabla^2 \hat{w} \tag{6.34}$$

These are linear partial differential equations for $\hat{u}, \hat{v}, \hat{w}$ and $\hat{p}$. They are linear since U, V and W are known functions and can be seen as variable coefficients. By assuming a locally parallel basic flow we may reduce these equations to an ordinary differential equation. If y is the coordinate normal to the wall or across the shear layer, we assume that the component V across the layer is negligibly small, as in duct flow, and further assume that $U \simeq U(y)$ and $W \simeq W(y)$ which reduces the above set of linear PDE's to

$$\frac{\partial \hat{u}}{\partial x} + \frac{\partial \hat{v}}{\partial y} + \frac{\partial \hat{w}}{\partial z} = 0 \tag{6.35}$$

$$\frac{\partial \hat{u}}{\partial t} + U\frac{\partial \hat{u}}{\partial x} + \hat{v}\frac{\partial U}{\partial y} + W\frac{\partial \hat{u}}{\partial z} = -\frac{1}{\rho}\frac{\partial \hat{p}}{\partial x} + \nu \nabla^2 \hat{u} \tag{6.36}$$

$$\frac{\partial \hat{v}}{\partial t} + U\frac{\partial \hat{v}}{\partial x} + W\frac{\partial \hat{v}}{\partial z} + = -\frac{1}{\rho}\frac{\partial \hat{p}}{\partial y} + \nu\nabla^2 \hat{v} \tag{6.37}$$

$$\frac{\partial \hat{w}}{\partial t} + U\frac{\partial \hat{w}}{\partial x} + \hat{v}\frac{\partial W}{\partial y} + W\frac{\partial \hat{w}}{\partial z} = -\frac{1}{\rho}\frac{\partial \hat{p}}{\partial z} + \nu\nabla^2 \hat{w} \tag{6.38}$$

Next we assume the form of the disturbances. We let them be on the form of traveling waves, specified as

$$(\hat{u}, \hat{v}, \hat{w}, \hat{p}) = [u(y), v(y), w(y), p(y)]exp[i\alpha(xcos\phi + zsin\phi - ct)] \tag{6.39}$$

where $i = \sqrt{-1}$, α is the wavenumber, c is the wavespeed and the frequency $\omega = \alpha c$. These waves are called Tollmien- Schlichting waves. We note that they are parallel to the base flow (they are all traveling along the x-axis) and that each amplitude is a function of y. By putting 6.39 into 6.35, 6.36, 6.37 and 6.38we can obtain a set of linear ODE's with complex coefficients.
First from continuity we have

$$i\alpha u\cos\phi + v' + i\alpha w\sin\phi = 0 \tag{6.40}$$

and for the x-, y- and z- component we get

$$i\alpha u(U\cos\phi + W\sin\phi) + vU' = -\frac{i\alpha}{\rho}p\cos\phi + \nu(u'' - \alpha^2 u) \tag{6.41}$$

$$i\alpha v(U\cos\phi + W\sin\phi - c) = -\frac{1}{\rho}p' + \nu(v'' - \alpha^2 v) \tag{6.42}$$

$$i\alpha w(U\cos\phi + W\sin\phi - c) + w'v = -\frac{i\alpha}{\rho}\sin\phi + \nu(w'' - \alpha^2 w) \tag{6.43}$$

Note that primes denotes differentiation with respect to y. In the next step we first introduce a helpful notation, that is

$$u_0 = u\cos\phi + w\sin\phi \tag{6.44}$$

$$U_0 = U\cos\phi + W\sin\phi \tag{6.45}$$

and then multiply 6.41 with $\cos\phi$, 6.43 with $\sin\phi$ and at last add them together.

$$\begin{gathered} i\alpha(U_0 - c)(u\cos\phi + w\sin\phi) + v(U'\cos\phi + W') = \\ -\frac{i\alpha}{\rho}p + \nu(u''\cos\phi + w''\sin\phi - \alpha^2(u\cos\phi + w\sin\phi)) \end{gathered} \tag{6.46}$$

6.46 can be reduced to 6.48 by using the compact notation introduced right above and similar for 6.47 and 6.49. We are then left with three equations with three variables u_0, v and p.

$$i\alpha u_0 + v' = 0 \tag{6.47}$$

$$i\alpha u_0(U_0 - c) + vU_0 = -\frac{i\alpha}{\rho}p + \nu(u_0'' - \alpha^2 u_0) \tag{6.48}$$

$$i\alpha v(U_0 - c) = -\frac{1}{\rho}p' + \nu(v'' - \alpha^2 v) \tag{6.49}$$

Finally, we may reduce the above set of equations 6.47, 6.48, 6.49 to a fourth order linear homogeneous ODE by eliminate two of the three variables u, v, p. To do this we start by using the continuity equation 6.47 to establish an equation for u_0.

$$v' = -i\alpha u_0 \qquad v''' = -i\alpha u_0''' \tag{6.50}$$

By using 6.50 we can replace u_0 in equation 6.48 and 6.49, transforming them to 6.51 and 6.52 respectively.

$$-v'(U_0 - c) + U_0' v = -\frac{i\alpha}{\rho}p + i\nu(-\frac{v'''}{\alpha} + \alpha v'') \tag{6.51}$$

$$i\alpha v(U_0 - c) = -\frac{1}{\rho}p' + \nu(v'' - \alpha^2 v) \tag{6.52}$$

In order to substitute for the pressure p, compute the derivative of 6.51 wrt y, the derivative of 6.52 wrt x and finally add the resulting equations together to acquire 6.53

$$-v''(U_0 - c) + U_0'' v + \frac{i\alpha}{\rho}p' - i\nu(\frac{v''''}{\alpha} - \alpha v'') - \alpha^2 v(U_0 - c) - \frac{i\alpha}{\rho}p' - i\nu(\alpha v'' - \alpha"2v) = 0 \tag{6.53}$$

as a final step we rearrange 6.53 to obtain the Orr - Sommerfeld equation 6.54

$$(U_0 - c)(v'' - \alpha^2 v) - U_0'' v + \frac{i\nu}{\alpha}(v'''' - 2\alpha^2 v'' + \alpha^4 v) = 0 \tag{6.54}$$

The boundary conditions is that the disturbance will vanish at infinity and at any walls (no-slip).

6.3.2 Results

Figure 6.7 and 6.9 shows the spectrum in the complex plane of the Orr-sommerfeld equation showing the eigenvalues in the form $\lambda = -i\alpha c$. The uppermost eigenvalues are the most unstable and values with a positive complex value c will grow in time and become unstable. The black eigenvalues are from Schmidt and Henningson's book "Stability and transition in shear flows"[13] for a case of Re $= 10000$. For a flow in general one assume that the flow is stable if all eigenvalues are in the lower half plane (negative complex values) meaning that the growth rate of the imposed perturbation will decay and disappear.

The numerical code solves the 50 largest eigenvalues with respect to the complex numbers. The numerical case is solved for a Reynolds number of $Re_D = 10000$ and a perturbation wave number $k = 5$, see the result in figure 6.9.

The experimental profile in figure 6.6 did not have good enough resolution to put in the solver in its original form. The solver uses the second derivative which requires a high resolution of the profile for the derivative to be somewhat smooth. Something about 20 points in the gas phase and 40 in the water made the second derivatives very rough. An interpolation were made to increase the resolution to 100 points in both gas and water phase(same as for the numerical profile) and to smooth out the transition between the phases before the calculation of the eigenvalues. The result can be seen in figure 6.7 were the highest complex value were 0 and thus not unstable but clearly missing out of the theoretical eigenvalues. More experimental profiles need to be inspected to draw any conclusion of the result.

The idea were to compute the highest eigenvalues for several different perturbation wave numbers and then investigate if any conclusion could be drawn of what perturbations were unstable and which were not.

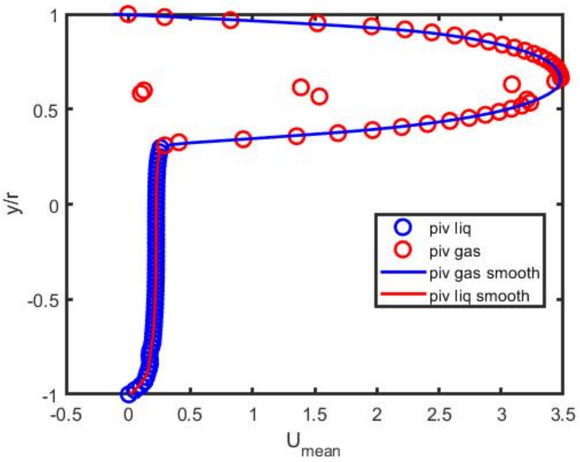

Figure 6.6: *A smoothed and raw experimental profile from PUC. It consists of the mean axial profile* $\overline{U}$ *of the gas velocity on the upper half and the liquid velocity at the bottom. This is a base flow with flow rate* $U_{sl} = 0.14m/s$ *and* $U_{sg} = 0.6m/s$.

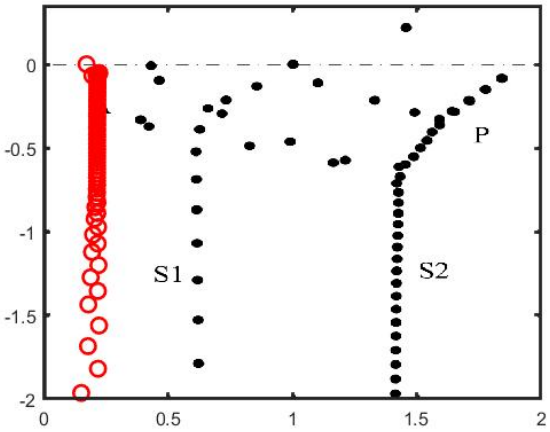

Figure 6.7: *Orr Sommerfeld spectrum with theoretical eigenvalues from [13] in black and red cirlces are the eigenvalues from the smoothed profile in fig6.6.*

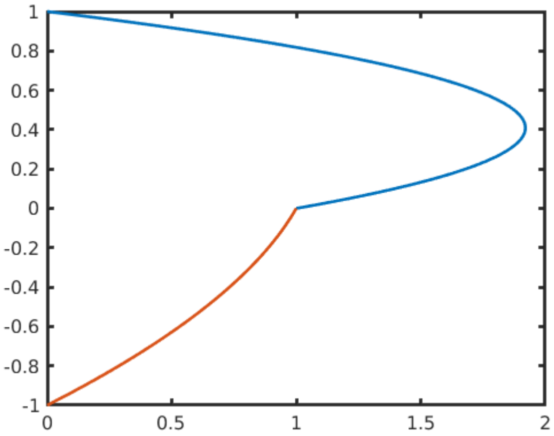

Figure 6.8: *A numerical profile produced from the code by Dr.Aakervik.*

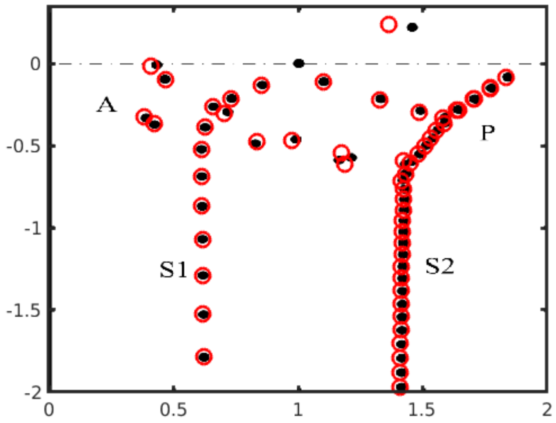

Figure 6.9: *Orr Sommerfeld spectrum with theoretical eigenvalues from [13] in black and red points are the numerical eigenvalues from the profile in figure6.8.*

Chapter 7

Bibliography

Bibliography

[1] `https://www.dantecdynamics.com/seeding-materials`

[2] Birvalski, M. (2015) *Experiments in stratified gas liquid pipe flow.* TU Delft, Delft University of Technology

[3] S. Nogueira, R.G. Sousa, A.M.F.R. Pinto, M.L. Riethmuller, J.B.L.M. Campos. 2003 *Simultaneous PIV and pulsed shadow technique in slug flow: a solution for optical problems* Experiments in Fluids 35 (2003) 598–609 DOI 10.1007/s00348-003-0708-8

[4] Scharnowski, S. & Kähler, C.J. *On the loss-of-correlation due to PIV image noise* Exp Fluids (2016) 57: 119. `https://doi.org/10.1007/s00348-016-2203-z`

[5] Scharnowski S., Bross M., Kähler J. C (2018)*Accurate turbulence level estimations using PIV/PTV*Experiments in Fluids(2019)60:1 `https://doi.org/10.1007/s00348-018-2646-5`

[6] Keane, R.D. & Adrian, R.J.(1992)*Theory of cross-correlation analysis of PIV images* Applied Scientific Research (1992) 49: 191. `https://doi.org/10.1007/BF00384623`

[7] WU, X., & MOIN, P. (2008). *A direct numerical simulation study on the mean velocity characteristics in turbulent pipe flow.* Journal of Fluid Mechanics, 608, 81-112. doi:10.1017/S0022112008002085

[8] Y Kaneda, T Ishihara, M Yokokawa, K Itakura, A Uno *Energy dissipation rate and energy spectrum in high resolution direct numerical simulations of turbulence in a periodic box* Physics of Fluids 15 (2), L21-L24

[9] Xu D., Chen J *Accurate estimate of turbulent dissipation rate using PIV data*Experimental Thermal and Fluid Science Volume 44, January 2013, Pages 662-672

[10] L. F. Richardson. *The supply of energy from and to atmospheric eddies.*Proc. R. Soc. Lond. A,97(686):354–373, 1920

[11] Wieneke B (2015), *PIV uncertainty quantification from correlation statistics.* Meas. Sci. Technol. 26(7) 074002

[12] Westerweel J, Scarano F (2005) *Universal outlier detection for PIV data.* Exp Fluids 39:1096–1100

[13] Schmid, Peter S Henningson, Dan. (2001). *Stability and Transition in Shear Flows.* 10.1007/978-1-4613-0185-1.

[14] Masullo, A., Theunissen, 2016 *Adaptive vector validation in image velocimetry to minimise the influence of outlier clusters* R. Exp Fluids (2016) 57: 33. `https://doi.org/10.1007/s00348-015-2110-8`

[15] Kislaya A and Sciacchitano A (2018), *Peak-locking error reduction by birefringent optical diffusers.* Meas. Sci. Technol. 29(2) 025202

[16] Xue Z, Charonko JJ and Vlachos PP (2014), *Particle image velocimetry correlation signal-to-noise ratio metrics and measurement uncertainty quantification.* Meas. Sci. Technol. 25(11) 11530

[17] Charonko JJ and Vlachos PP (2013), *Estimation of uncertainty bounds for individual particle image velocimetry measurements from cross correlation peak ratio.* Meas. Sci. Technol. 24 065301

[18] Sciacchitano A and Wieneke B (2016), *PIV uncertainty propagation.* Meas. Sci. Technol. 27 084006 (16pp)

[19] William. K George, Lectures in Turbulence for the 21st Century. *Chalmers University of Technology* (2013).

[20] B Lautrup Physics of Continuous Matter, Second Edition *The Niels Bohr Institute Copenhagen, Denmark* (2011).

[21] Stephen B.Pope, Turbulent Flows *Cornell University* (2003).

[22] Frank M. White, Viscous Fluid Flow, Third Edition *University of Rhode Island* (2006).

[23] Osborne Reynolds XXIX. *An experimental investigation of the circumstances which determine whether the motion of water shall be direct or sinuous, and of the law of resistance in parallel channels.* 174.Philosophical Transactions of the Royal Society of London

[24] `https://nptel.ac.in/courses/101103004/module5/lec1/3.html`.

[25] Osborne Reynolds (1895) Philosophical Transactions of the Royal Society of London. A Vol. 186 (1895), pp. 123-164

[26] Schulkes Ruben, An introduction to Multiphase Pipe Flow. (2010).

[27] Raffel Markus, Willert E. Christian, Wereley T.Steve, Kompenhans Jürgen. *Partice Image Velocimetry, A Practical Guide* Second Edition Springer-Verlag Berlin Heidelberg 1998 2007

[28] Kolaas Jostein, *Getting started with HydroLabPiv v1.1* Research Report in Mechanics ISSN 0801–9940

[29] C.E Willert, M. Gharib *Digital particle image velocimetry* Experiments in Fluids 10, 181-193 (1991)

[30] Padifield. D, 2012 *Masked Object Registration in the Fourier Domain* IEEE Transactions on image processing 21(5):2706-2718

[31] Hugh W. Coleman, W. Glenn Steele *Experimentation, Validation, and Uncertanity Analysis for Engineers* Third Edition 2009 John Wiley & Sons, Inc. ISBN: 978-0-470-16888-2

[32] A.A Ayati, J. Kolaas, A. Jensen, G.W. Johnson*A PIV investigation of stratified gas-liquid flow in a horizontal pipe*International Journal of Multiphase Flow 61 (2014) 129-143

[33] Foucaut JM, Milliat B, Perenne N, Stanislas M (2003) *Characterisation of different PIV algorithm using the europiv synthetic image generator and real images from a turbulent boundary layer.* EUROPIV2 workshop, Zaragoza, Spain

[34] Lecordier, B., Trinit, M., 2003. *Advanced PIV algorithms with image distortion validation and comparison from synthetic images of turbulent flow.* In: 5th International Symposium on Particle Image Velocimetry, September 22–24. Busan, Korea.

[35] Westerweel, J., 1997. *Fundamentals of digital particle image velocimetry.* Measur. Sci. Technol. 8, 1379–1392.

[36] Soria, J., 2006. *Lectures Notes on Turbulence and Coherent Structures in Fluid, Plasma and Non-Linear Media.* World scientific, Singapore (Chap.7).

[37] Herpin, S., Wong, C.Y., Stanislas, M., Soria, J., 2008. *Stereoscopic PIV measurements of a turbulent bounday layer with a large spatial dynamic range.* Exp. Fluids 45, 745–763.

[38] Raffel M., Christian E. W,Scarano F., Kähler C., Wereley S.T.,Kompenhans J. *Particle Image Velocimetry, A practical guide* Third Edition Springer International Publishing AG, part of Springer Nature 2018

[39] Cameron, S.M., 2011. *PIV algorithms for open-channel turbulence research; accuracy, resolution and limitations* J. Hydro-Environ. Res. 5,247-262.

[40] Thielicke, W. and Stamhuis, E.J., 2014. *PIVlab – Towards User-friendly, Affordable and Accurate Digital Particle Image Velocimetry in MATLAB.* Journal of Open Research Software, 2(1), p.e30

[41] Christensen.,K.,T.,2004 *On the influnece of peak-locking errors on turbulence statistics compared from PIV ensembles* Exp. Fluids 36 484-97

[42] Michaelis D., Neal R. D., Wieneke B. *Peak-Locking reduction for particle image velocimetry* Meas. Sci. Technol. 27 104005

[43] Adrian R. J. and Westerweel J., 2010 *Particle Image Velocimetry* New York, Cambridge University Press

[44] Roesgen T (2003) *Optimal subpixel interpolation in particle imagevelocimetry.* Exp Fluids 35(3):252–256

[45] Fessler J. R., Eaton J. K, 1999 *Turbulence modification by particles in a backward-facing step flow* J.Fluid Mech.,394, pp.97-117

[46] Lau, T., Nathan, G. (2016).*The effect of Stokes number on particle velocity and concentration distributions in a well-characterised, turbulent, co-flowing two-phase jet.* Journal of Fluid Mechanics, 809, 72-110. doi:10.1017/jfm.2016.666

[47] Scarano F (2002) *Iterative image deformation methods in PIV.* Meas Sci Technol 13(1):R1–R19. https://doi.org/10.1088/0957-0233/13/1/201 (ISSN: 0957-0233)

[48] Adrian, R.J. 1997 *Dynamic ranges of velocity and spatial resolution of particle image velocimetry.* Meas. Sci. Technol. 8(12), 1393–1398 (1997). DOI 10.1088/0957-0233/8/12/003.

[49] Adrian RJ (2007) *Hairpin vortex organization in wall turbulence.* Phys Fluid 19

[50] Robinson SK (1991) *Coherent motions in the turbulent boundary layer.* Annu Rev Fluid Mech 23:601–639

[51] Stanislas M, Perret L, Foucaut JM (2008) *Vortical structures in the turbulent boundary layer: a possible route to a universal representation.* J Fluid Mech 602:327–382

[52] Wang Zhi-Qing *Study on correction coefficients of laminar and turbulent entrance region effect in round pipe* Applied Mathematics and Mechanics (English Edition, Vol.3, No.3; June 1982)

[53] Sanchis, A. & Jensen, *Dynamic masking of PIV images using the Radon transform in free surface flows* A. Exp Fluids (2011) 51: 871. `https://doi.org/10.1007/s00348-011-1101-7`

[54] Brown L. , (1992) *A survey of image registration techniques* ACM Comput. Surv. (CSUR), 24 (4) (1992), p. 376

[55] Welch PD (1967) *The use of fast fourier transform for the estimation of power spectra: A method based on time averaging over short, modified his periodograms.* IEEE Trans Audio Electroacoustics AU- 15:7. `http://doi.org/10.1109/TAU.1967.1161901`

[56] Moin, P. (2009) *Revisiting Taylor's hypothesis* Journal of fluid mechanics , 2009, Vol.640, p.1-4